Study and Control of Nonlinearity in Large-Mode-Area Fibers

By
I-Ning Hu

A dissertation submitted in partial fulfillment
of the requirements for the degree of
Doctor of Philosophy
(Electrical Engineering)
in the University of Michigan
2015

Doctoral Committee:

Professor Almantas Galvanauskas, Chair
Associate Research Scientist John A. Nees
Associate Professor Alexander G.R. Thomas
Professor Herbert G. Winful

Dedication

Dedicated to my family

Acknowledgements

Making an acknowledgement list is a difficult task for me, because the number of people whom I would like to show my gratitude to seems countless. If someone is missed in this list, he or she must be hided in my heart.

Certainly, in these 6 years of PhD study, the most important person is my adviser Professor Almantas Galvanauskas. I would like to express my highest gratitude to him for playing two important roles in this period. He is a knowledgeable, enthusiastic and supportive research adviser. Whenever my research progress was stuck, he was often more anxious than me to resolve the issue and always provided a great guidance to help me go across the barrier. He was also a successful model showing me men's responsibility in family. He served as one of the two main witnesses of our wedding, and shared many tips with me for well maintaining a marriage and raising a baby. In addition to being a good researcher, I also learned how to be a good husband and a good father from him.

I want to thank all my committee members' help in reviewing and evaluating my dissertation. I appreciate the time and effort that you have spent on my PhD study and graduation process. Moreover, I would like to thank Professor Winful who in his class EECS 634 helped me develop the essential knowledge of nonlinear optics that can be directly applied to most of my research projects. I would like to thank Professor Thomas who helped me conquer the most critical numerical problem in solving the time-dependent coupled equations of thermally-induced two beam coupling. I would like to thank Professor John Nees who was always around the office and labs providing immediate help and

advises in our research works.

I would like to thank my colleagues Cheng Zhu, You-Chia Chang, Tong Zhou, Michael Haines, John Trey Ruppe, Siyun Chen, and Hafiz Sheriff, in particular Cheng and You-Chia. Without Cheng, I probably cannot make it to defend today. She helped solve countless technical issues in the experiments. A metaphor can let you understand how much she helped me: if I represents a nonlinear optical effect, she is the high power beam. You-Chia's knowledgeability and dedicating attitude of being a scholar inspired me when I was learning to be a PhD student. My in-depth sense of optics was mostly attributed to the discussion with him.

I also would like to thank my former colleagues Xiuquan Ma, Wei-Zung Chang, Matthew River, and Shenghong Huang. Like Cheng, they also gave me much support of my research work. Especially Xiuquan, his guiding in the physics of chirally-coupled core fibers solidified my understanding of fiber optics.

I would like to thank the department staffs Bett Weston, Car Nosel, Steven Pejuan, Stephanie Wicklund, Beth Stalnaker, Karen Liska, Debra Dieterle, Linda Owens, and Shonda Bottke. They help me address the most cumbersome paper works in my PhD study.

I would like to thank my English teachers, Judith Nowark, Christopher Luebbe, Elizabeth Hildinger, and Judy Dyer. They spent their private time tutoring me and helping me build up my English skills. Being a foreigner who used to have serious language issues, I felt so lucky to meet these four benevolent teachers.

Moreover, I would like to thank my friends in the university, in Taiwan, around the U.S., and the other part of the world. They either mentally or physically supported me so that I'll be able to arrive at the end of this long journey.

The last but not the least, I have countless thanks to my lovely family members. My

wife, Chi-Mei, gave up her prosperous life in Taiwan and came to the U.S. with me. In these years, especially after having our baby, every day was hard day for her. I really don't know how I can thank her enough. The only thing I can give back is my love to her in the rest of my life. I also would like to thank our baby. His born encouraged me to confront every difficulty that I have experienced or will experience. In the end, I would like to thank my parents, who brought me to this world, raised me up with love, and educated me with care. I'll always strive my best to make them proud of me.

Table of Contents

List of Figures

List of Tables

Abstract

Study and Control of Nonlinearity in Large-Mode-Area Fibers

By

I-Ning Hu

Chair: Almantas Galvanauskas

Numerous practical advantages of high power fiber lasers make them important in many scientific and industrial applications. However, the relatively small mode-area and long propagation-length in an optical fiber also enhance nonlinear interactions, and pose limits on achievable average and peak powers of fiber lasers. In this dissertation, we explore such nonlinear effects and their control in chirally-coupled-core (CCC) fibers, an important and practical type of large-core effectively-single-mode fibers.

Many laser applications require short wavelengths. We study use of four-wave-mixing (FWM) for wavelength conversion in CCC fibers. Our theoretical analysis shows that under proper conditions CCC fibers can be used for efficient and high-power wavelength conversion from ~1μm to yellow through red visible wavelengths.

We study the use of the spectral filtering property of CCC fibers to suppress stimulated Raman scattering (SRS). SRS suppression has been experimentally achieved in two types

of spectrally-tailored CCC fibers, demonstrating an additional degree of design freedom, by combining core-size scalability with SRS suppression.

Average powers in large-core amplifying fibers are limited by the thermally induced transverse mode instability (TMI). We show that TMI is essentially a two-beam coupling process, causing stimulated scattering from the fundamental to higher-order modes. We further show that increasing higher-order mode suppression in CCC fibers increases TMI threshold power.

CCC fibers are low-birefringence fibers, in which fiber coiling and twisting produces externally induced linear and circular birefringence. The presence of the latter complicates nonlinear polarization evolution (NPE) at high peak powers, and can degrade polarization preservation at the amplifier or laser output. Our experimental and theoretical analysis shows that with proper signal excitation and fiber packaging conditions linear output polarization can be maintained over a wide range of output peak powers.

Additionally, this dissertation includes a study of some design aspects of large-core polygonal-core CCC fibers, directly related to fiber modal properties that can be used in controlling nonlinear interactions.

Results of this work are important for using CCC, as well as other types of flexible (i.e. non-rod type) effectively-single-mode fibers, in high power and energy fiber lasers.

Chapter I

Introduction

1.1 Current Status of Fiber Lasers

High power fiber lasers are in demand for many industry, defense, energy solutions and scientific applications. In the last two decades, the output power of fiber lasers has been improved more than a thousand times, making fiber lasers applicable to a variety of fields such as material processing, aerosol monitoring, biomedical tomography and high field science, aerospace detection and, military purposes [1,2]. In fact, in the early 1990s, the output power of fiber lasers was on the order of 10W, while in the 2010s, 100kW output power has been achieved [3]. This remarkable power scalability is attributed to the high efficiency of fiber lasers and the development of relevant pumping schemes.

A fiber laser is a laser in which the gain medium is an optical fiber, typically doped with rare-earth ions. Thus, fiber lasers inherently have the advantages of optical fibers, such as good beam quality, stability, compactness and robustness. In addition, high efficiency can be achieved in ytterbium-doped fiber (YDF) lasers. The light emission of YDF lasers is via a simple electronic transition ($^2F_{7/2} \rightarrow {}^2F_{5/2}$), resulting in high quantum efficiency, minimization of the heat generation, and reduction of excited state absorption and non-radiative decay [4]. These advantages have made YDF lasers more preferred for high power operation than other rare-earth-doped fiber lasers and other types of lasers since 1999 [5,6,7,8].

An important innovation that enables power scalability in fiber lasers was the development of cladding pumping scheme [9,10]. In 1988, the issue of coupling low-brightness pump light into small or low-NA active fiber cores was entirely resolved with double-clad structure. The essence of this approach is that an "inner" cladding, which is surrounded by an "outer" cladding, serves as a highly-multimode waveguide for the larger and lower-quality pump beam. This structure enables efficient coupling of pump light into single-mode or few-mode fibers. This technique can also be extended to the multiple-clad structure [11]. Moreover, other relevant pumping schemes such as the breaking of cladding rotational symmetry [12] for increasing the overall pump absorption or the tapered fiber bundle combiners [13] for further creating high brightness, high power pumping modules have also contributed to the tremendous achievement in high power fiber laser development. These designs have resolved the limitation on pump coupling and efficiently increased the power scalability of fiber lasers, but this also ushers in the next limitation, the threshold of nonlinear effects.

1.2 Limitation from nonlinear effects

Improved power scaling leads to the onset of nonlinear optical effects in fiber lasers. The geometry of fiber lasers, which contributes most significantly to their superior performance, is associated to the enhancement of optical nonlinearities. The strength of nonlinear optical interactions is inversely proportional to the mode area and proportional to the optical path. This reveals that nonlinear effects are ultimately unavoidable in fiber lasers, especially at high power levels. In CW or pulsed fiber lasers, there are various types of nonlinear effects, and they can be classified into two categories, inelastic and elastic. The former includes stimulated Brillouin Scattering (SBS), stimulated Raman scattering (SRS), and transverse mode instability (TMI) specific to in high power fiber amplifiers, and the latter includes self-phase modulation (SPM), cross-phase modulation (XPM), four-wave-mixing (FWM), and self-focusing (SF). The three scattering effects are inelastic because a delayed response in the light-matter interaction exists, thus, the signal frequency is downshifted and the lost energy is transferred to material waves (phonons). As for the four elastic effects, which are also called Kerr effects, since they are induced by a nearly immediate response of the power dependent refractive index, the energy of the optical waves is conserved.

These nonlinear effects usually do not happen all together, since the threshold of the dominant nonlinear effect depends on both the properties of the material and the state of the optical waves. In the following content, the study of nonlinear effects with the relevant mitigation strategies is divided into three subsections, which in order of occurrence are SRS and SRS, the Kerr effects, and TMI. TMI is discussed separately because it only occurs in active media.

1.2.1 Stimulated Scattering Effects

SBS and SRS are two similar nonlinear effects, since they are associated to the vibrational excitation modes of the fiber glass. In both scattering processes, when the threshold is reached, the energy in the signal wave is transferred to the Stokes wave. SBS develops from the acoustic waves (acoustic phonon) that are driven by the propagating waves via electrostriction [14]. If the bandwidth of the light waves is much smaller than or close to the acoustic vibration frequency of fiber glasses (~100 MHz [15]), SBS is the dominant effect. When the SBS threshold is reached, the propagating optical wave inelastically resonates with the induced acoustic waves and scattered backward due to the requirement of energy and momentum conservation. The energy in the propagating optical waves is partly transferred to the acoustic waves and the frequency of the backward scattered wave is downshifted by ~10 GHz [15]. This scattered wave can destabilize the whole laser system, and can even damage the oscillator or fiber ends. However, SBS only limits the achievable power of narrow-linewidth signals transmitting through a fiber laser. When the bandwidth of a signal is increased, the response time of acoustic waves cannot keep pace with the optical waves, reducing the peak gain and increasing the threshold of SBS by a factor of $\Delta\nu_s/\Delta\nu_B$, where $\Delta\nu_s$ is the bandwidth of the signal and $\Delta\nu_B$ is the bandwidth of SBS gain. Therefore, for a broadband optical signal, the other inelastic nonlinear effect, SRS, takes over.

SRS is the most significant limiting nonlinear effect for continuous-wave (CW) or quasi-CW high power fiber lasers. The onset of SRS is associated with the resonance of the glass lattice (optical phonon). The difference between SRS and SBS is that the scattered waves in the SRS process mainly propagate forward. Because of phase-mismatching and

the lack of excited optical phonons, the occurrence probability of backward SRS is much smaller than forward [16]. In the fused silica, SRS downshift the signal frequency by 13.2 THz with an extension of 40 THz for signal wavelengths around 1 μm [15]. While the threshold of SRS is surpassed as with SBS, the signal energy rapidly flows to the Stokes waves at longer wavelengths.

Several methods of mitigating SBS and SRS have been demonstrated in 2000s. Since the emergence of SBS is due to the excitation of acoustic waves with limited bandwidth, mitigation strategies focus on broadening the spectrum of the light waves. This can be achieved by either modulating with pseudo-random signals [17] or naturally by the longitudinal temperature gradient in active fibers [18,19]. Moreover, an alternative method is to apply an acoustically anti-guiding profile on the fiber to reduce the overlap between the light wave and the acoustic modes [20]. As for the mitigation of SRS, the approaches are mainly based on spectral filtering techniques that can be achieved by inserting long-period grating or by employing specialty fibers to attenuate the Stokes waves. This technique will be discussed in greater detail in Chapter III.

1.2.2 Kerr Nonlinear Effects

The Kerr effect is the power- or intensity-dependent nonlinear refractive index induced via the third-order nonlinearity $\chi^{(3)}$. In a silica medium, when the intensity of a light wave is high enough (>100 MW/cm^2), the refractive index through which the light wave propagates is larger than at low intensity. Consequently, the Kerr effect mainly modifies the phase of propagating light waves through the nonlinearly-induced variation of the optical path. Therefore, unlike stimulated scattering processes, the energy of the light

waves is conserved. Categorized by the phenomenological facts and the light waves involved, the Kerr effect includes a variety of nonlinear effects such as SPM, XPM, SF, and FWM.

SPM and XPM are influential when the signal pulse belongs to ultrafast regime (<50 ps [15]), SPM can lead to symmetric broadening while XPM, which is attributed to the existence of the other waves, can lead to asymmetric broadening of the signal bandwidth. When a high-intensity ultrafast pulse goes through a segment of optical fiber, the bandwidth broadening caused by SPM and XPM accompanied with the existing dispersion leads to a distortion on its temporal profile. This distortion can reduce the quality of a recompression process in a chirp-pulse-amplification system. However, this distortion can be compensated by pre-modulation of the phase [21]. Incidentally, except the above mentioned nonlinear effects which are specifically influential in ultrafast pulses, if a constant polarization cannot be maintained along a high-intensity fiber laser, the two polarization modes of the signal can also induce XPM. This XPM can also lead to a nonlinear polarization evolution which can randomize the output polarization status. The detail of this process is given in Chapter V.

Ultimately, power scalability is limited by self-focusing. This type of Kerr effect occurs in the spatial domain. Unlike the other types of Kerr effect, the threshold is determined by peak power rather than peak intensity. When the threshold is reached, the distribution of the local refractive index follows the beam shape and forms a focusing lens. This lens can focus the propagating beam to a tight spot which can irreversibly damage the fiber. Since currently there is no solution for this beam-collapsing effect, the upper limit of power scaling is about 4MW for linear polarized waves at 1-μm wavelength [22]. The only method to mitigate SF is to operate at longer wavelength, since the SF threshold is

quadratically proportional to the wavelength [23].

FWM is often described as a process in which two waves interact with a Kerr medium and produce the two other waves. However, one can also more generally view FWM as an interaction among four different waves. A complete FWM process involves SPM, XPM, and wavelength conversion which requires phase-matching to become efficient. Thus, SPM and XPM and wavelength conversion can also be viewed as three different types of FWM. SPM is a nonlinear process of mixing four waves at the same frequency; XPM is of mixing two waves at a common frequency with the two other waves at another common frequency; wavelength conversion is of mixing four waves, all at different wavelengths, and due to phase-matching requirement, efficient conversion can hardly be observed. As has been pointed out, SPM and XPM both hinders power-scalability in fiber lasers, and mitigating both of them is always in the scope of cutting edge designs. Contrarily, efficient generation of the wavelength conversion is ardently pursued in this field. The reason is that the application of fiber lasers, which only have limited selections of wavelength, can be further extended if a wide range of wavelength is available. The details concerning wavelength conversion is introduced in Chapter II.

Broadly speaking, the most straightforward path to diminish these nonlinearities, including SBS, SRS, SPM, XPM, for the purpose of improving the power scalability of fiber lasers is to enlarge the core size of fiber lasers. The enlarged core size allows a large mode field area, proportionately reducing fiber nonlinearity. However, this intuitive solution raises another newly-found nonlinear effect, transverse mode instability (TMI).

1.2.3 Thermally-induced Stimulated Scattering: Transverse Mode Instability

TMI is first observed in 2011 and is quickly recognized as the limitation of power scaling capability of fiber lasers [24]. TMI refers to a fluctuation of output transverse modes in high power fiber amplifiers. The phenomenon is illustrated in Fig. 1.2-1 [2], which shows the onset of TMI when the output power is just below the threshold and the fluctuation of the output mode at a power level above threshold. This fluctuation is on millisecond scale, which suggests that the origin of TMI is associated to the thermal diffusion.

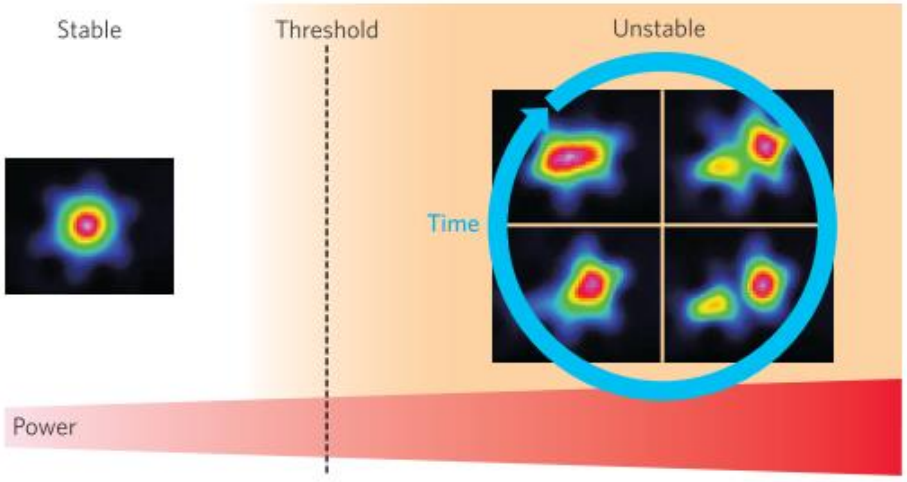

Fig. 1.2-1 Schematic of transverse mode instability [2]

As with SBS and SRS, we recognized TMI as a threshold-like inelastic nonlinear scattering process which is attributed to the multi-mode performance of high power fiber amplifiers. When a fiber amplifier that can support more than one mode is operated at high average output (above TMI threshold), the coupling between fundamental mode (FM) and higher order modes (HOM) is stimulated. There are three phases of TMI status [25]: 1) below threshold where stable modal output is observed; 2) near, but above threshold where

periodic modal oscillation emerges; 3) well above threshold where chaotic modal oscillation dominates. These phenomena observed at the output end of high power fiber amplifiers, are broadly explained as the emergence of a thermally-induced grating (thermal phonon) which comes from the depletion of local population inversion due to the heat that is periodically generated with the modal beating pattern. The formation of this grating takes approximately a millisecond [26], a delay that further indicates the inelasticity of the TMI process and argues that TMI is a stimulated scattering process. Therefore, a frequency downshift between the coupled modes is expected.

An alternative approach contends that TMI is not necessarily a stimulated scattering process. A non-adiabatic waveguide change is used to explain the onset of TMI in fiber amplifiers when the threshold is reached [27]. The key point of this statement is that above TMI threshold, the beam cannot adapt itself fast enough to the rapidly changing waveguide conditions due to the ongoing non-adiabatic heat flow thus a phase lag is induced between the thermal grating and the radiation beating. This explanation is fully accepted by the researchers who observe TMI in their simulations without considering the frequency difference between the coupled modes [28,29]. However, we noticed that the instability in TMI simulations that exclude frequency difference between modes is commonly caused by numerical truncation error. An explanation regarding this error will be discussed in Chapter IV.

When the threshold of TMI is reached, the output beam quality degrades and the modal content fluctuates. Currently, this type of thermally-induced nonlinear effect still cannot be fully controlled or avoided. The reported strategies of mitigating TMI, like an active excitation of out-of-phase HOM [30] to wash out the thermally-induced grating, delocalization of HOM away from the FM [31], and confined doping to reduce pump

absorption [32], are still not very effective. Therefore, we believe an understanding of TMI is required, since the full picture of TMI is not yet clear. A detailed analysis of TMI and our scheme of increasing TMI threshold by enhancing higher-order mode suppression in chirally-coupled core fibers are introduced in Chapters IV and VI.

1.3 Chirally-Coupled Core Fibers

In order to increase output power of fiber lasers and simultaneously mitigate TMI or control other nonlinear effects (except self-focusing), enlarging the core size while maintaining diffraction-limited output-beam quality is indeed required. Conventional large-mode-area (LMA) fibers can achieve this goal by external controls such as the technique of single-mode excitation [33] or the employment of fiber bending [34], but these methods can only be effective with smaller-core (<25μm) multimode fibers and are very sensitive to external perturbation such as stress or imperfect alignment of signal injection. Moreover, fiber bending can hardly be applicable to the fiber with a larger core size or a lower numerical aperture to suppress higher-order mode (HOM), because the bending-induced loss of fundamental mode (FM) and HOMs cannot be distinguished. Thus, specialty fibers provide alternative approaches to realize core scalability. The two important approaches to improve the power scalability of fiber lasers are photonic crystal fiber (PCF) [35] and large-pitch fibers (LPF) [36]. The main feature of PCF is the fiber core surrounded by an air-hole structure which lowers the refractive index of the cladding thus being able to guide waves in the core. By properly designing the photonic band-gap structure of the cladding, the numerical aperture can reach as small as 0.02, and this allows single-mode operation in a fiber structure with large core size. However, a significant concern is that this kind of PCF is not bendable when the core size exceeds 40μm eliminating one of the essential advantages of optical fibers. As for LPF, the approach to realize single mode operation is based on HOM delocalization, which only occurs with a specific heat deposition. So LPF can only be applied to active fibers which are operated at a specific power level. As with larger-core PCF, LPFs are not bendable as well, even though its core scalability is indeed the largest in specialty fibers [37].

Since the common goal of the developed specialty fibers is to realize core scalability and to introduce a distinguished loss for HOMs while keeping the advantages of fiber laser technology, our research group has developed CCC fibers, which features single or multiple helical side cores around a modal guiding central core [38,39]. Based on quasi-phase-matching of the modal coupling between the side cores and the central core or the intra-core modal coupling from guided modes to leaky modes, HOMs in the central core can be attenuated thus realizing the effectively single-mode propagation and spectral control. Previous work in our group shows that CCC fibers can achieve the desired single-mode property with large core-size and without losing any of the conventional advantages of optical fibers [38,39]. Furthermore, the spinning fabrication process of CCC fibers also makes them free from intrinsic birefringence, a property that indicates CCC fibers are naturally polarization-maintaining fibers [40].

With the special features described above, CCC fibers have the potential to control a variety of nonlinearities. TMI can be mitigated with CCC fibers by the property of effective single-mode propagation. SRS can be suppressed by the properties of core-size scalability and transmission spectral control. The wavelength conversion achieved by FWM can be realized with SRS being suppressed. The nonlinear polarization evolution (NPE) can be controlled by engineering the externally-induced birefringence since CCC fibers are free from intrinsic birefringence. Overall, the purpose of this dissertation is to study and control several critical types of nonlinearities emerging in CCC-fiber-based high power fiber lasers as well as in passive CCC fibers. Furthermore, in order to improve the capability of CCC fibers to control nonlinearities, the design principles governing polygonal-core CCC (P-CCC) fibers are investigated and shown in Chapter VI.

1.4 Chapter Overview

In this dissertation, the focus is on two parts: (1) the study of the following nonlinear effects: four-wave-mixing (FWM), stimulated Raman scattering (SRS), transverse mode instabilities (TMI), and nonlinear polarization evolution (NPE); (2) the control of these nonlinear effects with CCC fibers.

In Chapter II, the analysis of wavelength conversion via FWM nonlinear effect is analyzed with 5 aspects: phase-matching, the generation of fundamental-mode signal, the competing SRS nonlinearity, the loss of idler signal, and the acceptable pump bandwidth. In Chapter III, the concept of suppressing SRS using spectrally tailored transmission in a CCC fiber and the demonstration of it with two different types of CCC fibers are introduced. In Chapter IV, the detailed physical process of thermally-induced gratings, a static and a time-dependent models of TMI, the origin of TMI, and the suppression of TMI with CCC fibers are discussed. In Chapter V, the study of nonlinear polarization evolution in CCC fibers, the stabilizing input polarization mode, and the demonstration of the preservation of linear polarization at the output of a 55-μm polygonal-core CCC fiber amplifier are introduced. In Chapter VI, some design aspects of P-CCC fiber and the effect of bending enhanced HOM suppression is investigated.

Chapter II

Analysis of Wavelength Conversion in Large-Mode-Area Fibers

2.1 Introduction

Present fiber lasers can only operate at few fixed wavelengths, as determined by the availability of the suitable rare-earth ions: Yb-doped fused silica fiber lasers operate at 1μm wavelength, Er-doped at 1.55μm, and Tm-doped at 2μm. However, a large variety of applications requires high power laser operation at other wavelengths, short (visible or UV) wavelengths in particular. Conventionally, laser beam wavelengths are converted by using $\chi^{(2)}$ nonlinear interactions, such as parametric down-conversion, sum-frequency or harmonic frequency generation, in bulk nonlinear crystals. This is associated with two principal limitations: (1) such conversion schemes cannot be implemented as monolithic all-fiber systems thus including many unnecessary source of loss, and (2) material properties of the majority of available nonlinear crystals makes it difficult to use such schemes for high optical power operation (due to material lifetime and damage issues). Thus, we are exploring methods to use four-wave-mixing (FWM) through $\chi^{(3)}$ nonlinear interactions in fused silica optical fibers to overcome these limitations since the wavelength conversion realized in optical fibers has important advantages related to the issue of life time and damage threshold.

Wavelength conversion of fiber laser output through FWM process has been explored from the end of last century [15]. However, all the explored approaches so far use small-core single-mode optical fibers, such as highly nonlinear fiber (HNLF). Even the claimed large mode area (LMA) photonic crystal fibers (PCF) that are applied to an efficient FWM process can only be with <15μm core size [41-42]. This limits the power scalability of such conversion schemes. Our goal is to exploit properties of novel CCC fibers [38,39], which can provide single-mode operation at very large core sizes (with mode areas 5 times larger than that of conventional single-mode fibers, ~30μm). Most importantly, CCC fibers enable monolithic integration of such large-core fiber lasers while maintaining diffraction-limited output beam quality.

In the following sections, the analysis to assess an efficient wavelength conversion in LMA-CCC fibers is introduced.

2.2 Modeling of degenerate four-wave-mixing

Four-wave-mixing is a complex of the 3rd order nonlinear optical processes, which involves self-phase modulation (SPM), cross-phase modulation (XPM), and wavelength conversion which requires the achievement of phase-matching. More generally speaking, each of SPM, XPM, and wavelength conversion is a specific type of FWM. This point of view can be revealed in the wave equation with the 3rd order nonlinear polarization [15].

$$\nabla^2\vec{\mathbf{E}} - \frac{1}{c^2}\frac{\partial^2\vec{\mathbf{E}}}{\partial t^2} = \mu_0\frac{\partial^2\vec{\mathbf{P}}}{\partial t^2} \tag{2.2-1}$$

$$\vec{\mathbf{P}} = \varepsilon_0\chi^{(3)}\vdots\vec{\mathbf{E}}\vec{\mathbf{E}}\vec{\mathbf{E}} \tag{2.2-2}$$

Eq. (2.2-1) and Eq. (2.2-2) reveal that through the 3rd-order electric susceptibility, the interaction of three waves produces the fourth wave. Therefore, it is reasonable to identify FWM to be the most general 3rd-order nonlinear process which includes, SPM, XPM, wavelength conversion, and even third harmonic generation.

The mathematical form of a linearly polarized electrical field of frequency ω which includes four optical waves can be defined as

$$\vec{\mathbf{E}} = \frac{1}{2}\hat{x}\sum_{j=1}^{4}A_j(z)F(r_\perp)\exp\left[j\left(\beta_j z - \omega_j t\right)\right] + c.c. \tag{2.2-3}$$

where *A* is the amplitude, *F* is the radially symmetric modal profile, and β is the modal propagation constant. In order to derive a scalar model of FWM, Eq. (2.2-2) is substituted into Eq. (2.2-1) with the optical waves shown in Eq. (2.2-3). The scalar model of FWM can then be derived as [15]

$$\frac{dA_l}{dz} = j\frac{n_2\omega_l}{c}\cdot\left(f_{ll}\left|A_l\right|^2A_l + 2\cdot\sum_{j\neq l}f_{ij}\left|A_j\right|^2A_l + f_{mnkl}A_m^*A_nA_k\cdot e^{j\Delta k_l z}\right), l = 1-4 \tag{2.2-4}$$

where *f* is the modal overlap factor, Δk_l is the phase mismatch and n_2 is the nonlinear refractive index coefficient. The effective area of the wave interaction can be defined by

the modal overlap

$$A_{eff,l} \equiv \frac{1}{f_{mnkl}} = \frac{\sqrt{\left\langle |F_m|^2 \right\rangle \left\langle |F_n|^2 \right\rangle \left\langle |F_k|^2 \right\rangle \left\langle |F_l|^2 \right\rangle}}{\left\langle F_m^* F_n F_k F_l^* \right\rangle} \tag{2.2-5}$$

The phase mismatch Δk_l is defined as

$$\Delta k_l = \beta_n + \beta_k - \beta_m - \beta_l \tag{2.2-6}$$

Thus, a scalar model of FWM involves Eq. (2.2-3) to Eq. (2.2-6). Eq. (2.2-3) defines the electrical fields of each of the four waves in the nonlinear mixing process. Eq. (2.2-4) is the coupled equations of FWM, which can be divided into three parts, SPM, XPM, and wavelength conversion. Eq. (2.2-5) shows the inverse proportionality of FWM nonlinearity to the effective area determined by the modal overlap. Therefore, the nonlinearities are different for SPM, XPM, and wavelength conversion due to the involvement of the different modes.

According to the law of energy conservation, there are two types of FWM, which can be explained with the concept of the photon interaction. One is a process in which three photons generate one photon or vice versa, as shown in Fig. 2.2-1(a). This type of FWM is difficult to observe in optical fibers due to poor phase-matching. Therefore, this type of FWM is neglected in the above derivation. The second type of FWM is a process in which two photons become two other photons, as shown in Fig. 2.2-1(b). This type of FWM can only occur when the two input photons are in-phase or at least coherent. For the ease of experimentation, this type of FWM can be further simplified to degenerate four wave mixing (DFWM), as shown in Fig. 2.2-1(c). DFWM can be realized by a single pump wave, and conventionally, the output two waves are called signal at shorter wavelength and idler at longer wavelength. The phase-matching condition for this case is achievable, and will

be discussed in the next section.

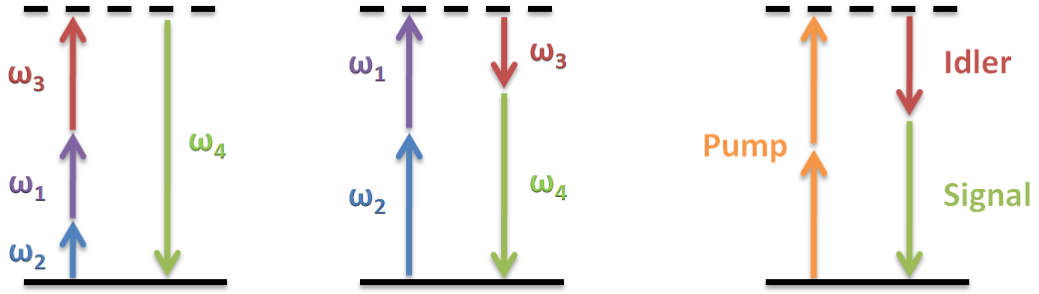

(a) (b) (c)

Fig. 2.2-1 FWM described by energy levels. (a) Three photons exchange for one photon. (b) Two photons exchange for the other two photons. (c) Degenerate case of (b)

To involve the influence of the competing nonlinearity, stimulated Raman scattering (SRS), a model of DFWM combined with the generation of the Stokes waves is derived. Due to the degeneracy of the two pumping wavelengths, the updated model can be quickly derived from Eq. (2.2-4) with this mathematical trick $\sqrt{2}A_1 = \sqrt{2}A_2 \Rightarrow A_1$. The following is the full scalar model of DFWM including the competing nonlinearity, SRS, for each wave:

$$
\begin{aligned}
\frac{dA_1}{dz} &= -\frac{1}{2}\alpha_1 A_1 - \frac{n_s\omega_{1s}}{c} f_{1s}\left|A_{1s}\right|^2 A_1 \\
&+ j\frac{n_2\omega_1}{c}\cdot\left(f_1\left|A_1\right|^2 A_1 + 2\cdot\sum_{k\neq 1} f_{1k}\left|A_k\right|^2 A_1 + f_{1134}A_1^* A_3 A_4\cdot e^{j\Delta kz}\right) \\
\frac{dA_3}{dz} &= -\frac{1}{2}\alpha_3 A_3 - \frac{n_s\omega_{3s}}{c} f_{3s}\left|A_{3s}\right|^2 A_3 \\
&+ j\frac{n_2\omega_3}{c}\cdot\left(f_3\left|A_3\right|^2 A_3 + 2\cdot\sum_{k\neq 3} f_{3k}\left|A_k\right|^2 A_3 + f_{3411}A_4^* A_1 A_1\cdot e^{-j\Delta kz}\right) \\
\frac{dA_4}{dz} &= -\frac{1}{2}\alpha_4 A_4 - \frac{n_s\omega_{4s}}{c} f_{4s}\left|A_{4s}\right|^2 A_4 \\
&+ j\frac{n_2\omega_4}{c}\cdot\left(f_4\left|A_4\right|^2 A_4 + 2\cdot\sum_{k\neq 4} f_{4k}\left|A_k\right|^2 A_4 + f_{4311}A_3^* A_1 A_1\cdot e^{-j\Delta kz}\right)
\end{aligned}
\qquad (2.2\text{-}7)
$$

$$\frac{dA_{1s}}{dz} = -\frac{1}{2}\alpha_{1s}A_{1s} + \frac{\omega_{1s}n_s}{c} f_{1s}|A_1|^2 A_{1s}$$

$$\frac{dA_{3s}}{dz} = -\frac{1}{2}\alpha_{3s}A_{3s} + \frac{\omega_{3s}n_s}{c} f_{3s}|A_3|^2 A_{3s}$$

$$\frac{dA_{4s}}{dz} = -\frac{1}{2}\alpha_{4s}A_{4s} + \frac{\omega_{4s}n_s}{c} f_{4s}|A_4|^2 A_{4s}$$

where A_{is} is the amplitude of the SRS wave induced by A_i, and n_s is the effective nonlinear refractive index of SRS [43].

This model is numerically solved with the finite-difference method. The input condition of the signal wave A_3, and the idler wave A_4 are both determined by the vacuum fluctuation [44], and the input conditions of their Stokes waves A_{3s} and A_{4s} are the product of the Stokes photon energy and the effective bandwidth of stimulated Raman scattering [45].

2.3 The challenges to achieve efficient wavelength conversion FWM

With Eq. (2.2-7) the wavelength conversion in large-mode-area optical fibers can be analyzed. The main challenges in attaining efficient FWM wavelength conversion in large-core fibers are (1) phase-matching between pump, signal and idler wavelengths, (2) the generation of fundamental-mode signal, which influence the output beam quality of the converted wave, (3) achieving efficient wavelength conversion at peak powers well below the threshold of other competing nonlinearities (SRS in particular), and (4) high attenuation at the idler wavelength (>2μm) due to the material absorption of fused silica. Our initial exploration addressed all four issues and determined conditions under which the use of a 28μm-core LMA fiber with 0.07 NA can achieve efficient and power scalable wavelength conversion from ~1μm (Yb-fiber operation range) down to the visible wavelength range.

2.3.1 Phase-Matching of Wavelength Conversion in LMA Fibers

Phase-mismatch induced by the dispersion is associated to the efficiency of FWM-wavelength conversion, and the dispersion can be from three different parts. The contribution of the phase-mismatch between the waves includes material dispersion, waveguide dispersion, and nonlinear phase modulation induced by SPM and XPM. Thus, the phase-mismatch can be written as $\Delta k = \Delta k_M + \Delta k_W + \Delta k_{NL}$, where Δk_M, Δk_W, and Δk_{NL} are the phase-mismatch caused by material dispersion, waveguide dispersion, and nonlinear phase modulation respectively.

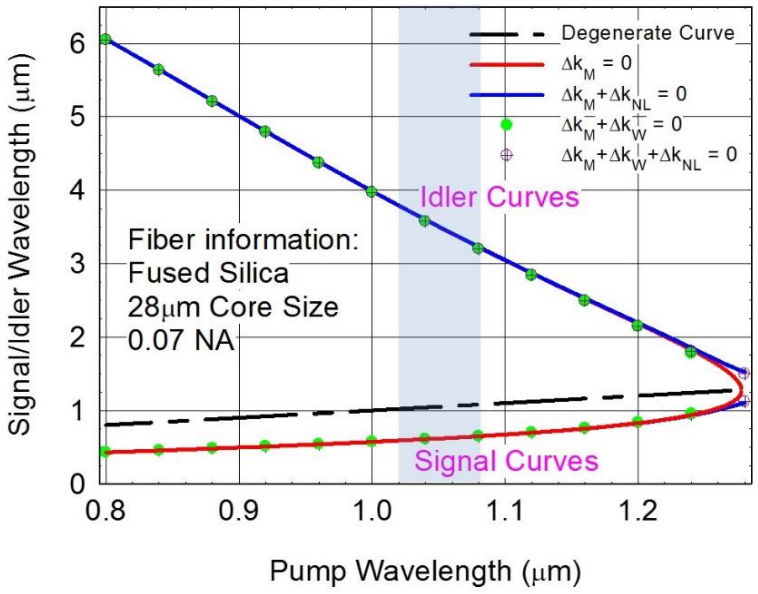

Fig. 2.3-1 The phase-matching diagram of a fused-silica fiber with 28-μm core and 0.07 NA

The fused silica dispersion characteristics favor the wavelength conversion from NIR-pump to visible-signal and MIR-idler. In Fig. 2.3-1, the phase-matching diagram of a fused-silica fiber with a 28-μm core and 0.07 NA is calculated. Being divided by the black dashed degenerate curve, the upper curves show the phase-matched idler wavelengths versus pump wavelengths, and the lower curves show the signal one. Four different combinations of phase-mismatch, from material dispersion ($\Delta k_M = 0$), from material dispersion and nonlinear phase modulation at 300kW pumping ($\Delta k_M + \Delta k_{NL} = 0$), from material and waveguide dispersion ($\Delta k_M + \Delta k_W = 0$), and from all three dispersions ($\Delta k_M + \Delta k_W + \Delta k_{NL} = 0$), illustrate only slightly different signal and idler phase-matching curves. The overlapping condition of these phase-matching curves indicates the dominance of material dispersion. One reason is that the waves are confined in the core of a LMA fiber which is closer to bulk rather than waveguide, thus the waveguide dispersion in the LMA fiber can be ignored. The other reason is attributed to the diminished nonlinearity by the

~22μm mode field diameter. Eq. (2.2-5) reveals that the nonlinearity is inversely proportional to the effective mode area, so the Kerr effect is diminished in a large-core fiber. Thus, with the exception of the phase-matching in the pumping wavelength range between 1.25μm to 1.28μm, the material dispersion alone can determine the phase-matching wavelengths of signal and idler. Around the degenerate wavelength ~1.28μm, which is also the zero dispersion wavelength, due to the phase-mismatch caused by the material dispersion is smaller or comparable to the Kerr nonlinear phase modulation, the degenerate point is split and this splitting is extended to the wavelength range of anomalous material dispersion. This condition is the so called modulation instability, which only occurs at wavelength in anomalous dispersion. All in all, as shown in Fig. 2.3-1, the material dispersion singly determines the phase-matching condition of wavelength conversion in a LMA fiber.

The above analysis concludes the phase matching of wavelength conversion in large-mode-area fibers. If the pump wave is launched from an ytterbium-doped fiber lasers which is usually operated between 1020-nm to 1080-nm wavelength (the blue marked area in Fig. 2.3-1), the output signal is red light (~650 nm) and the idler is MIR (~3.5μm). A significant result taken from this analysis is that as long as the pump wavelength is shorter than ~1.28 μm, the phase matching of wavelength conversion is definitely achievable.

2.3.2 The Modal Overlapping

In order to verify the output beam quality of the signal, the modal overlap is calculated with Eq. (2.2-5). The goal of this test is to confirm the nonlinearity of the wavelength conversion from the fundamental-mode (FM) pump wave to the FM signal wave and the

idler wave dominates. In the following calculation of modal overlap, the pump wave is assumed FM since the input excitation is always controllable. The idler wave is naturally FM due to the corresponding V-number at this wavelength is less than 2.405. Thus, the performance of multiple transverse modes can only happen to the signal wave. Fig. 2.3-2 shows the modal overlap integral including both the pump and the idler wave as FMs while the signal waves has varied orders of HOM, LP_{lm}. This figure shows the signal of FM (l +1 = 1, and m = 1) within a FWM process dominates it of other HOMs. This result predicts the output beam of the signal is diffraction-limited FM.

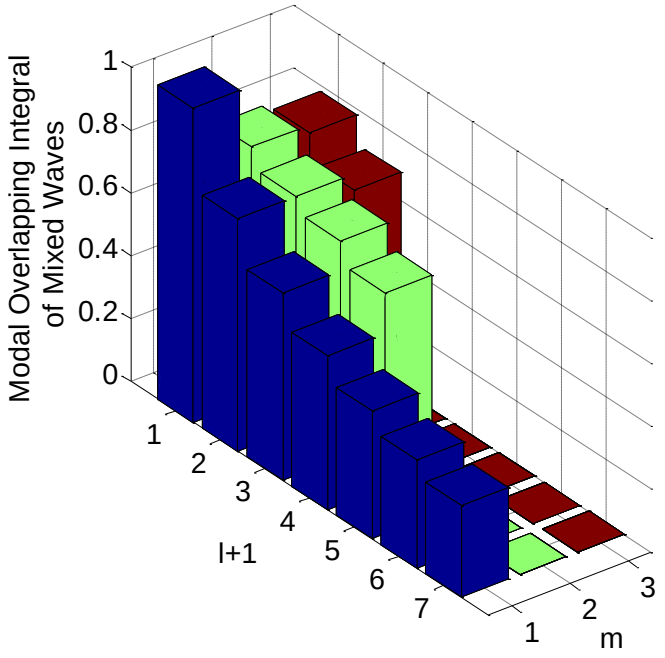

Fig. 2.3-2 Modal overlapping integral calculated with different modal numbers of the signal wave at 632 nm (Overlapping → Overlap)

The generation of single-mode signal is a critical factor to make use of this wavelength conversion technique for further applications. If the pump wave cannot maintain pure single-mode operation, both the efficiency of conversion and the output beam quality of

signal are degraded. Thus, the calculation, shown in Fig. 2.3-2, is especially meaningful when an effective single-mode fiber, such as a CCC fiber, is used as a medium to achieve the wavelength conversion, since the FM pump wave is naturally realizable.

2.3.3 Idler Loss

The confinement loss of wavelengths above 2 μm, which is the idler wavelength range, was believed too high, so no effort was made to further investigate the availability of efficient wavelength conversion by FWM in fused silica fibers. In Fig. 2.3-1, the 1064-nm pump wavelength determines the phase-matched signal is 632 nm, and the idler is 3372 nm, at which the fused silica has a strong absorption. Fig. 2.3-3 is the absorption spectrum taken from Ref. [46]. As shown in this figure, the material absorption at 3372 nm is ~70 dB/m. Thus, compared to the loss at this idler wavelength, that of the pump (~1 dB/km) or signal (<100 dB/km) is negligible.

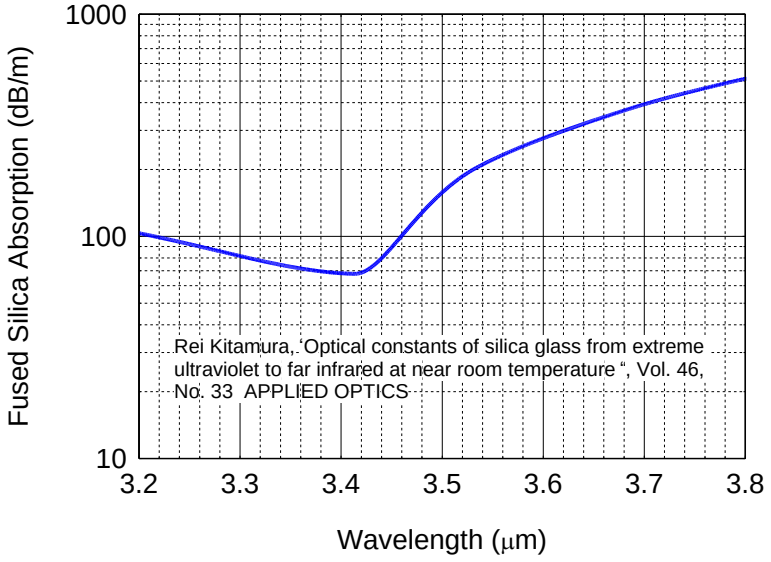

Fig. 2.3-3 The spectrum of fused silica absorption in the wavelength range of 3.2 nm-3.8 nm

This fact plausibly indicates a critical issue of efficient wavelength conversion by DFWM in fused silica fibers. However, the truth is that this level of idler absorption helps stabilize the generation of the signal wave, a characteristic that is verified with $\chi^{(2)}$ parametric oscillators [47]. The reason is conceptually explained as the following.

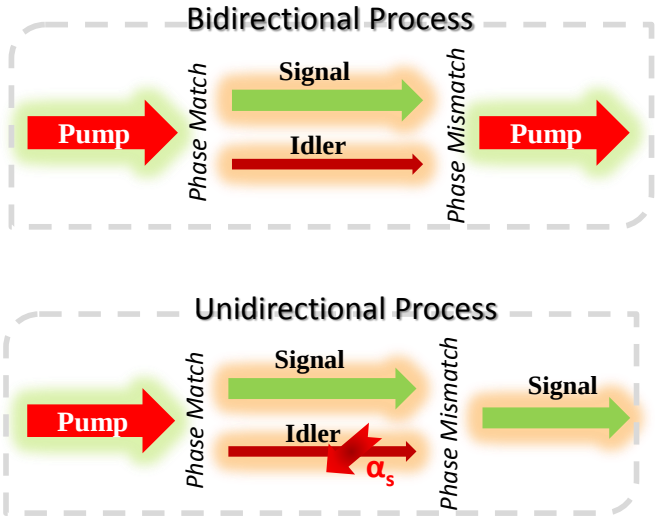

Fig. 2.3-4 Scheme of stabilizing the generation of signal waves by strongly absorbed idler

Due to the nonlinear phase modulation from SPM and XPM, the phase matching condition changes with the depletion of the pump waves as well as the increment of the signal and idler waves. Thus, when the power level of the pump waves is close to the signal and idler wave, the power flow is reversed due to the phase mismatch. This indicates a bidirectional process of the wavelength conversion in FWM, one is the nonlinear coupling from the pump to the signal and the idler and the other one is it from the signal and idler to the pump. This bidirectional process can be broken if one of the mixed waves is lossy. The scheme is shown in Fig. 2.3-4. The upper diagram depicts the generated waves of the signal and idler converted back to the pump wave due to the power-dependent nonlinear phase

modulation. The lower diagram shows that the back conversion is impeded due to the removed idler. This scheme can be applied in a limited range of idler losses (50-500 dB/m [42]), which indicates the 70 dB/m attenuation at 3372-nm idler wavelength actually favors the wavelength conversion to the visible signal.

In the next subsection, this attenuation level is used to simulate the power progression of DFWM in a fiber with 28mm-core and 0.07 NA. In this simulation, the other critical factor, SRS, which unavoidably influences the availability of the wavelength conversion is considered as well.

2.3.4 Competing Nonlinearity: Stimulated Raman Scattering

Stimulated Raman scattering is the other limitation of an efficient wavelength conversion by FWM. The two nonlinear processes, FWM and SRS, occur simultaneously in the fiber. Since SRS is automatically phase-matched, when the threshold of SRS is reached, the power would be downshifted by 13.2 THz. However, the nonlinear coefficient of FWM is larger than that of SRS by four times [15]. Thus, the FWM process is expected to be dominant within the small-signal-gain segment of the fiber [43]. In this segment, if the pump attenuation is not considered, the pump intensity is approximately undepleted. Thus, the nonlinear phase modulation, which is mainly determined by pump in this segment, is approximately constant. In other words, efficient wavelength conversion occurs due to the achievement of a stable phase-matching condition in this segment.

Due to the complexity of FWM combined with SRS, the model derived in Sec. 2.2 is numerically solved by finite difference method. In this simulation, the result of two pump wavelengths, one is at 1064nm and the other is at 1030nm, are compared, and the relevant

idler loss is also included. The role of the idler loss can influence the small signal gain of both the signal and the idler, but as with the concept discussed in the last subsection, it can also help stabilize the generation of the signal.

Fig. 2.3-5 shows the normalized power progressions of the pump, the signal, the idler, and the associated Stokes waves in the LMA fiber which is pumped by a 100-kW 1064-nm wave. This power progression in linear scale is shown in (a), and in logarithmic scale in (b) for comparison. The dashed line in (a) marks the position at which the SRS threshold is reached. This position determines the length of the fiber to be used for wavelength conversion. From (b), the small signal gain of both the pump and the signal can be observed, and the coherence length is thus measured to be ~0.9 m. However, the selected fiber length is longer than this due to the stabilizing process involving the idler loss which occurs at the transition of the small signal gain to the large signal FWM interaction. Selecting this fiber length avoids both the conversion from the signal to its Stokes wave and the mixture of the pump-Stokes wave to the signal. Fig. 2.3-5 shows the stabilized generation of 632-nm signal due to the 70-dB/m absorption of the 3372-nm idler wave. In addition, >30% conversion efficiency from the pump to the signal is obtained.

A contrasting group of simulations is shown in Fig. 2.3-6, where the pump wavelength is changed to 1030 nm, and the pump power is increased to 300 kW. Under this condition, the position, marked by the dashed line in (a), at which the signal generation is maximized is consistent with the fiber length with which the SRS is above threshold. This fact indicates that the domination of SRS is attributed to the loss of idler (~385 dB/m). This idler loss level effectively reduces the small signal gain of the signal and idler wave, and equalizes the generation of the signal and the Stokes wave from the pump in the large-signal-gain segment. Fig. 2.3-6 (b) shows that for the idler wave, the large signal gain of DFWM is

much smaller than its 385-dB/m absorption. Therefore, the generation is quickly saturated and all the other power is transferred to SRS, and the upper limit of the signal efficiency is confined by both SRS and the idler loss.

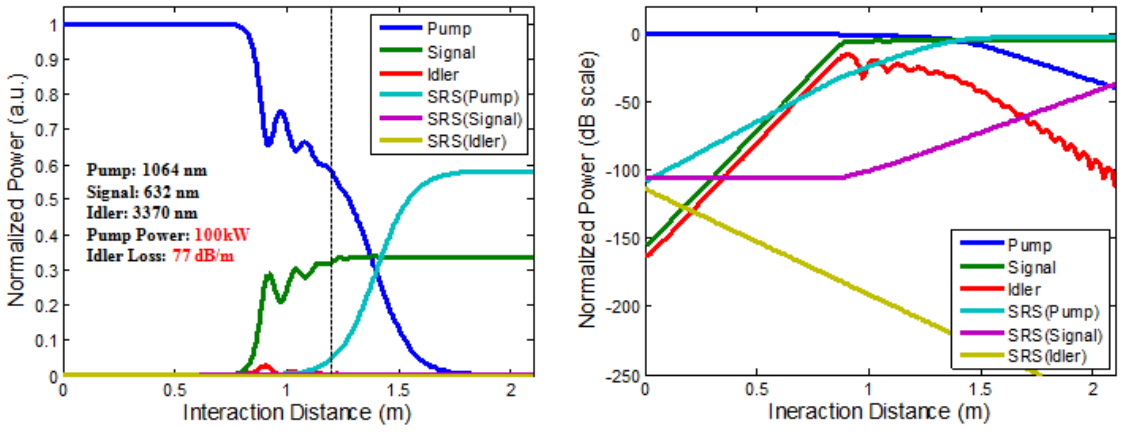

(a) (b)

Fig. 2.3-5 Normalized power progression in LMA fiber with 100 kW pump power at 1064 nm in (a) linear scale and (b) logarithm scale

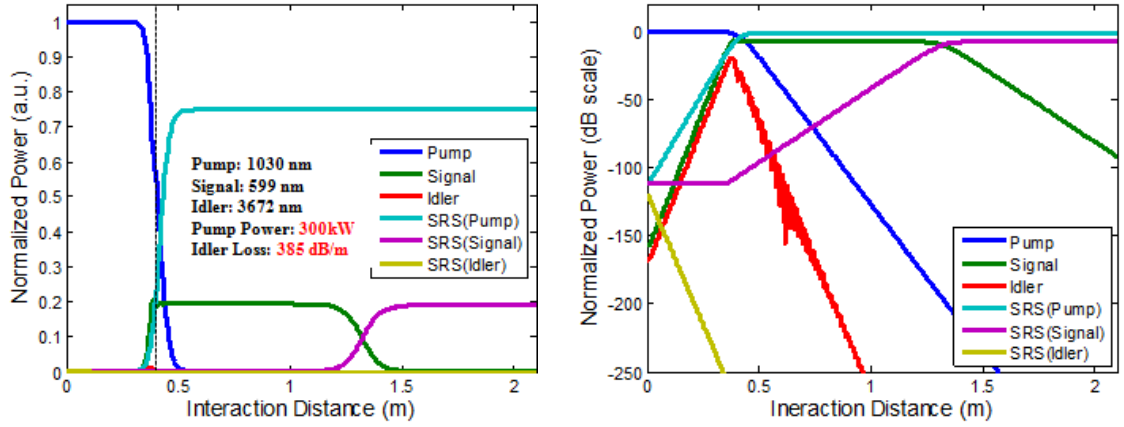

(a) (b)

Fig. 2.3-6 Normalized power progression in LMA fiber with 300 kW pump power at 1030 nm in (a) linear scale and (b) logarithm scale

From the above case study, the phase matching of DFWM, the proper loss level of the idler, and the suppression of SRS are three key factors for an efficient wavelength

conversion from near infrared- pump to visible-signal. This analysis helps to identify the avoidance of SRS by pumping at a particular wavelength range. Moreover, this analysis provides a systematic flow for determining the pump peak power and wavelength for the availability of achieving efficient FWM wavelength conversion with different fiber structures. However, in order to control the nonlinearity of FWM, the use of CCC fiber with tailored transmission spectrum and effective single mode performance is critical. The tailored transmission spectrum can be applied to suppress the competing nonlinearity SRS (introduced in the next chapter), and the effective single-mode performance can ensure a good beam quality for the converted signal.

2.3.5 Acceptable bandwidth of pump waves

The last factor which determines the conversion efficiency of the DFWM wavelength conversion is the bandwidth of the pump wave. In order to convert the pump wavelength to a specific signal wavelength with which the phase-matching is achieved, the bandwidth of the pump wave cannot be too broad. Otherwise, the phase-matching condition cannot be satisfied and the SRS would thus dominate DFWM. In the following paragraph, the acceptable bandwidth is derived from the small-signal-gain coefficient of the signal.

The small-signal gain coefficient can be derived from the DFWM model [15], and is given by

$$g = \sqrt{(\gamma P_1)^2 - (\kappa/2)^2} \tag{2.3-1}$$

where P_1 is the input pump power, and γ is nonlinear coefficient which is given by

$$\gamma = \frac{n_2 \omega_1 f_{1134}}{c} \tag{2.3-2}$$

Here we can equalize f_{1134} to $1/A_{eff}$, the reciprocal of FWM effective area. κ is the entire phase mismatch

$$\kappa = \Delta k + 2\gamma P_1 \tag{2.3-3}$$

From this equation, we can conclude that *g* exists only if

$$-4\gamma P_1 \le \Delta k \le 0 \tag{2.3-4}$$

Assuming the wavelength of the signal and the idler are fixed, the range of Δk, shown in Eq. (2.2-4) determines the bandwidth of pump wave as

$$\delta\Delta k \approx \frac{\partial \Delta k}{\partial \lambda}\delta\lambda = \frac{\partial k_p}{\partial \lambda}\delta\lambda_p \tag{2.3-5}$$

, so that the effective bandwidth of the pump wave can be derived as

$$\delta\lambda_p = \frac{\delta\Delta k}{\partial k_p / \partial \lambda} = \frac{4\gamma P_1}{\left(\partial k_p / \partial \lambda\right)\Big|_{\lambda=\lambda_p}} = \frac{4n_2\omega_1 P_1}{cA_{eff}\left(\partial k_p / \partial \lambda\right)\Big|_{\lambda=\lambda_p}} \tag{2.3-6}$$

Eq. (2.3-6) indicates that the acceptable pump bandwidth depends on the pump power P_1 and the effective area A_{eff}. The effective area is associated to the core diameter of a step-index fiber. Thus, we can also use the core diameter to characterize the acceptable pump bandwidth. Fig. 2.3-7 shows the acceptable pump bandwidth characterized with both pump power and the core diameters of a 0.07-NA step-index fiber and operated at 1.064-μm wavelength.

The pump bandwidth indeed limits the availability of an efficient wavelength conversion by DFWM in LMA fibers. In general, the acceptable pump bandwidth is proportional to the pump power and inversely proportional to the core size with a fixed NA. Therefore, the generation of the signal wave is associated both to the design the pumping source and the pumped passive fiber. According to Fig. 2.3-7, the acceptable pump bandwidth is around 15-pm for a hundred kilowatt peak power pumping 30-μm-core fiber.

Thus, one can estimate, from the time-bandwidth product 0.44 for Gaussian-shaped transform limited pulse [48], that depending on the fiber parameters, a high-peak-power- and hundreds of ps- transform-limited pulse is suggested as the pumping source.

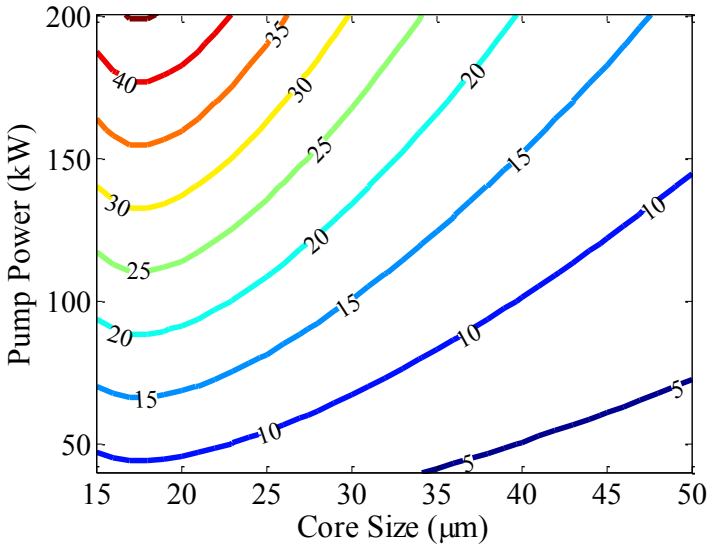

Fig. 2.3-7 Simulated acceptable pump bandwidth measured in picometer at different pump power and core diameter of a step-index fiber with 0.07 NA and operated at 1.064-μm wavelength

This calculation of the acceptable bandwidth is an approximation, since the above derivation is based on the small-signal gain of DFWM. In order to verify these equations, the acceptable bandwidths of the pump wave in two published experiments of DFWM in LMA fibers are calculated [41,42]. In Nodop's experiment in 2009, the pump bandwidth is < 4 pm, and the conversion efficiency from 1064-nm pump light to 673-nm signal light is 35%. With Eq. (2.3-6), the calculated acceptable bandwidth of the pump wave in this experiment is 72.3 pm, which is much larger than 4 pm. As for Jauregui's experiment in 2012, The bandwidth of the pump light is 6.6 pm, and the calculated acceptable bandwidth is 42.9 nm. In this experiment, 30% conversion efficiency to 672-nm signal is demonstrated.

As a result, it can be inferred that in order to achieve high conversion efficiency, the actual pump bandwidth needs to be much smaller than the acceptable bandwidth. The reason can be derived from the bandwidth broadening due to SPM. This factor indeed needs more investigation.

2.4 Summary

In this chapter, a DFWM model combined with SRS and a systematic method of analyzing the availability of DFWM wavelength conversion in LMA fibers are built. The procedure of this analysis includes 5 aspects: 1) the availability of phase-matching between 3 very different wavelengths, 2) the generation of FM-signal in a DFWM process, 3) the large idler loss, 4) the influence of SRS, and 5) the acceptable bandwidth of the pump wave. The dispersion characteristic of fused silica specifically favors the occurrence of DFWM, while waveguide dispersion and nonlinear dispersion can almost be ignored in LMA fibers. Thus, the phase matching of DFWM generation in LMA fused-silica fibers is achievable. A simple calculation of the modal overlap indicates the domination of FM-signal to other HOM-signals when the pump wave is excited as FM. The attenuation of the idler wave actually helps the stabilization of the signal generation due to the impeded bidirectional wavelength conversion caused by phase-mismatch caused by the depletion the pump wave. The detrimental SRS, by properly choosing the pump peak power and fiber length, can be avoided because the growth of SRS is weaker than DFWM in the small-signal-gain segment of the fiber, since the phase matching condition is automatically achieved. In order to further improve the performance of the wavelength conversion, the CCC technique of SRS-suppression, which will be introduced in the next section, is suggested for realizing more efficient DFWM. The analysis of the acceptable pump bandwidth indicates that the selection of the pump wave depends on both pumping power and the fiber structure. For achieving an efficient wavelength conversion, a high-peak-power, hundreds of pico-second transform-limited pulse is required.

Chapter III

Suppression of Stimulated Raman Scattering in CCC Fibers

3.1 Introduction

In general, the achievable signal power in a fiber laser or amplifier is constrained by various optical nonlinearities occurring in an optical fiber at high optical intensities and sufficiently long propagation distances. There are many types of optical nonlinearities that can occur in high-power fiber lasers, amplifiers, or delivery fibers: stimulated Brillouin scattering, stimulated Raman scattering, self-phase modulation, thermal multimode instabilities, etc. Usually the type of dominant nonlinearity is primarily determined by a signal format. For example, for high power broadband signals, both continuous-wave and long pulse, dominant nonlinearity is stimulated Raman scattering (SRS) [15,49]. Once the SRS threshold is exceeded, most of the power will transfer to the unwanted Stokes wave at a longer wavelength, thus strongly degrading system performance.

A straightforward path to increasing SRS threshold is to reduce fiber length, thus reducing nonlinear interaction length. This solution, however, leads to a trade-off in high power systems between increasing nonlinearity-limited achievable signal power or energy and the long fiber length required for effective heat dissipation. A somewhat less straightforward path is to increase fiber core size, thus reducing optical intensity. Since

increasing core size in conventional fiber structures eventually leads to an undesirable multimode performance, this path initiated development of several advanced large-core fiber designs specialized for preserving single mode operation [50,51,52] - a general approach to reducing nonlinear interactions. Over the last several years, however, a new approach had emerged specialized for increasing SRS threshold by inducing Stokes-wave loss in an optical fiber. Several approaches have been proposed and demonstrated such as bending-induced loss filtering [53], single-mode dual-hole-assisted fibers [54], W-type core fiber with fundamental mode cut-off [55], filter fiber based on the loss in coupled ring modes [56,57], and specially designed photonic bandgap fibers [58,59,60,61]. However, these schemes are not compatible with large-core single-mode preserving fiber designs, and, therefore, with a general technological direction of increasing core size for scaling up achievable powers and energies.

Recently, a possibility to spectrally tailor the transmission in a single-side-core chirally coupled core (CCC) fiber to induce SRS Stokes-wave loss has been identified and explored theoretically [38,39], showing that one can design a large core fiber which combines both the effectively-single mode propagation and the SRS suppression. In this chapter we demonstrate this combined performance experimentally with two different types of CCC fibers: with a "conventional" single-side CCC fiber with approximately 33 μm core, and with a polygonal-CCC fiber with 60 μm core. SRS suppression in the later structure represents a significant conceptual and quantitative extension of this previously work.

3.2 SRS Suppression by Induced Stokes-Wave Loss

Many relevant techniques of SRS suppression in long optical fibers have been demonstrated in these several years. The common concept of these approaches is inserting Stokes-wave loss in optical fibers. As mentioned in the section of introduction, there are five primary schemes of inducing loss at Stokes wavelength. So far, these schemes indeed play important roles in approaching SRS suppression for various scientific purposes and applications. However, to implement SRS suppression through Stokes-wave loss, not only is the fiber needed to be lossy around Stokes wavelengths, but the loss spectral profile around the cut-off wavelength needs to be steep thus providing strong enough discrimination between pumping waves and corresponding Stokes waves.

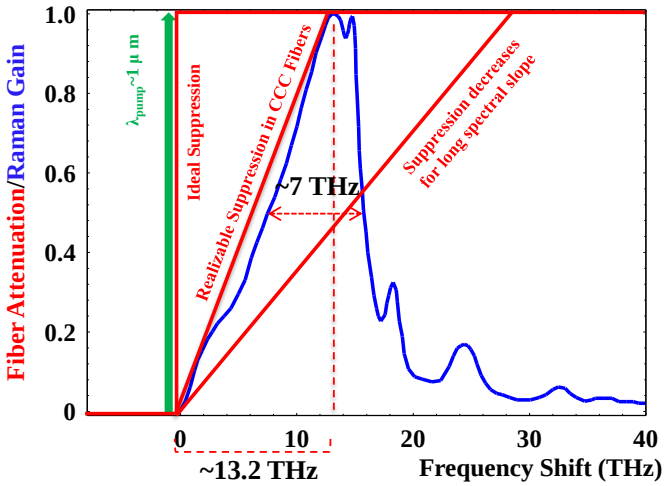

Fig. 3.2-1 Fiber attenuation profile for the concept of SRS suppression, which includes the profile of the Raman gain of silica material shown as the blue curve and three different degrees of SRS suppression showns as the red curves.

In Fig. 3.2-1, the spectrum of the normalized Raman gain and it of three different types of fiber attenuation are shown. This figure conceptually shows the slope of the loss

spectrum is an important factor of achieving effective SRS suppression. The ideal spectrum of fiber attenuation is a step function which covers the whole gain spectrum of SRS while keeping the attenuation of the pump wave small. However, normal specialty fibers can only support finite slope of the attenuation. As shown in Fig. 3.2-1, the slope of the Stokes-wave attenuation should be as short as 13.2 THz (~50 nm) to provide enough pump-to-Stokes discrimination thus leading to an effective SRS suppression as the pump wavelength is around 1μm. When the slope is longer than 13.2 THz, the suppression decreases and is not capable of suppressing SRS effectively. Two good examples are associated to the method of bending normal step-index fibers [53] and W-type fibers [55] would lead to a large loss at the Stokes wavelength, but they cannot provide sharp cut-off edge between the pump wavelengths and its Stokes wavelengths. Therefore, bending makes the differentiation between the pump waves and the Stokes waves difficult. In addition to the attenuation slope of the Stokes waves, the peak attenuation is the other factor of achieving effective SRS suppression. Although dual-hole-assisted fibers [54], filter fibers [56,57] and PCF [58,59,60,61] favor steep cut-off edges between the pump wavelength and its Stokes wavelength, the SRS attenuation of these fibers is only mild (<5dB/m). The reason of this judgment is based on a simple estimation. The peak power gain coefficient of SRS can be found as $g_R I_0$ [15], where $g_R \left(\sim 10^{-13} W/m\right)$ is the peak gain coefficient of SRS for fused silica, I_0 is the peak intensity of the pump wave. Therefore, the optimized attenuation for effective SRS suppression in fused silica fibers can be estimated as

$$\alpha_p = 10\log_{10}\left(e^{g_R I_0}\right) \cong 4.34 g_R I_0 \qquad (3.2\text{-}1)$$

In Fig. 3.2-2, the estimated peak attenuation of the Stokes waves for effective SRS suppression is calculated. This figure shows that under <5 dB/m Stokes-wave attenuation,

even if the mode field diameter of the fiber is as large as 70 μm, an effective SRS suppression can only occur around 10-kW pump power. For a normal 10-μm-MFD photonic bandgap fiber, <5 dB/m Stokes-wave attenuation can only support to achieve effective SRS with below 1-kW pump power.

On the other hand, all these five schemes are demonstrated with relative small-core fibers, and this issue leads them difficult to be implemented their SRS-suppression performance to high power or high energy regime. To explore the solution of realizing SRS-suppression in large-mode-area (LMA) optical fibers, we adopted the properties of spectrally-tailored transmission spectrum in chirally-coupled-core (CCC) fibers, which is demonstrated to have steep enough attenuation slopes as well as strong enough attenuation peaks at Stokes wavelengths. Moreover, since CCC fibers are also known as the effectively-single mode propagation with large core scale, its potential on high-power or high-energy applications is highlighted.

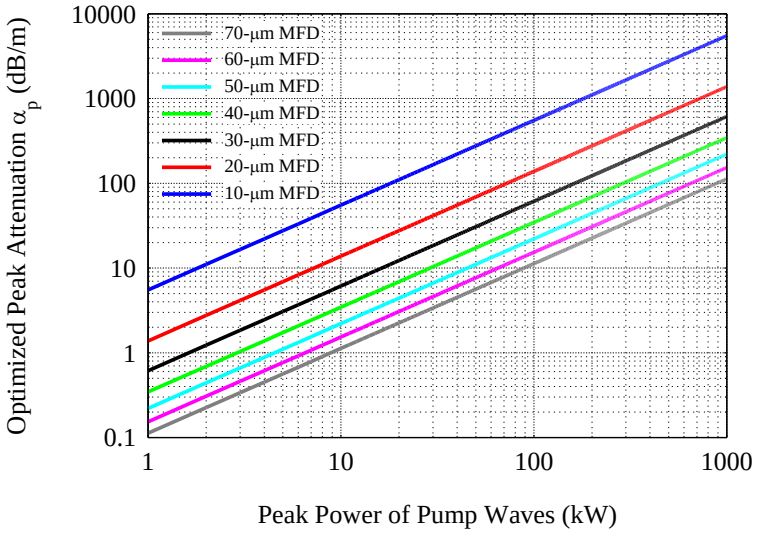

Fig. 3.2-2 Estimation of the required peak attenuation of the Stokes waves for effective SRS suppression

3.3 SRS Threshold in LMA Fibers with Stokes-Wave Loss

When a fused silica optical fiber is pumped with a high-intensity wave, stimulated Raman scattering seeded by spontaneously-generated Stokes waves occurs. In this process, the pump power is exponentially transferred to the Stokes wave, which is at 13.2 THz frequency lower than the pump. The threshold P_{th} of this phenomenon is defined as the power level of input pump wave which leads to that the output pump-wave power equals to the output Stokes wave [45]. Mathematically, this definition can be shown as

$$P_s(0)\cdot e^{-\alpha_s L+P_{th}g_R L/A_{eff}} = P_{th}\cdot e^{-\alpha_p L} \tag{3.3-1}$$

where g_R is the Raman gain coefficient, $P_s(0)$ is the power of the Stokes wave generated from spontaneous Raman scattering, α_p and α_s are the loss of the pump wave and the Stokes wave, *L* is the fiber length, and A_{eff} is the effective area of transverse mode supported in the fiber. For single-mode fibers, the solution of Eq. (3.3-1) with assuming equivalent attenuation of pump and signal waves ($\alpha_p = \alpha_p \equiv \alpha$) gives the well-known expression for SRS threshold

$$P_{th} \approx \frac{16A_{eff}}{g_R L_{eff}} \tag{3.3-2}$$

where L_{eff} is the effective length defined by

$$L_{eff} \equiv \frac{1-e^{-\alpha L}}{\alpha} \tag{3.3-3}$$

However, for large-mode-area fibers, the SRS threshold calculated with Eq. (3.3-1) cannot be precise anymore. The coefficient *16* in Eq. (3.3-2) should be corrected when the threshold of SRS in a LMA fiber is calculated. The updated coefficient in Eq. (3.3-2) can

be calculated by going through the derivation steps in [45] and substituting the LMA-fiber parameters. Fig. 3.3-1 shows the calculated coefficient at different mode-field diameters and threshold power. The curves in Fig. 3.3-1 reveal the coefficient is not sensitive to the mode field diameters as well as the threshold level. Therefore, a reasonable approximation of this coefficient for LMA fibers can be chosen from 27 to 30, and Eq. (3.3-2) is thus rewritten as

$$P_{th} \approx \frac{CA_{eff}}{g_R L_{eff}} \tag{3.3-4}$$

where C is from 27 to 30. The exact coefficient depends on the threshold level.

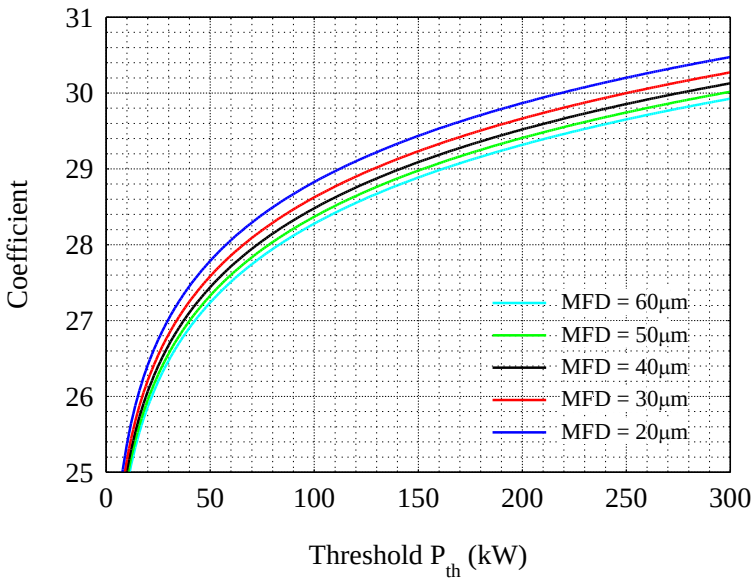

Fig. 3.3-1 The updated coefficient in the formula of SRS threshold with different trial SRS threshold level

When the Stokes wave experiences large loss while the attenuation of the pump wave is negligible, following the same process as above, Eq. (3.3-4) can be further modified as [62]

$$P_{th} \approx \frac{CA_{eff}}{g_R L} + \frac{\alpha_s A_{eff}}{g_R} \tag{3.3-5}$$

Eq. (3.3-5) shows that the increment of the SRS threshold is independent of the Stokes wave attenuation. Therefore, the propagation length-independent SRS threshold $P_{th} \approx \frac{\alpha_s A_{eff}}{g_R}$ is predicted as taking $L \to \infty$ [62]. This concept recapitulates the importance of distinguished attenuation from the Stokes wave to the pump wave.

3.4 The Stokes Attenuation in CCC Fibers

In this research work, a new technique of SRS suppression based on novel chirally-coupled-core (CCC) fibers is proposed and is demonstrated. CCC fibers are constructed by a central core and at least one side core. Thus, it is a dual-waveguide system if all the side cores are viewed as an integrated waveguide in which the side-core modes interact with the central-core ones. Based on the phase-matching of inter-waveguide or intra-waveguide modal coupling [38,39], the helical system of CCC fibers allows a spectrally tailored transmission spectra for fundamental mode as well as higher-order modes. Therefore, effective single mode delivering can be achieved under appropriate structural design. The suppression of SRS is realized by manipulating the phase-matching condition at Stokes wavelength. At this wavelength, the Stokes wave generated in the central core would be coupled to the side cores. Due to the helical geometry of the side core, the frustrated total internal reflection leads to large attenuation of the propagating waves there. For example, if the coupling between the fundamental mode LP_{01} in the central core and the higher-order mode LP_{11} mode in the side core at the Stokes wavelength is phase-matched, the SRS generated by the signal of LP_{01}-mode would be coupled to the side core as LP_{11} mode. This LP_{11} mode is efficiently dissipated via the frustrated total internal reflection thus resulting in SRS suppression. The ability of SRS suppression based on the individual characteristic of CCC fibers has been demonstrated numerically [62]. This literature mainly focuses on the concept of propagation-length-independent SRS threshold which is conceptually explained in Eq. (3.3-5).

For the two specially-designed Ge-doped CCC fibers, one is with 33-μm and the other is with 60-μm core size, the fiber attenuation spectra of the FM are shown in Fig. 3.4-1. In this figure, the method of suppressing SRS in a 33-μm and a 60-μm spectrally-tailored

CCC fiber is shown with the SRS gain spectra. One can observe that in these two figures, the designed CCC fiber transmission spectrum matches the spectral profile of SRS gain coefficient in fused silica material for pump wavelengths at 1085 nm and 1040 nm respectively. In Fig. 3.4-1 (a), a distributed 30-dB loss covers the peak of the Raman gain and the ~40nm-long slope of the attenuation curves is qualified for the criteria of achieving effective SRS suppression. While in Fig. 3.4-1 (b), the estimated Raman-suppression loss is as high as 45-dB with a 20-nm attenuation band. As calculated from Eq. (3.2-1), the required peak attenuation for these two CCC fibers to suppress SRS is 37.6 and 43.8 dB/m respectively, so the SRS-suppression performance of these two CCC fibers is predicted. By exploiting the property of modal attenuation in these two CCC fibers with different core sizes, we present the first experimental verification of the SRS suppression in CCC fibers by comparing the output spectra of the launched high-peak power nanosecond pulses through these two CCC fibers, and each pumped by two different wavelengths, one with and another without Stokes-wave loss.

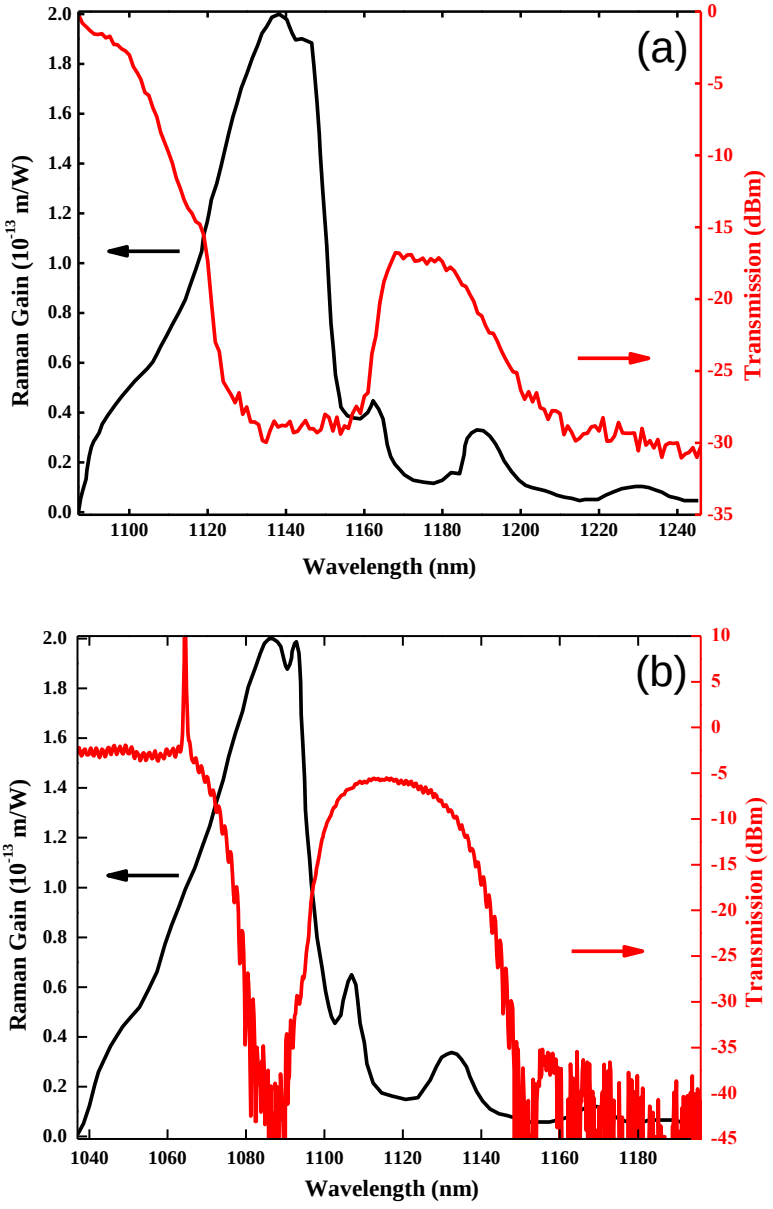

Fig. 3.4-1 (a) The 33μm-core CCC fiber sample's transmission spectrum from 1087nm to 1246nm with red solid line and vertical axis on the right is shown to match the Raman Stokes gain of pump wavelength at 1087nm. (b) The 60μm-core CCC fiber sample's transmission spectrum from 1037nm to 1097nm with red solid line and vertical axis on the right is shown to match the Raman Stokes gain of pump wavelength at 1040nm. Both figures are plotted as a function of wavelength with black solid line and vertical axis on the left.

3.5 Experimental Design

The experimental layout is shown in Fig. 3.5-1. This setup consists of four parts: an oscillator, two stages of single-mode pre-amplifiers, a CCC fiber-based high power amplifier, and a passive fiber under test (FUT). The output beam from FUT is coupled to a single-mode fiber which is connected to an optical spectrum analyzer for measuring the output spectra.

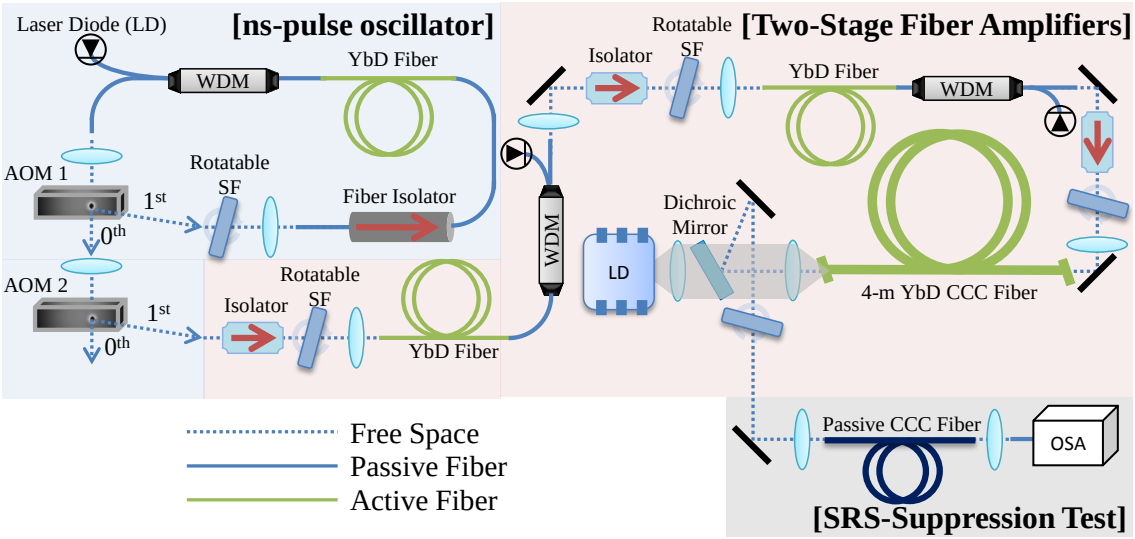

Fig. 3.5-1 Compact view of experimental setup: pulse generator, two stages of Ytterbium-doped fiber amplifiers, and the set-up of SRS-suppression test. (LD: laser diode, YDFA: ytterbium doped fiber amplifier, WDM: wavelength division multiplexing, AOM: acoustic optical modulator)

In order to explore SRS suppression in CCC fibers at different wavelengths and varied ranges of peak power, a wavelength and repetition rate-tunable oscillator is required. The oscillator in the experimental setup, which provides ns-pulsed signals to the first stage of the pre-amplifier, consists of a gaining cavity, a rotatable laser-line filter made by Semrock and two acousto-optic-modulators (AOM). The tunable wavelength of the signal is achieved by rotating the laser-line filter to change the incident angle, and the tunability is

from 1064 nm down to 1020 nm when incident angle is changed from 0° to 35°. If the longer wavelength (>1064 nm) is needed, this Semrock filter can be replaced with a band-pass filter which works at longer wavelength, such as of 1085 nm or 1095 nm. As for the repetition-rate tunability, it is attributed to the in-cavity AOMs which controls the cycle of the pulse. The other one is to filter the amplified-spontaneous-emission (ASE). Both AOMs are electrically controlled by the Stanford digital delay generator DG-535, with which the repetition rate can be changed from 1 mHz to 1MHz.

The development of the nanosecond pulses resembles the ring-cavity regenerative amplification. The 1st-order beam from the intra-cavity AOM is used to close the ring loop, and the 0^{th}-order beam is for dumping out the pulses. As depicted in Fig. 3.5-2, the detailed temporal electronic control of the optical-wave modulation is shown for both intra-cavity and extra-cavity AOMs.

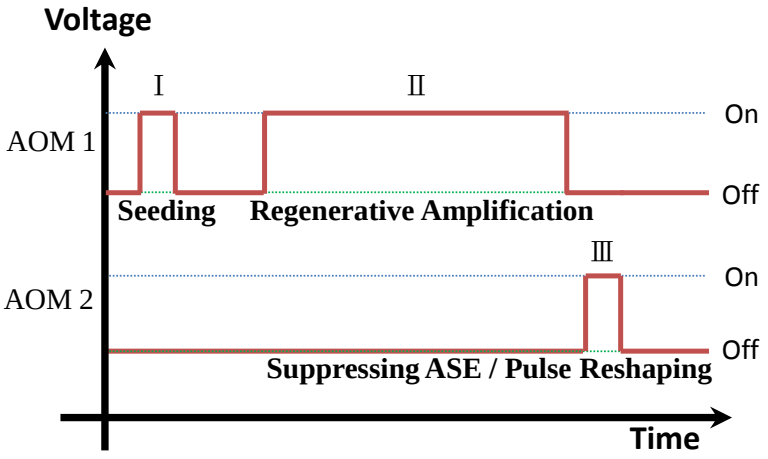

Fig. 3.5-2 The electronic control of both AOMs in each cycle. I: shaping the cintinuous-wave ASE as a pulse and sending back into the loop; II: closing the loop for a regenerative amplification of the pulse until the gain is saturated; III: reshaping the pulse and suppressing the background ASE

The electronic control of the two AOMs in each cycle is divided into three parts. (I)

The ASE is carved out with the length of this period, and this carved pulse is sent back into the loop for a further amplification. This period is 10-20 ns. (II) The intra-cavity AOM that is turned on in this period permits several roundtrips of the self-seeded ASE pulse until the pulse energy saturates, and then the loop is opened for dumping the saturated pulse out of the cavity. The number of the round trips is dependent on the wavelength. Each round trip takes 110 ns. (III) The extra-cavity AOM is used to clean up the dumped pulse from the mixture of the ASE, and output as at the 1st-order beam. The generated pulse from this oscillator is down to 10 ns as a minimum, which is limited by the rise time of the intra-cavity AOM.

Since this oscillator was built for testing nonlinear phenomena in CCC fibers, even though it possesses the value of being researched further, its full performance was never thoroughly investigated. The tuning range of the wavelength is only demonstrated from 1020nm up to 1090nm, and this range covers most of the useful Yb-doped fiber amplifier gain. The tuning range of the repetition rate was only demonstrated from 1 kHz to 10 kHz. Considering the trade-off between the influence of the ASE at low repetition rate and the achievable peak power in the amplifier stages at high repetition rate, 5 kHz is chosen in this SRS-suppression experiment. This oscillator allows an output around several hundred μW up to few mW of average power at the demonstrated range of wavelengths and repetition rates. At the output end of this pulse generator, a rotatable wavelength filter is used to block the rest of ASE and SRS which cannot be eliminated by the 2^{nd} AOM.

The output pulse from the programmable oscillator serves as the signal seed and is further amplified in the next three stages of ytterbium-doped fiber amplifiers (YDFA). This amplification system is consist of two single-mode Yb-doped fiber preamplifiers and a 4-m Yb-doped CCC fiber amplifier with 38-μm core size (30-μm mode-field diameter),

producing nanosecond pulses with a peak power up to 200 kW. The achievable peak power of this active-CCC fiber based amplifiers is also dependent on wavelength. Since this is the final stage of amplification and the output beam is used to characterize the SRS generation in a passive fiber, a SRS-free signal along this amplifier is important. The SRS threshold of this fiber amplifier is estimated by the highest gain which can be provided by the active Yb-doped CCC fiber. At 1040-nm wavelength, the highest gain is around 23dB, which corresponds to a 0.75 m effective length. Using Eq. (3.3-4), the threshold is calculated as 290 kW, which is higher than the achievable output peak power. Moreover, the output spectrum of the strongest pulses at 1040 nm are also measured to doubly confirm this amplifier to be SRS-free.

In order to more accurately demonstrate the SRS-suppression capability of CCC fibers, as shown in Fig. 3.5-1, a filter is placed at the output end of the CCC-fiber based YDFA to further block the small amount of SRS- and ASE- mixture. The output signal from the stage of CCC-YDFA is sent into the passive CCC fibers, and the output spectra from these passive fibers are measured by an optical spectrum analyzer (OSA).

3.6 Experiment Result and Analysis

3.6.1 38- μm-core CCC Fiber

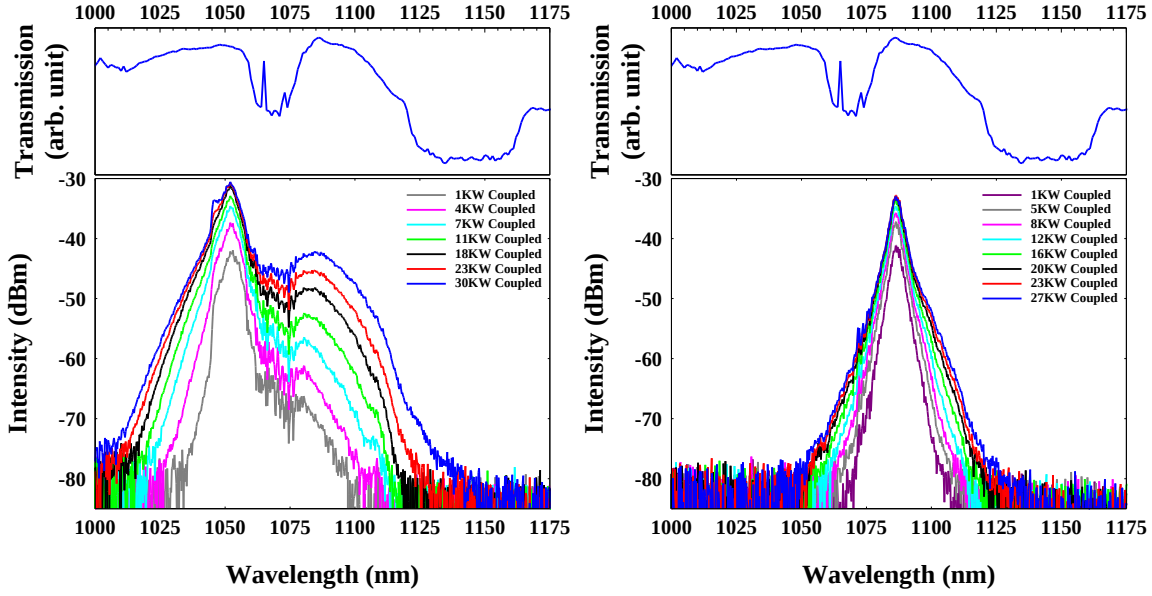

(a) (b)

Fig. 3.6-1 Output Spectrum versus coupled input peak power. (a) 1052nm pump wavelength with 7nm bandwidth. (b) 1087nm pump wavelength with 4nm bandwidth. The inset shows the transmission spectrum of the tested CCC fiber.

The first passive CCC fiber under test is a 6-m long Ge-doped CCC fiber with the core size of 33 μm and the NA of 0.06. The measured mode-field diameter of this CCC fiber is 21 μm. The SRS threshold in this fiber is calculated as the following. The pump-wave attenuation of these two wavelengths is 1dB/m, so the effective length is 3.1 m. The gain factor *C* in the SRS threshold formula is selected as 27. The Raman Stoke gain coefficient of Ge-doped fused silica is 2 times larger than usual fused silica fiber and is chosen to be 2×10^{-13} W/m [63,64], which is calibrated in all of the measurement. Using Eq. (3.3-4), the SRS threshold is estimated as 15.5 kW under no SRS suppression.

SRS suppression is demonstrated with this fiber by launching high peak power into the fiber at two different wavelengths. The pumping wavelength at 1087 nm is with SRS suppression, while it at 1052 nm is without SRS suppression. The measured output spectra are recorded and shown in Fig. 3.6-1. For clarifying the picture of the SRS-suppression, the transmission spectrum of this 33-μm Ge-doped CCC fiber is placed on the top of the figure which shows the evolution of the output spectra versus different pumping peak powers at the two selected pump wavelengths. For both cases, the coupled peak powers into the CCC fiber is up to 30 kW, which exceeds the calculated SRS threshold, 15.5 kW. The spectra in this two cases shows significantly different characteristics. The SRS growth is shown at 1052-nm pumping, while a complete absence of observable SRS is shown at 1087-nm pumping. In order to quantify this difference, for each spectrum shown in Fig. 3.6-1 (a) and (b) respectively, an integral of the spectral power ratio of the wavelengths longer than the signal wavelength by 23 nm to it of the total measured spectrum is practiced for each power level, and shown in Fig. 3.6-2. This result shows that SRS is indeed suppressed at all tested peak powers by the tailored loss profile of this CCC fiber, while without suppression SRS power appears to grow starting from few-kW peak powers. Furthermore, what is also worthy of noting is the small amount of spectral broadening associated with non-phase-matched four-wave-mixing (FWM). This induced spectral broadening appears to be suppressed for 1087-nm pumping due to the fact that this signal is “sandwiched” between two spectral transmission “dips”. While for the case of 1052-nm pumping, due to the mixture of the sideband seeded non-phase-matched FWM and SRS at the integrated wavelengths, the fraction curve shows a quadratic growing in Fig. 3.6-2.

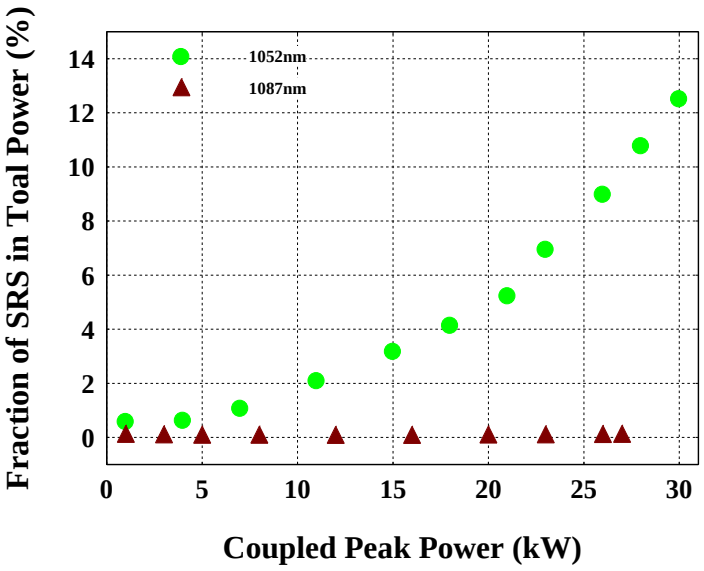

Fig. 3.6-2 The power fractions of the integrated components according to wavelength longer than 1075 nm in fig 7 (a) and the integrated components according to wavelengths longer than 1110nm in fig 7 (b) versus coupled peak power

3.6.2 60-μm-core CCC Fibers

For the purpose of realizing SRS suppression with high-power facilitation, a CCC fiber with a doubled core size is put under test. This fiber was a 4-m long Ge-doped CCC fiber with a core size of 60 μm and NA of 0.06. The measured mode-field diameter around 1-μm wavelength is 46 μm. The attenuation for both of these pump wavelengths, 1040 nm and 1060 nm, is 0.5dB/m, and this corresponds to 3.1-m effective length and 77-kW SRS threshold when no SRS suppression is onset. This SRS threshold is calculated with selecting the gain factor C as 29.

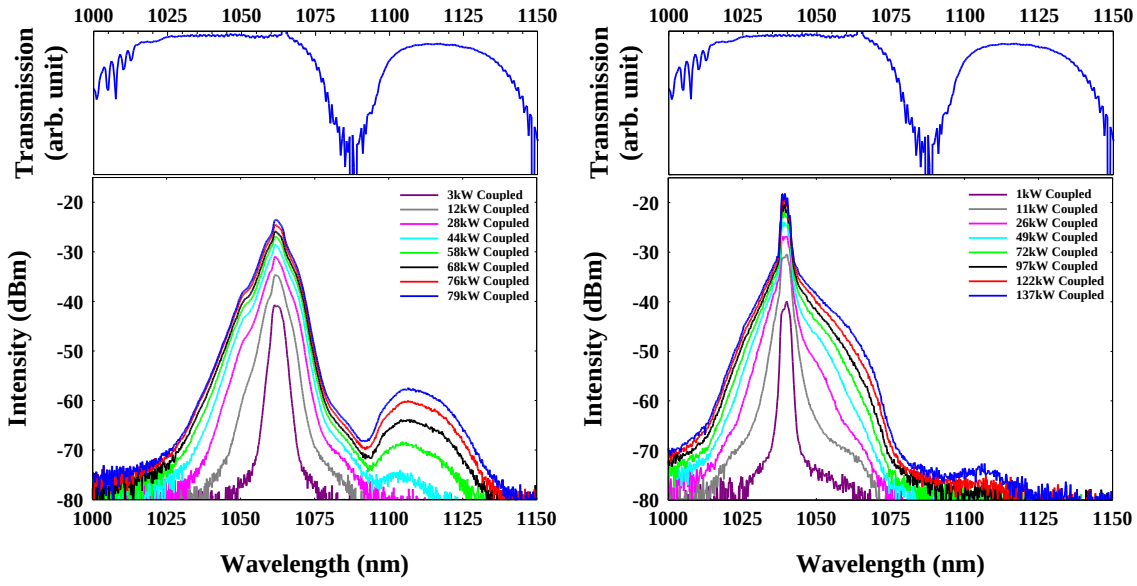

(a) (b)

Fig. 3.6-3 Output Spectrum versus coupled input peak power. (a) 1060nm pump wavelength with 7nm bandwidth. (b) 1040nm pump wavelength with 4nm bandwidth. The inset shows the transmission spectrum of the tested CCC fiber.

With a similar experimental process, the 60μm-core CCC fiber was tested with pumping wavelength at 1060 nm and 1040 nm respectively. Fig. 3.6-3 (a)-(b) show the evolution of the output spectra versus different pumping peak powers at the two selected pump wavelengths. For the experiment of 1060-nm pumping, the peak powers coupled into the fiber is up to 78 kW, while for 1040nm pumping, the coupled peak power is up to 138 kW. The difference of these two power level is due to the varied achievable gain in Yb-doped fiber amplifiers. In Fig. 3.6-3(a) and (b), significant SRS growth pumped by injected beam of 1060-nm wavelength and an effective suppression of SRS by injected beam of 1040 nm are observed. Following the same procedure as in the case of the 33μm-core CCC fiber, this difference is quantified by the integral fraction of the wavelengths longer than the signal wavelength by 35 nm (approximately 9 Thz) for both signal wavelengths in Fig.

3.6-3 (a) and (b) to the spectral power of the total measured spectra. In this experiment, due to the doubled core size which leads to around 4 times less nonlinearity, the non-phase-matched FWM amount which is included in the SRS power integration is smaller, and a more accurate theoretical fitting can be predicted. However, an additional issue which should be noticed is when pumping wavelength is at 1040 nm, large amount of the in-band ASE inevitably mixed with pulses energy is sent into the test fiber. Thus, in order to avoid ASE being counted in the integrals of the spectra power, the integrated power of the total spectra is calibrated with the measured pulse energy. Fig. 3.6-4 shows the obtained fractions of the power around the Stokes wavelength with respect to the total pulse power for both signal wavelengths and the relevant simulation result. This result shows that SRS is indeed suppressed by the tailored loss profile of this CCC fiber. Without suppression, the amount of SRS appears to grow starting from 45-kW peak power, while with suppression, the SRS amount starts to grow at 100-kW peak power. Thus, doubled SRS threshold is observed. The simulation curves is calculated from the frequency dependent coupled intensity equations of SRS [62]

$$\begin{cases} \dfrac{dI_p}{dz} = -\dfrac{\omega_p}{\omega_s} \cdot g_R(\Omega) \cdot I_p \cdot I_s \\ \dfrac{dI_s}{dz} = g_R(\Omega) \cdot I_p \cdot I_s - \alpha_s I_s \end{cases} \tag{3.6-1}$$

where g_R is the Raman gain coefficient as a function of frequency shift Ω. One can observe the fit between experimental result and simulation result, because the side bands generated from non-phase-matched FWM is distinguishably separated from the Stokes waves.

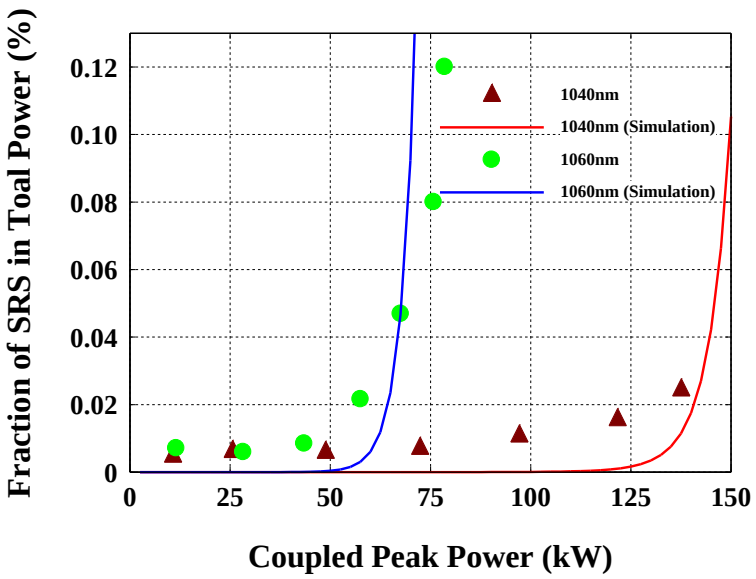

Fig. 3.6-4 The power fractions of the integrated components according to wavelength longer than 1095 nm in Fig. 3.6-3 (a) and the integrated components according to wavelengths longer than 1075nm in Fig. 3.6-3 (b) versus coupled peak power

3.7 Conclusion

We experimentally demonstrated SRS suppression due to the tailored transmission spectrum of specially-designed LMA-CCC fibers. Through selecting the pump wavelengths whose corresponding Raman gain peak is located at the phase-matched wavelength of the CCC fiber, no apparent SRS have been observed respectively for coupled peak powers of up to 30 kW in a 6-m long 33μm-core Ge-doped CCC fiber at 1087-nm signal wavelength and for coupled peak powers of up to 140 kW in a 4-m long 60-μm-core Ge-doped CCC fiber at 1040-nm signal wavelength where large Stokes-wave loss in the fiber is matching the spectral profile of Raman gain peak in this fiber. The comparison with the tests at non-suppressing signal wavelength indicates that a significant degree of SRS suppression has occurred. Potential practical significance of this finding can contribute to two aspects. One is the availability of using longer-length fibers to facilitate heat dissipation in high power fiber lasers and amplifiers without being limited by SRS threshold. The other one is the application to high power Raman-free long delivery fibers.

Chapter IV

Study of Transverse Mode Instabilities in High Power Fiber Lasers

4.1 Introduction

Increasing average power from fiber lasers or amplifiers is associated with increasing fiber core size to mitigate nonlinear effects and facilitate high power pumping. However, as it was recently discovered experimentally, increasing power to between few hundred watts and up to approximately a kW in large mode area (LMA) fibers leads to a sudden degradation of the output mode [24,29,65], which limits the achievable power in a diffraction-limited beam. This phenomenon, known as transverse mode instability (TMI) is characterized by a threshold-like onset of coupling from the fundamental mode (FM) to the higher-order modes (HOM), and by a time-dependent periodic or chaotic oscillation at the kHz frequencies between the modes at powers above the threshold [25]. The degree of chaotic behavior increases with increasing power when it is beyond TMI threshold.

By now the importance of thermally-induced refractive-index gratings caused by beating between the fundamental and a higher-order mode in producing TMI is well established [66]. Since the local heating, associated with the quantum defect between fiber pump and fiber signal wavelengths, is proportional to the local inversion, this grating follows a periodic longitudinal temperature variation resulting from spatially-varying

inversion due to the intensity variation in the intermodal beating pattern. Through thermo-optic effect this will result in a refractive index grating. Period of the beating and, hence, the grating period, is determined by the propagation-constant difference of the two modes.

As it is pointed out in [66], although such self-induced gratings always have the exact period to couple between the beating modes, an efficient power transfer between the FM and the HOM requires a phase lag between this grating and the intensity oscillation pattern of the two beating modes. In the same paper it was suggested that this phase lag could be produced by a moving refractive-index grating formed by the interference between two transversal modes with slightly different optical frequencies (typically in the kHz range). This has been confirmed theoretically by several authors using various coupled-mode equation models [66,67,68,69], which associate this mechanism with the thermally induced stimulated scattering processes. In addition, it has been also proposed that an alternative mechanism can be involved in producing this phase lag [27,28,70], in which the two interfering modes that induce TMI are at exactly the same frequency. Evidence for this was based primarily on the results of numerical simulations using integrated beam-propagation models, which demonstrated the onset of TMI with strictly monochromatic input fields. Although conceptual explanations of this mechanism have been attempted, but no theoretical model for it was ever proposed.

In this chapter we present a general time-dependent coupled-mode theory describing TMI in terms of a general two-beam coupling (TBC) process, which reveals the physical noise, spontaneous emission, can produce the phase lag between the thermally-induced grating and a two-mode interference pattern. We also show that within the framework of the derived time-dependent TBC coupled-mode model, the origin of TMI can be described based on a spatially-dependent structure. In addition, this general model can be simplified

as a static model with which the threshold of TMI can be quickly calculated. Using this static model, the scheme of mitigating TMI with CCC fibers can be assessed.

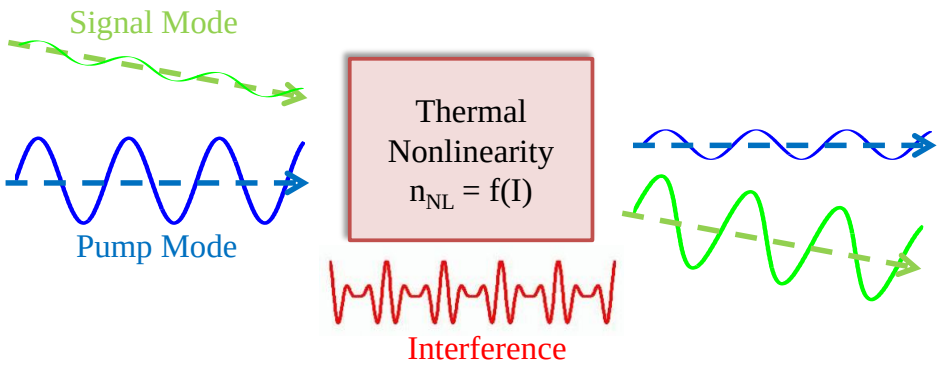

Fig. 4.1-1 Two beam coupling is a nonlinear process in which the interference pattern would be imprinted into a moving grating.

In Sec. 4.2, the physical background of TMI is summarized, and this understanding of TMI will serve as the headlight to develop the time-dependent theory. This general time-dependent model can be simplified to a static model of TMI, which we developed in parallel with both Hasen [68] and Dong [69], are used to characterize the threshold of TMI with different fiber parameters as well as to estimate the required HOM loss in CCC fibers to suppress TMI . In Sec. 4.4, the numerical implementation of the time-dependent theory is shown. In Sec. 4.5, the physical noise and issue of the non-physical noise occurring in the numerical simulation is discussed. With understanding the role of the noise in the dynamical behavior of TMI, in Sec. 4.6, the spatial phase shift induced by these noise sources reveals that the origin of TMI can be simply explained with the developed analytical model. Sec. 4.7 is the conclusion of our current study of TMI.

4.2 Physical Model of TMI in LMA-fiber Amplifiers

The general procedure of modeling TMI is constructed as the following. Two modal fields are added to produce spatially and temporally varying irradiance. Through the interaction between the optical waves and the medium, this irradiance induces a refractive index change. The exact mechanism of this nonlinear refractive index change depends on particular physical phenomena involved, but the general feature is that it is associated with a finite response time of a medium. For example, in a medium with Kerr nonlinearity, standard Debye equation applies. In the case of thermally induced TMI, the analogical mechanism is more complex in that it involves local population inversion, thermal diffusion and thermo-optical effect. The standard theoretical framework of TBC can be applied to the TMI for a time-dependent dynamic model, and the thermally-induced modal coupling can be applied for the static model, which is simplified from the former and will serve as a tool to analyze TMI thresholds in a system. In order to understand the physical mechanism, the most general dynamical model will firstly be introduced.

A general formulation of TBC can be strictly derived from the electromagnetic wave equation with the nonlinear refractive index modulated by the other control equation. The relevant control equations of the two well-known TBCs, namely SBS and SRS, are acoustic wave equation and atom oscillator equation respectively. When addressing temperature-induced refractive index modulation, the thermal diffusion equation is the control equation to formulate the thermally-induced TBC. The procedure of rigorously deriving the time-dependent TBC model for the thermally-induced TMI follows the same general theoretical framework described above, with the essential difference that the amplitudes are assumed to be both temporally and spatially varying. This makes it impossible to achieve coupled power equations, i.e. time-dependent coupled-amplitude equations become the final point

of the theoretical derivation. However, this time-dependent coupled-amplitude equations can be simplified to a pair of coupled-power equations with eliminating the time-dependence of the amplitude. This simplified model is useful for predicting the threshold of TMI and for plotting the mitigating strategy. In the following subsections, this whole modeling procedure is introduced from a classical theory of TBC.

4.2.1 Review of Two-Beam-Coupling Theory in Kerr Media

The fundamentals of TBC is introduced in the well-known textbook of nonlinear optics *Boyd* [71]. Two waves with distance-varying amplitudes *A(z)* interfere, and the electric field can be formulized as

$$E_s(z,t) = A_1(z)e^{j(k_1 z-\omega_1 t)} + A_2(z)e^{j(k_2 z-\omega_2 t)} + c.c. \tag{4.2-1}$$

where A, k and ω are respectively the amplitude, propagation constant, and the carrier frequency of the two waves. In a Kerr-medium, the intensity of the interfering waves ($I_s = |E_s|^2$) induces nonlinear index grating $n_{NL}(z,t)$, and the medium responds within finite time τ. The response that is shown with the driven nonlinear refractive index can be described by Debye relaxation equation

$$\tau \frac{dn_{NL}}{dt} + n_{NL} = n_2 I_s(z,t) \tag{4.2-2}$$

The coupled-amplitude equations (CAEs) of these two waves are obtained by substituting $n_{NL}(z,t)$ and $E_s(z,t)$ into the wave equation

$$\nabla^2 E_s(z,t) = \frac{(n_0 + n_{NL}(z,t))^2}{c^2}\frac{\partial^2 E_s(z,t)}{\partial t^2} \tag{4.2-3}$$

, and then considering slowly-varying envelope approximation, a pair of coupled amplitude equations can be derived as

$$\frac{dA_{1,2}}{dz} = \frac{2in_0 n_2 \omega}{c}\left[\left(|A_1|^2 + |A_2|^2\right)A_2 + \frac{|A_1|^2 A_2}{1 \mp i\delta\tau}\right] \tag{4.2-4}$$

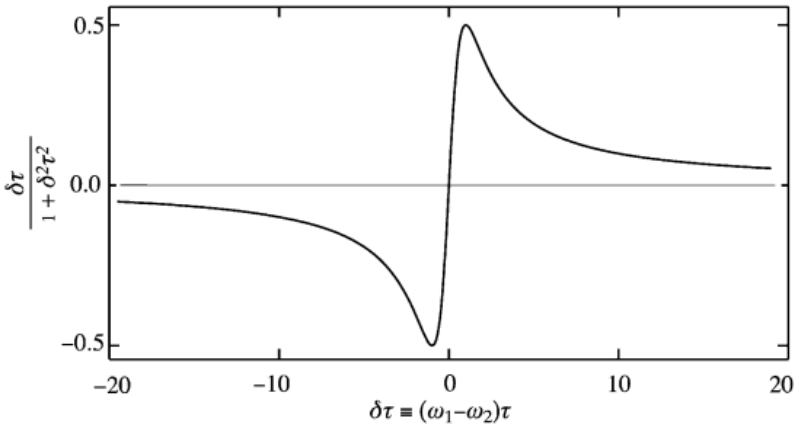

Fig. 4.2-1 Frequency dependence of the TBC gain [71]

This CAEs can be transformed to a pair of coupled-intensity equations, revealing the presence of optical gain and stimulated-scattering threshold

$$\frac{dI_{1,2}}{dz} = \mp\frac{2n_2\omega}{c}\frac{\delta\tau}{1+\delta^2\tau^2} I_1 I_2 \tag{4.2-5}$$

From Eq. (4.2-5), the wavelength-dependent conversion is plotted in Fig. 4.2-1, and the gain-peak frequency offset for the converted wave is determined by $\delta_{peak} \cdot \tau = 1$. This relationship indicates that the strongest TBC occurs when the time scale of the beating between the two waves is consistent with the delay time. Furthermore, the full-width at the half maximum (FWHM) of the peak in Fig. 4.2-1 is the phonon life time of the material.

The significance of this theory is that it depicts the fundamental physic and the modeling process of TBC with the key factors including the beating pattern of the modes, the response function with finite delay time relative to the intensity of the waves, and the conversion from one wave to the other with the frequency-offset-dependent gain. These

four factors can be translated to model TMI as introduced in the following subsections.

4.2.2 Time-dependent TMI Theory Based On Thermally-Induced TBC

By following a similar path as the last subsection, the time-dependent theory of TBC for describing TMI in high power fiber amplifiers is developed. The scalar optical field which includes two transverse modes can be written as

$$E(r,\varphi,z,t)=\sum_{2}A_i(z,t)\varepsilon_i(r,\varphi)\cdot e^{j[k_i z-\omega_0 t]}+c.c. \tag{4.2-6}$$

where ε_i indicates the normalized modal profile ($\int_0^{2\pi}\int_0^{r_b}|\varepsilon_i(r,\phi)|^2 r dr d\phi=1$), either of FM or HOM, supported in the fiber amplifier with a known step-index structure. A_i is a slowly varying amplitude in both spatial and temporal domain and k_i is the modal propagation constant. Since TMI is mainly attributes to the interaction between the fundamental LP_{01} mode, and the 1st-order LP_{11} mode, only these two modes are considered in the following derivation. The purpose to add time dependence to the amplitude is for the generality of TBC. In a TBC process, the coupling from one wave to another is derived from the phase lag between the radiation beating pattern and the imprinted refractive index grating. As the aforementioned, this phase lag is induced from the frequency offset between the involved two waves. One thing to note is that in Eq. (4.2-6), this frequency difference is included in the time-dependent amplitude, and the carrier frequency of both modes are assumed the same.

TMI is induced by the heat generated from the signal depleting population inversion with a quantum defect. If the amplification is far from being saturated, and the spontaneous emission and the re-absorption of the signal are assumed so small that they can be neglected,

the depleted population or the generated heat is linearly proportional to the signal intensity. Thus, the volume heat-generation density Q can be approximately expressed as

$$Q(r,\phi,z,t) \cong \sigma_{es} \cdot N_{Yb} \cdot n_{\mu}(z) \cdot \left(\frac{\lambda_s}{\lambda_p} - 1 \right) \cdot I_s(r,\phi,z,t) \tag{4.2-7}$$

where σ_{es}, N_{Yb}, n_{μ} are the emission cross section at the wavelength of the signal, the doping density, and the ratio of the population inversion. $\lambda_{p(s)}$ is the optical wavelength, and thus the ratio in the parentheses represents the quantum defect. I_s is the signal intensity which includes the radiation beating pattern of the FM and the HOM, and it can be given by

$$I_s(r,\phi,z,t) = \frac{1}{2} n_0 \varepsilon_0 c \cdot \left[|A_1|^2 \varepsilon_1^2 + |A_2|^2 \varepsilon_2^2 + A_1 A_2^* \varepsilon_1 \varepsilon_2 e^{jqz} + A_2 A_1^* \varepsilon_2 \varepsilon_1 e^{-jqz} \right] \tag{4.2-8}$$

where q is the difference of the propagation constants. For simplicity, Eq. (4.2-8) can be rewritten as

$$I_s = I_{11}\varepsilon_1^2 + I_{22}\varepsilon_2^2 + I_{12}\varepsilon_1\varepsilon_2 e^{jqz} + I_{21}\varepsilon_2\varepsilon_1 e^{-jqz} \tag{4.2-9}$$

where

$$I_{ij} = \frac{1}{2} n_0 \varepsilon_0 c A_i A_j^* \tag{4.2-10}$$

The volume heat-generation density Q in Eq. (4.2-7) serves as the source term in the thermal diffusion process, which is controlled by the thermal diffusion equation

$$\frac{1}{\alpha} \frac{\partial \Delta T(r,\phi,z,t)}{\partial t} = \nabla^2 \Delta T + \frac{Q}{\kappa} \tag{4.2-11}$$

where α and κ are the thermal diffusivity and the thermal conductivity respectively. Since the medium is a longitudinally-extended optical fiber, the diffusion along the z direction is neglectable. Eq. (4.2-7), integrated with Eq. (4.2-8)-(4.2-10), is substituted into Eq. (4.2-11) which can be solved by the separation of variables in the cylindrical coordinate system. Since the z dependence is not considered, Eq. (4.2-11) with only radial r and azimuth angle

ϕ dependence is solved, and the solution can be described as

$$\Delta T(r,\phi,z,t)=\frac{\alpha\gamma_2}{\eta}\cdot\sum_{\nu}\sum_{m=1}^{\infty}\frac{J_\nu(\beta_m,r)}{N(\beta_m,\phi)}\cdot\int_{t'=0}^{t}\left(B_{11}I_{11}+B_{22}I_{22}+B_{12}I_{12}e^{jqz}+c.c.\right)\cdot e^{-\alpha\beta_m^2(t-t')}dt' \tag{4.2-12}$$

and

$$B_{ij}=\int_{r'=0}^{r_{Yb}}\int_{\phi'=0}^{2\pi}r'J_\nu(\beta_m,r')\cos(\phi-\phi')\varepsilon_i\varepsilon_j dr'd\phi' \tag{4.2-13}$$

where η is the thermal-optic coefficient. J_ν is the first kind Bessel Function of order ν, r_{Yb} is the doped radius, and N is the normalization function. β_m is the eigen-value of the radial dependent differential equation which can be solved with the thermal boundary condition shown as

$$\frac{\partial\Delta T}{\partial r}+\frac{h}{\kappa}\Delta T=0 \tag{4.2-14}$$

h is the effective heat transfer coefficient. In addition, γ_2 in Eq. (4.2-12) is defined by

$$\gamma_2(z)=\frac{\eta\sigma_{es}N_{Yb}n_\mu(z)}{\kappa}\left(\frac{\lambda_s}{\lambda_p}-1\right) \tag{4.2-15}$$

Eq. (4.2-13) shows the decomposition of the heat generation profile derived from the intensity beating pattern by the eigen-mode of the diffusion equation in Eq. (4.2-11) in cylindrical coordinate. The purpose of this decomposition is to quantify the diffusion for each eigen-function of this diffusion equation, which is sourced by the heat generation. As the diffusion for each eigen-function is determined, these eigen-functions are recombined to acquire the total temperature difference. Therefore, Eq. (4.2-12) reveals the relaxation nature of a thermal diffusion process. In this equation, the integral also reveals the relaxation time of each eigen-function as

$$\tau_m = \frac{1}{\alpha \beta_m^2} \tag{4.2-16}$$

Therefore, the validity of deriving TBC to acquire a pair of coupled amplitude equation is confirmed.

The nonlinear refractive index can be defined as

$$n_{NL} = \eta \cdot \Delta T \tag{4.2-17}$$

Considering effective refractive index of the gain from the amplifier as n_g, the total relative permittivity, which attributes to the gain and the nonlinearity, can be expressed as

$$n^2 = \left(n_0 + n_g + n_{NL}\right)^2 \cong n_0^2 - j\frac{g(z)n_0}{k_0} + 2n_0 n_{NL} \tag{4.2-18}$$

since n_g and n_{NL} are much smaller than n_0. Eq. (4.2-6) and Eq. (4.2-18) can be substituted into the wave equation $\nabla^2 E - \frac{n^2}{c^2}\frac{\partial^2 E}{\partial t^2} = 0$. Since the Helmholtz equation $\nabla_t^2 \varepsilon(r,\phi) + \left(n_0^2 k_0^2 - \beta^2\right)\cdot \varepsilon(r,\phi) = 0$ is satisfied by the mode profiles, this equivalence helps eliminate the transversal dependence of the mode. Then following the principle of spatially and temporally slowly-varying envelope approximation on $A_i(z,t)$, a pair of coupled mode advection equations can be derived as

$$\frac{\partial A_1}{\partial z} + \frac{n_0^2}{c n_1}\frac{\partial A_1}{\partial t} = j\frac{n_0}{n_1}k_0\left(H_{1111} + H_{2211}\right)A_1 + j\frac{n_0}{n_1}k_0\left(H_{1221}\right)A_2 + \Gamma_1\frac{n_0}{2n_1}gA_1 \tag{4.2-19}$$

$$\frac{\partial A_2}{\partial z} + \frac{n_0^2}{c n_2}\frac{\partial A_2}{\partial t} = j\frac{n_0}{n_2}k_0\left(H_{1122} + H_{2222}\right)A_2 + j\frac{n_0}{n_2}k_0\left(H_{2112}\right)A_1 + \Gamma_2\frac{n_0}{2n_2}gA_2 \tag{4.2-20}$$

where

$$H_{ijkl} = \alpha\sum_{\upsilon}\sum_{m=1}^{\infty}\left\{\frac{\gamma_2(z)}{N(\beta_m,\varphi)}\Psi_{ijkl}(\beta_m,\upsilon)\left[\int_0^t I_{ij}(z,t)e^{-\alpha\beta_m(t-t')}dt'\right]\right\} \tag{4.2-21}$$

$$\Psi_{ijkl}(\beta_m,\nu) = \int_{r=0}^{r_b}\int_{\varphi=0}^{2\pi}\int_{r'=0}^{r_{yb}}\int_{\varphi'=0}^{2\pi} R_\nu(\beta_m,r)R_\nu(\beta_m,r')\Phi(\varphi-\varphi')\varepsilon_i'\varepsilon_j'\varepsilon_k\varepsilon_l rr'd\varphi' dr' d\varphi dr \tag{4.2-22}$$

$$\Gamma_i = \int_{r=0}^{r_{Yb}} \int_{\phi=0}^{2\pi} \varepsilon_k \varepsilon_l r dr d\phi \tag{4.2-23}$$

where n_1 and n_2 are the effective refractive indices of the FM and the HOM. g is the gain coefficient associated to the active amplifier. Eq. (4.2-19)-(4.2-23) is an analytical model which describes the dynamic (time-dependent) coupling between the modes. Eq. (4.2-19)-(4.2-20) are a pair of the coupling amplitude equations. The left-hand-sides of these equations reveal the propagation nature of the two waves. This form is the so called advection equation which describes the "flow" of the waves from one end of a fiber to the other. The right-hand-sides by order indicate the thermally-induced phase variation, the modal coupling, and the gain from amplifiers. In other words, the pair of these two advection coupling amplitude equations explains that in the propagation process, when these two waves flow from the input end to the output end, they would experience the nonlinear phase variation and the mode coupling due to the diffused thermal distribution that results from the thermal loading on the medium. These phase variation and modal coupling terms are factorized with the integrated nonlinear refractive index H_{ijkl}, which represents the thermal "holography". H_{1111}, H_{2222} refers to the nonlinear refractive indices of the self-phase modulation. H_{1122}, H_{2211} refers to the nonlinear refractive indices of the cross-phase-modulation terms. H_{1221}, H_{2112} refers to the nonlinear refractive indices of "four-wave-mixing", in which two waves are at the current moment and two other waves are at the past moment. Overall, this model is consist of the propagation of the modes, the 6 different terms of thermally-induced nonlinear refractive indices, and the amplification of the waves in the fiber.

4.2.3 Time-independent Model for TMI Threshold Calculation

In the last section, the time-dependent model of the thermally-induced TBC in high power fiber amplifiers is derived. With this model, the temporal behavior of TMI can be simulated. However, this model is not convenient for obtaining the threshold of TMI, even though this information is indeed included. In order to create a quick path to calculate the threshold of TMI, the time-dependence in this model, formulizing in Eq. (4.2-19)-(4.2-21), is removed by making the following change on Eq. (4.2-6)

$$A_i(z,t)e^{-j\omega_0 t} \Rightarrow A_i(z)e^{-j\omega_i t} \tag{4.2-24}$$

where ω_i is the carrier frequency of one mode, and we assume $\omega_1 \neq \omega_2$ for counting the frequency offset ($\Delta\omega = \omega_1 - \omega_2$) between the two modes. Thus, due to the lack of time-dependence, the coupled amplitude equations can be further derived as a pair of coupled power equations. As a result, the model of stimulated thermal two beam coupling is derived from the model of time-dependent TBC and shown with the following three formulas

$$\frac{dP_1}{dz} = -\chi_1(\Delta\omega)gP_1P_2 + \Gamma_1 gP_1 - l_1P_1 \tag{4.2-25}$$

$$\frac{dP_2}{dz} = \chi_2(\Delta\omega)gP_1P_2 + \Gamma_2 gP_2 - l_2P_2 \tag{4.2-26}$$

where l_1 and l_2 are the modal loss of FM and HOM respectively.

$$\chi_i = \frac{\eta n_0^3}{\kappa n_i}\cdot\left(\frac{\lambda_s}{\lambda_p}-1\right)\cdot\sum_{\nu}\sum_{m=1}^{\infty}\left\{\frac{\Psi_{1212}(\beta_m,\nu)}{N(\beta_m,\nu)}\left[\frac{\alpha\cdot\Delta\omega}{\alpha^2\beta_m^2+\Delta\omega^2}\right]\right\} \tag{4.2-27}$$

$\Delta\omega$ represents the amount of frequency downshift, g is the gain coefficient of the amplifier, and Γ is the modal overlap of each mode with the ion-doped area. χ is the thermal nonlinear coefficient that is determined by the wavelength of the pump and the signal, the fiber parameters such as core size and NA, and the cooling conditions.

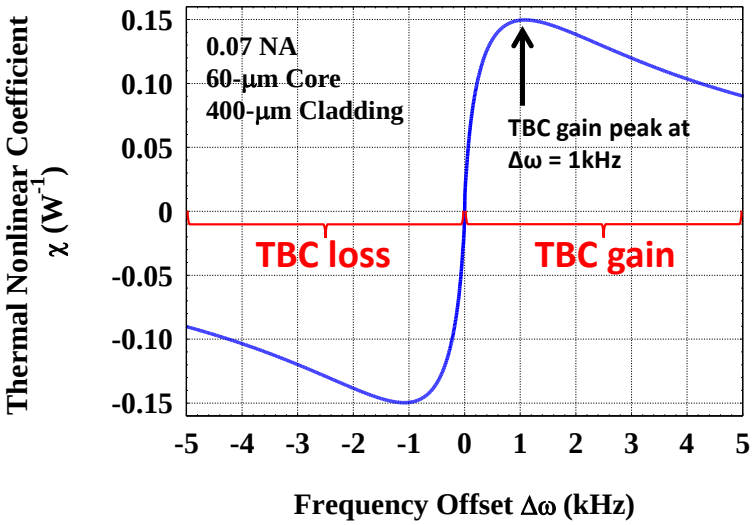

Fig. 4.2-2 Thermal nonlinear coefficient versus frequency offset

In Eq. (4.2-27), χ is expressed as a function of frequency offset between FM and HOM. This figure shows the frequency-downshift spectrum of this nonlinear coefficient for a step-index LMA fiber with 60-μm core, 400-μm cladding, and 0.07-NA. (The detailed parameters in Table 4.5-1.) Note that at the zero frequency offset this static model gives no nonlinear gain. The negative segment of the frequency-downshift ($\Delta\omega$) indicates the TBC loss on the HOM, while the positive one reveals the TBC gain on the HOM. The profile of χ shown in this figure is determined by the finite thermal response time of the field beating pattern between FM, which serves as the pump, and HOM, which serves as the signal. This is associated to the previously-mentioned phase lag between the beating patterns of the waves and the medium, predicting the frequency-downshift from the pump wave (FM) to the signal wave (HOM). In this figure, the gain peak is at 1-kHz frequency offset, which indicates the delay is around 1 ms. Moreover, the life time of the thermal phonon can also be estimated. The FWHM of the peak is around 5 kHz, so the thermal phonon life time is

close to 200 μs. Both thermal delay and thermal phonon lifetime vary with the different thermal condition, which is associated to fiber core size, cladding size, doping area and density, cooling condition, and so on.

The value of the static model is that it can be easily implemented to calculate the threshold of the TMI, and can provide a reference for the calculation result of the more sophisticated dynamical model. Coincidently, Hensen who was simultaneously working on this static theory of TMI and solved Eq. (4.2-25)-(4.2-27) to obtain the semi-analytic formula of SRS threshold which is given by [67]

$$x_{th} = \hbar\omega\sqrt{\frac{2\pi\Gamma_1}{|\chi''(\omega_0)|}}\frac{P(L)^{(\Gamma_2/\Gamma_1-1.5)}}{P_1(0)^{(\Gamma_2/\Gamma_1)}}\exp\left(\frac{\chi_0}{\Gamma_1}P(L)\right) \tag{4.2-28}$$

where χ_0 and ω_0 are the maximum value of the thermal nonlinear coefficient χ and the corresponding frequency, χ'' is the second derivative of χ, and *P(z)* is the total output power. In this formula, x_{th} indicates the output power ratio of HOM to FM at which the TMI threshold is reached, and it is generally set 5%. Eq. (4.2-28) is solved by a numerical root-finding method to calculate the TMI threshold which is characterized by the output average power of a fiber amplifier. According to the relevant parameters in Eq. (4.2-28), TMI threshold is associated to the wavelength of pump and signal waves, filling ratio of the doped area ($r_{Yb} \le r_{core}$), core size, NA, and cooling condition.

One important note is that the TMI threshold calculated by Eq. (4.2-28) is not sensitive to the cooling condition, even if the cooling factor is included in the theory and the macroscopic temperature of the fiber amplifier is indeed varied in different cooling environment. This fact is definitely not consistent with the observation in the experiment in ref. [29]. The reason of this inconsistency is attributed to the idealized modeling in which only symmetric cooling is considered [72]. The temperature gradient induced in an

asymmetrically cooled fiber can distort the modal profile as well as the thermally-induced grating, and thus the TMI threshold is more dependent on the cooling condition. In addition, the thermal-relevant parameters including thermal conductivity, thermal diffusivity, density, heat capacity, and thermal-optic coefficient in Eq. (4.2-28) are all assumed temperature independent. These assumptions are definitely not realistic, since the temperature of the fiber is highly dependent on the cooling condition. The solution of this issue needs more investigation, and currently only a numerically intense beam-propagation model integrated with a 3-dimensional thermal diffusion formula can includes the above mentioned dependences, but this part is not in our scope here.

4.3 Role of HOM Suppression in Increasing TMI Threshold

In this section, the static model is used to characterize the TMI threshold in step-index fibers with different NA and doped ratio to explain the difficulty of engineering the modal overlap with doped area for increasing TMI threshold. Then three types of mitigation strategies of TMI mitigation, which represent the current approaches to increase the TMI threshold, will be introduced. Following these approaches, we propose to use the effective-single mode performance of CCC fibers to achieve the mitigation of TMI in high power fiber amplifiers.

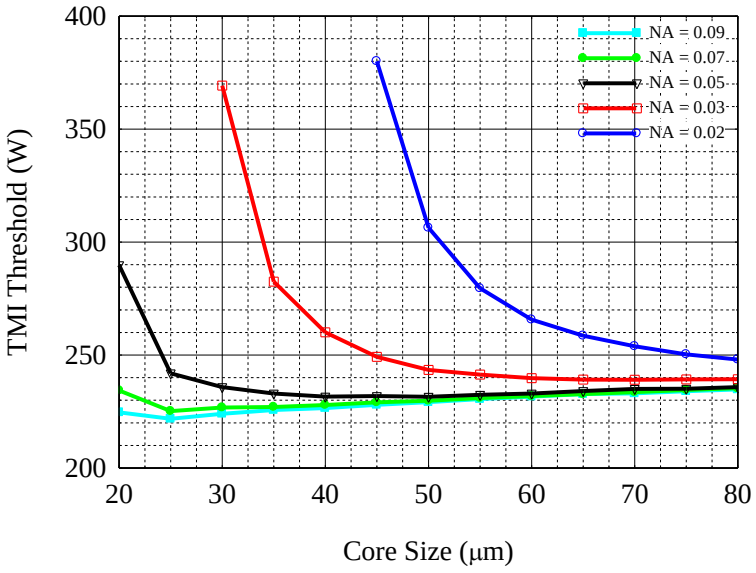

Fig. 4.3-1 TMI threshold of 400-μm step-index Yb-doped fiber amplifiers operated at 1μm wavelength with different core size and numerical aperature

By using Eq. (4.2-28), TMI threshold can be characterized with the different fiber parameters such as the core size, NA, and the dopant filling ratio. This characterization result can serve as the first step of determining a scheme for TMI suppression.

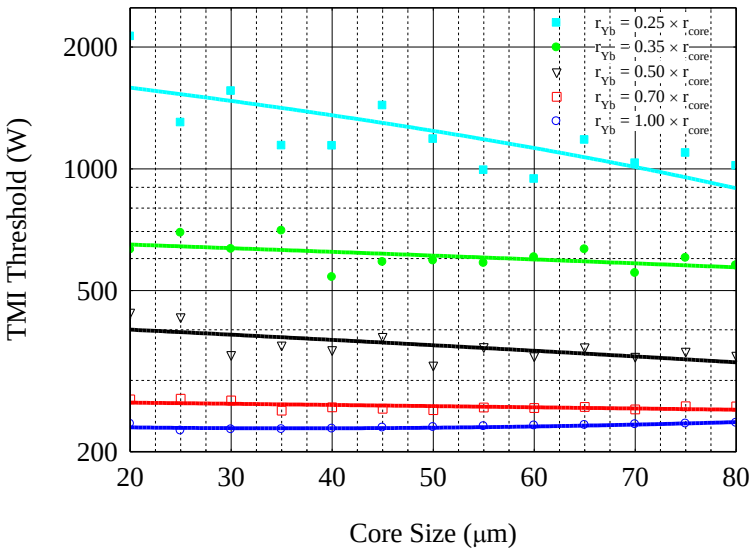

Fig. 4.3-2 TMI threshold of 400-μm Yb-doped fiber amplifiers with 0.07 NA operated at 1μm wavelength with different core size and filling ratio of the doped region

Fig. 4.3-1 shows the TMI threshold calculated by Eq. (4.2-28) with varied core size and numerical aperture in a 400-μm Yb-doped step-index fiber that is operated at 1μm wavelength. In this calculation, only two modes, the fundamental LP_{01} mode and the 1st-order LP_{11} mode, are involved. This result reveals two facts: 1) small NA means the reduction of the modal beating pattern that is overlapped with the doped region thus reducing the strength of the thermal nonlinearity and increasing the TMI threshold; 2) TMI cannot occur in a single-mode fiber. According to Fig. 4.3-1, the TMI threshold can only be pushed by 1.5 times when the NA is changed from 0.09 to 0.02 at relatively smaller core fibers (<50 μm). However, if the V-number ($\frac{2\pi}{\lambda} \cdot r_{core} \cdot NA$) of the fiber amplifier is smaller 2.405, TMI cannot occur and the threshold is infinite. For larger-core fibers, a smaller NA is needed to achieve single-mode operation, but concerning the stability of the amplifiers, NA cannot be unlimitedly reduced with the need to scale up the core size. As long as the fiber can support more than one mode, the issue of TMI cannot be avoided.

Fig. 4.3-2 shows the TMI threshold calculated by Eq. (4.2-28) with varied core size and filling ratio of the doped region in a 400-μm Yb-doped step-index fiber with 0.07 NA and is operated at 1μm wavelength. From the analysis shown in Fig. 4.3-1, we know that the reduction of NA leads to a small overlap of the modal beating pattern with the doped region thus increasing the TMI threshold. Therefore, a more straightforward scheme to increase TMI threshold is to reduce the filling ratio of the doped region in the core. In Fig. 4.3-2, the five-fold of TMI threshold increase is observed when the ratio of the doped radius to the core radius decreases from 1 to 0.25. However, the price to pay is that longer active fibers should be applied to the amplifier in order to maintain the rate of pump absorption and signal amplification. For the case with the ratio equivalent to 0.25, a 16-times-longer active fiber should be used. This indicates a 16-times-smaller SRS or SBS threshold, leading to a serious trade-off. On the other hand, one thing which should be clarified is that reducing the doping density is different from this scheme, even if the side effect of both schemes are the need of increasing the fiber length. Basically, reducing the doping density cannot change the TMI threshold too much even if the local temperature of the fiber is indeed reduced, since the formation of the temperature grating is not influenced and the fiber length is also not relevant to the TMI threshold.

In the above two cases of TMI threshold characterization, we can understand that modifying the fiber parameters for the purpose of TMI suppression can either only have a limited improvement (by reducing NA) or leads to a trade-off (by reducing r_{Yb}) associated to the other nonlinearities. Thus, an alternative method to efficiently mitigate TMI without leading to any extended issues is pursued by many researchers. In these two years, since the mechanism of TMI in high power fiber amplifiers is more understood, three mitigation

strategies are proposed and two of them are also experimental demonstrated. These three strategies are categorized as active extrinsic mitigation, passive extrinsic TMI mitigation, and passive intrinsic TMI mitigation respectively [73]. The active extrinsic mitigation, which indicates a scheme associated to an externally modulated seeding signal, is demonstrated by exploiting acousto-optic modulation to alternatively seed phase-shifted HOM into a fiber amplifier [30]. The purpose of this implementation is to wash out the thermal grating, and this operation has resulted in the increase of the TMI threshold by 3 times. The passive extrinsic mitigation is mainly attributed to the reduction of quantum efficiency by making the wavelength difference between pump and signal smaller. This scheme is broadly used in tandem pumped fiber lasers, but the successful demonstration of TMI mitigation is still absent. The focus of the passive intrinsic strategy is on modifying the fiber structure to reduce the local heat load, which is relevant to the TMI threshold. Our calculation shown in Fig. 4.3-1 and Fig. 4.3-2 is a reference to approach this mitigation scheme. Experimentally, this scheme has been demonstrated in four different types of fiber lasers. In 2013, Jauregui etc. experimentally verified that a smaller core-to-cladding ratio leads to a higher TMI threshold when the total pump absorption was kept constant [73]. In 2014, Robin etc. demonstrated modal instability-suppressing PCF amplifier with 811 W output power [32]. The doping area of this PCF was designed to favor the amplification of fundamental mode instead of HOM. Later on, Otto etc. used a four-core PCF to directly increase the TMI threshold by 4 times [74]. Even though these methods are effective of suppressing TMI, the improvement is still quite limited. Thus, here we proposed an alternative passive intrinsic strategy.

The onset of TMI is attributed to the multi-mode operation in a high power fiber amplifiers. Thus, in order to suppress the stimulated coupling from FM to HOMs (mainly

LP_{11} mode), the most straightforward method is to increase the attenuation of HOMs. This attenuation determines the degree of TMI suppression. Since the achievable HOM loss in a specialty fiber cannot be infinite, knowing the level of the TBC gain on the HOM is an important reference for the design work of specialty CCC fibers. The following gives an example of the calculated TMI threshold of a 30-μm-core double-clad Yb-doped fiber amplifier with HOM suppression. This calculation is executed with the modified form of Eq. (4.2-28) that is given by

$$x_{th}e^{\alpha L} = \hbar\omega\sqrt{\frac{2\pi\Gamma_1}{|\chi''(\omega_0)|}}\frac{P(L)^{(\Gamma_2/\Gamma_1-1.5)}}{P_1(0)^{(\Gamma_2/\Gamma_1)}}\exp\left(\frac{\chi_0}{\Gamma_1}P(L)\right) \tag{4.3-1}$$

where α is the loss coefficient of the HOM, and L is the fiber length. The relevant parameters are listed in Table 4.3-1. The calculated TMI threshold at different level of HOM attenuation using Eq. (4.3-1) is shown in Fig. 4.3-3. The result in this figure indicates two points: 1) the TMI suppression is more prominent in longer fibers, and this is only due to the overall HOM attenuation is larger. Basically, the increment of the TMI threshold versus total loss can be quantified as 1.6 W/dB; 2) for a 2.5-m fiber amplifier, a 100-dB/m HOM loss can lead to approximately tripled TMI threshold, and a 200-dB/m HOM loss can guarantee the 1-W input signal being amplified by 30 dB without reaching TMI threshold. Thus, the HOM attenuation in a fiber amplifier is expected to strongly mitigate TMI.

Table 4.3-1 Parameters of TMI threshold of a 30-μm-core DC Yb-doped fiber amplifier with HOM suppression

PARAMETER	VALUE
Fiber Size	400μm
Core Size	30μm
NA	0.07
Pump Wavelength	0.976μm
Signal Wavelength	1.064μm
Modal Content	LP_{01} & LP_{11}
FM Seed Power	1W
Thermal B.C.	H = 150W/m2K

In addition, an important factor to mention is that the fiber length is associated to the pump absorption. Thus, in this calculation, the pump cladding size is automatically chosen to be inversely proportional to the square root of the fiber length to keep the total pump absorption constant thus ensuring the comparison shown in Fig. 4.3-3 is meaningful.

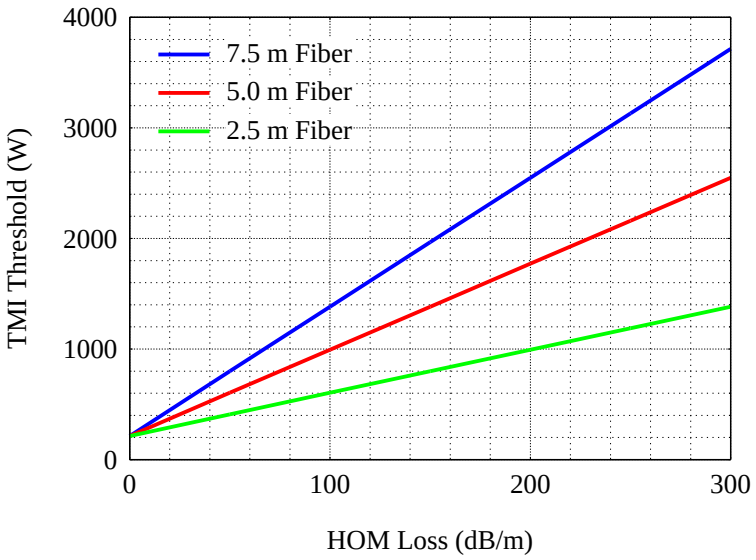

Fig. 4.3-3 TMI threshold of 30-μm core double-clad Yb-doped fiber amplifier varied with different HOM suppression, and three different lengths of such fiber amplfier are compared.

4.4 Numerical Model for Simulating TMI Phenomenon

The TMI threshold can be quickly calculated with either the full model described in Eq. (4.2-25) to Eq. (4.2-27) or the semi-analytic formula Eq. (4.2-28). Since TMI is a dynamical phenomenon, the static model cannot be used to analyze the temporal behavior. In order to understand the physics of TMI, the dynamical model, Eq. (4.2-19) to Eq. (4.2-23), needs to be solved. However, the implementation of the TMI calculation with Eq. (4.2-19) to Eq. (4.2-23) is numerically intense due to the mixture of two different time scales, i.e. the thermal diffusion is at millisecond level, while the optical transmission is at nanosecond level. Therefore, two simplifying methods are required to incorporate with the time-dependent model of modal instability. Firstly, in order to simplify the advection equations, the method of characteristics which is associated to the transformation of the laboratory coordinate to a moving coordinate is exploited. In this method, the new coordinate can be defined by the following three variables

$$\tau \equiv t \tag{4.4-1}$$

$$\xi \equiv z + \frac{n_1 c}{n_0^2} t \tag{4.4-2}$$

$$\zeta \equiv z + \frac{n_2 c}{n_0^2} t \tag{4.4-3}$$

This coordinate transformation makes the pair of coupled partial differential equations (PDEs) in Eq. (4.2-19) and Eq. (4.2-20) simplified to a pair of coupled ordinary differential equations (ODEs). In addition, since the value of n_1 is very close to n_2, a further approximation $\xi = \zeta$ is assumed. Thus, Eq. (4.2-19)- (4.2-20) become

$$\frac{dA_1}{d\xi} = jk_0\left(H_{1111} + H_{2211}\right)A_1 + jk_0\left(H_{1221}\right)A_2 + \Gamma_1 \frac{g}{2} A_1 \tag{4.4-4}$$

$$\frac{dA_2}{d\xi} = jk_0\left(H_{1122} + H_{2222}\right)A_2 + jk_0\left(H_{2112}\right)A_1 + \Gamma_2 \frac{g}{2} A_2 \tag{4.4-5}$$

Secondly, the method of phase reduction is used to reduce the truncation error in numerical calculation. Since it is found that the self-phase modulation and cross phase modulation term in Eq. (4.4-4) to (4.4-5) are purely imaginary, and this fact indicates they are both from the "macroscopic" temperature change of the material. The magnitude of these terms are usually much larger than it of the modal coupling term and can make the simulated modes rapidly accumulate phase variation thus causing serious truncation errors. In addition, because only the relative phase variation between the FM and the HOM matters to the coupling of the modes, for the sake of reducing phase accumulation, Eq. (4.4-4) and (4.4-5) can be rewritten as

$$\frac{dA_1}{d\xi} = j\frac{k_0}{2}\left[\left(H_{1111}+H_{2211}\right)-\left(H_{1122}+H_{2222}\right)\right]A_1 + jk_0\left(H_{1221}\right)A_2 + \Gamma_1\frac{g}{2}A_1 \tag{4.4-6}$$

$$\frac{dA_2}{d\xi} = j\frac{k_0}{2}\left[\left(H_{1122}+H_{2222}\right)-\left(H_{1111}+H_{2211}\right)\right]A_2 + jk_0\left(H_{2112}\right)A_1 + \Gamma_2\frac{g}{2}A_2 \tag{4.4-7}$$

These two equations are the final forms of the coupled amplitude equations which are used to implement modal instability calculation.

On the other hand, for the convenience of numerical calculation with finite difference method, Eq. (4.2-21) can be decomposed into the following equations

$$H_{ijkl} = \sum_{\nu}\sum_{m=1}^{\infty} h_{ijkl} \tag{4.4-8}$$

$$\frac{dh_{ijkl}}{d\tau} = \sum_{\nu}\sum_{m=1}^{\infty}\left[M_{m\nu,ijkl}I_{ij}\left(\xi,\tau\right)-\alpha\beta_m^2 h_{ijkl}\right] \tag{4.4-9}$$

$$h_{ijkl} = M_{m\nu,ijkl}\int_0^{\tau} I_{ij}\left(\xi,\tau'\right)e^{-\alpha\beta_m^2\left(\tau-\tau'\right)}d\tau' \tag{4.4-10}$$

$$M_{m\nu,ijkl} = \frac{\alpha n_2\left(\xi\right)}{N(\beta_m,\phi)}\left[\int_{r=0}^{r_b}\int_{\phi=0}^{2\pi}\int_{r'=0}^{r_{Yb}}\int_{\phi'=0}^{2\pi} R_\nu\left(\beta_m,r\right)R_\nu\left(\beta_m,r'\right)\Phi\left(\phi-\phi'\right)\varepsilon_i'\varepsilon_j'\varepsilon_k\varepsilon_l rr'\,d\phi'\,dr'\,d\phi dr\right] \tag{4.4-11}$$

These four formulas forms an additional set of ODE which is used to calculate the temporal-varying thermal induced nonlinear refractive indices H_{ijkl}. Overall, Eq. (4.4-6) to Eq. (4.4-11) is the dynamical model of thermally induced TBC in the transformed coordinate τ, ξ and ζ with the format of ODEs.

Moreover, in order to solve Eq. (4.4-6) to (4.4-7), a boundary condition and an initial condition are required. The initial condition is assigned as the condition of an un-pumped active fiber. This assignment indicates H_{ijkl} is zeros in the very beginning of the simulation. As for the boundary condition, the time-dependent amplitude defined in Eq. (4.2-6) indicates that the amplitude of the input signals $A_i(0,t)$ can include any types of frequency components with being modulated in time.

In the next sections, the TMI simulation in time domain with spontaneous emission as the noise source is analyzed. The HOM is supplied with downshifted frequency component to onset TMI-modal oscillation. Moreover, a non-physical noise in the relevant simulation will also be discussed. In the section after, the physics of TMI is discussed based on these simulation result.

4.5 Role of Noise in Initiating TMI

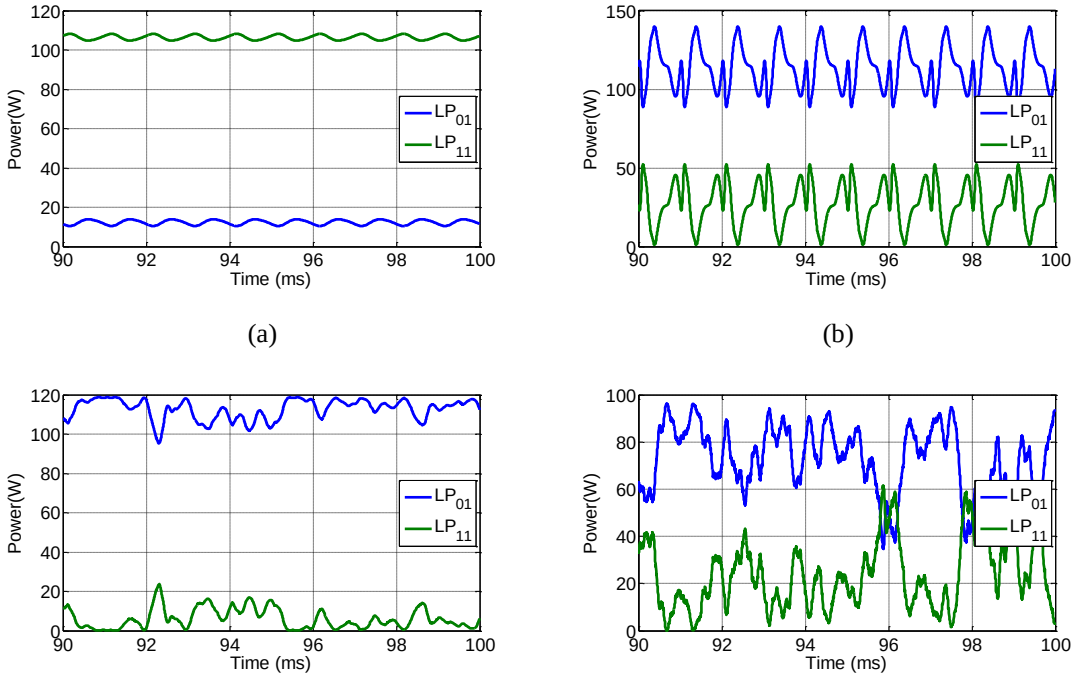

Fig. 4.5-1 The modulation of HOM seeding directly reflects on the output modal coupling. (a) Sinusiodal intensity modulation (b) Sinusoidal phase modulation (c) Random intensity modulation (d) Random phase modulation

The above developed model is time-dependent, but it doesn't include dispersion, and the modes in it are co-propagating along the fibers. Thus, the thermally-induced instability is dissimilar to modulation instability in anomalous dispersion or interference instability induced by counter-propagating beams [75,76,77]. Therefore, we audaciously predict that TMI can originate in noise. One reason is that the modulation of the FM- or HOM- seeding directly reflects on the output modal coupling. For example, if the amplitude or the phase of the seeding is sinusoidally modulated, the output modal coupling by time also fluctuate sinusoidally. The upper two figures (a) and (b) in Fig. 4.5-1 show the calculation result

with the sinusoidal modulation on the intensity and on the phase of the HOM seeding, while the lower two figures (c) and (d) show the calculation result with the random-walk modulation on the intensity and on the phase of the HOM seeding. These four types of modulation on the HOM seeding lead to the relevant fluctuation of the output modal content. In other words, the type of temporal modulation on the seeding modes determines the fluctuation of the output modes. Thus, the chaotic oscillation between the modes when the TMI threshold is reached can originates from a type of random-walk modulation on the FM, HOMs, or both.

Moreover, the spectrum of the thermal nonlinear coefficient, shown in Fig. 4.2-2 implies an important information. The blue-shifted frequency components in one mode would be coupled to the red-shifted frequency of the other mode. The chaotic oscillating noise provides the required frequency components, including both blue-shifted and red-shifted frequency components, for both FM and HOM. This explains the bidirectional coupling when the TMI threshold is reached. The detail of this principle would be further demonstrated in the frequency-domain analysis of the output signals. Before then up, in order to have a preliminary understanding of the required noise level for TMI to emerge, we can use the thermal nonlinear coefficient shown in Fig. 4.2-2 and the coupled power equation of the HOM in Eq. (4.2-26) to estimate the gain of the thermally-induced TMI. If the modal loss is neglected, Eq. (4.2-26) can be further defined as

$$\frac{dP_2}{dz} \equiv g_{NL}(z)P_2 + g_{Amp}(z)P_2 \tag{4.5-1}$$

where $g_{NL} = \chi_2(\Delta\omega)gP_1$ is the gain coefficient of the thermal nonlinearity, while $g_{Amp} = \Gamma_2 g$ is the gain coefficient from the fiber amplifier. The entire amplification of the HOM with the frequency at the gain peak can be calculated by the integral of the gain

coefficient $G_{NL}(z)=\int_0^z g_{NL}(z')dz'$, which is presented in dB-scale and shown in Fig. 4.5-2. The used parameters is listed in Table 4.5-1.

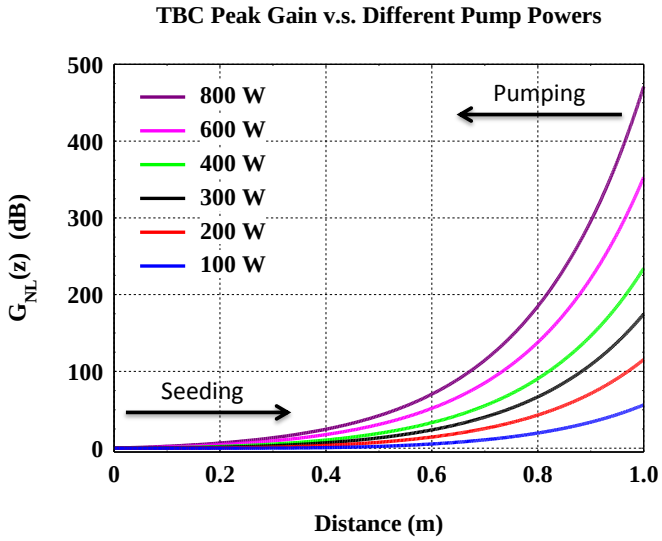

Fig. 4.5-2 Power gain of thermally-induced two beam coupling in a 1-m fiber amplifier at different pump levels

This figure shows the thermal nonlinearity supplies a larger gain (>100 dB/m for >200W pumping power) on the HOM than the amplifier (<25 dB/m) does. Even though this nonlinear gain varies for different fiber structure or cooling condition, the order of it is measured in hundreds of dB. With this level of thermally-induced gain on the HOM, as long as the power level of the in-mode noise is larger than 10^{-10} W, this noise can be amplified to the power level of watt and be prominent enough to be observed.

The most relevant noise in a fiber amplifier is the spontaneous emission (SE) which is resulting from quantum noise. This noise source is integrated into our dynamical model for the understanding of TMI in high power fiber amplifiers. Moreover, we also found an unphysical noise derived from the limited number of digits which can be used in a

numerical computation. As knowing this type of noise, we highly doubted that the observation of the simulated TMI with only considering single frequency for both FM and HOM in few published literatures misinterpret this noise source as physical [28,29]. However, even if this type of noise created a mirage of TMI in the simulation, it reflected the same physical phenomenon: TMI originates from the nonlinear amplification of noise. The detailed amplification mechanism is explained in the next section.

Table 4.5-1 Parameters used to simulate TMI in a 1-m high power Fiber Amplifier

FIBER PARAMETER	VALUE (UNIT)
Fiber Type	YbD SI Fiber
Pump Configuration	Counter-Pumping
Fiber Size	400 μm
Core Size	60 μm
Inner Cladding Size	170 μm
Doped Size	60 μm
NA	0.07
Fiber Length	1 m
Doping Density	3.5×10^{25} m^{-3}

AMPLIFIER PARAMETER	VALUE (UNIT)
Pump Wavelength	0.976 μm
Signal Wavelength	1.064 μm
LP_{01} Seeding	10W
LP_{11} Seeding	$<10^{-3}$W

THERMAL PARAMETER	VALUE (UNIT)
Thermo-Opto Coeff.	1×10^{-5} K^{-1}
Thermal Conductivity	1.38 W/(m·K)
Thermal Diffusivity	8.92×10^{-7} m^2/sec
Heat Transfer Coeff.	500 W/(m^2·K)

4.5.1 Role of the Spontaneous Emission

In an active fiber providing a large gain, the optical waves from SE can be amplified to a high power level. These amplified optical waves are viewed as noises because of its randomness of polarization, modal content, and low temporal coherence. These properties make SE an ideal candidate for seeding FM or HOM with shifted frequency thus giving rise to the random coupling between them via thermally-induced TBC. Since the FM at the

input end of the fiber amplifier is assumed dominant, we only consider the SE which is incorporated into HOM.

The SE power is calculated with the rate equation [78], and this increment of the power from SE is added into HOM with its phase being modulated by a random walk. Thus, the change of the HOM amplitude due to the incorporated SE is given by

$$\Delta A_2(z,t) = A_{SE}(z,t)e^{j\Xi(t)} \tag{4.5-2}$$

where $\Xi(t)$ is the phase modulation of a temporal random walk. An important note is that the frequency bandwidth of $A_{SE}(z,t)$ is equal to the simulation window $\delta\nu = \frac{1}{\Delta t}$, where Δt is the meshed grid size in time domain. Using the parameters listed in Table 4.5-1, simulation results calculated from the time-dependent CAE model, Eq. (4.4-6) to Eq. (4.4-7), are shown in Fig. 4.5-3. In these calculations, fiber amplifier pump is suddenly turned-on at the time t = 0. In Fig. 4.5-3, the left-hand panes show FM and HOM powers at the output of an LMA fiber amplifier over the time period of the first 250 ms after the pump power turn-on. The right-hand panes show frequency-domain pictures calculated by taking a Fourier-transform of the time-domain result from 50ms to 250 ms in the corresponding left-hand figures. In Fig. 4.5-3 (a) and (d), the modal power variation over the first 10 ms is associated with the transient thermal conditions in a fiber amplifier, and after this period, the thermal equilibrium is reached. This reveals the TMI threshold (230 W signal power) is not reached, the FM is stably produced at the output end of the fiber amplifier. Note that in the frequency domain, a spectral broadening feature is observed in the HOM spectrum in Fig. 4.5-3 (d). This spectral broadening is associated with a temporal modulation, which is from the SE noise, imposed on the HOM beam. However, since the output HOM is negligible, an oscillation between the modes cannot be observed. Fig. 4.5-3

(b) and (e) shows the result at the TMI threshold. Resembling to the condition below threshold, both the FM and the HOM show chaotic amplitude fluctuation in the first 10 ms. After this period, a tiny fluctuation between the modes continues. In Fig. 4.5-3 (e), the spectrum indicates a spectral broadening also occurs in FM. Fig. 4.5-3 (c) and (f) shows the result above the TMI threshold. Rapid and chaotic power fluctuations are observed for both modes, and the spectra of both modes are prominently broadened. In Fig. 4.5-3 (d), (e), (f), the spectrum of the normalized thermal nonlinear coefficient is attached for the comparison of the coupling-induced broadening. The spectral broadening of the FM is due to the forth-and-back coupling to HOM, since FM is assumed not incorporated with spontaneous emission and it does not possess the red-shifted frequency components, while the broadening of the HOM is because part of the HOM is from the incorporation of the SE, the frequency components around the gain peak (1 kHz) is amplified via the process of the thermally-induced TBC. Moreover, if the pumping power keeps increasing, both FM and HOM spectra will be strongly broadened and peaked around 1-kHz downshift due to the entirely chaotic oscillation between these two modes.

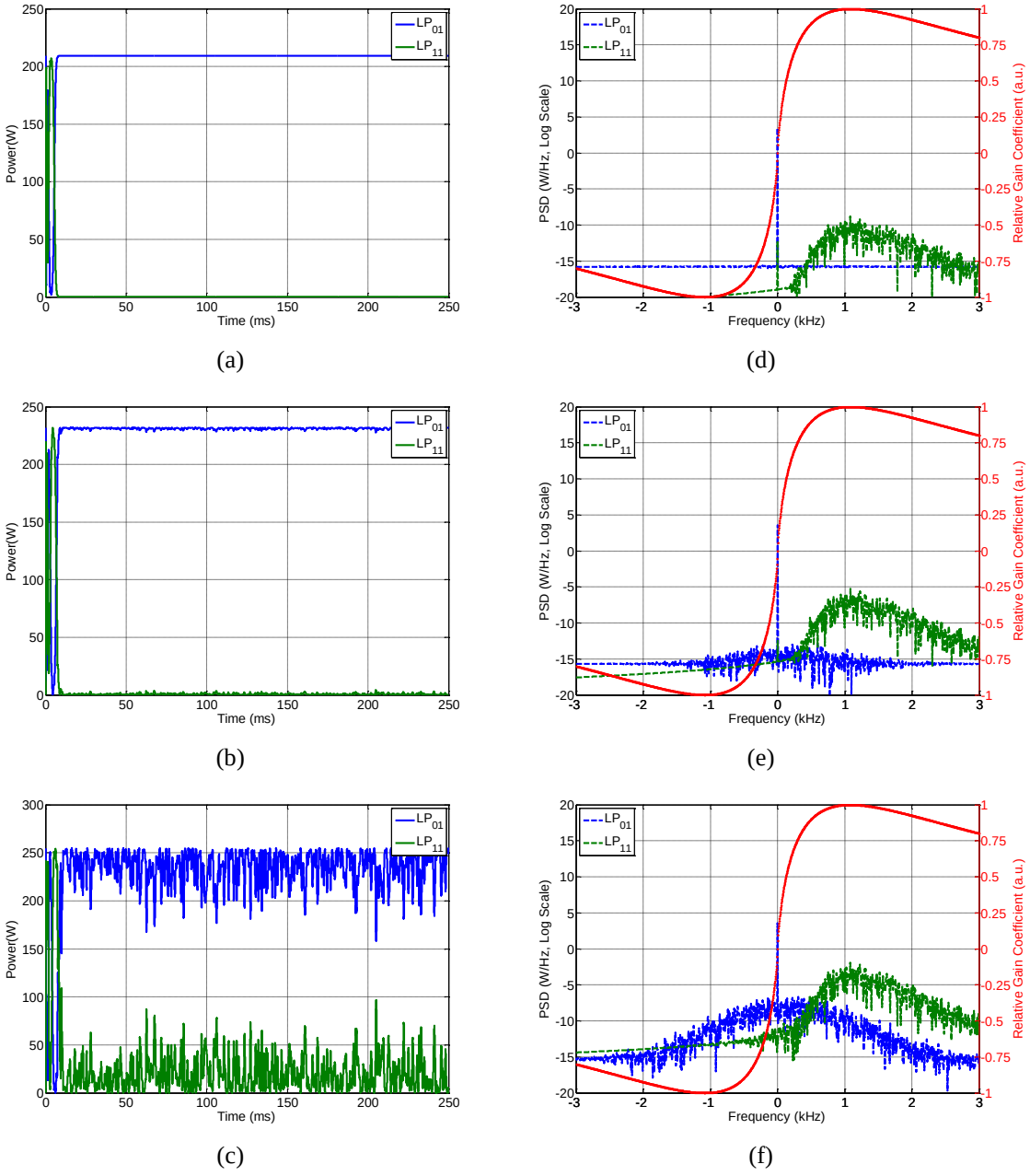

Fig. 4.5-3 (a), (b) and (c) are the output power progression of FM and HOM with the total output power at 210-W, 230-W, and 250-W; (d), (e), and (f) are the output power spectral density at the corresponding three pumping levels. The red curve is the normalized thermal nonlinear coefficient which characterizes the gain or loss in frequency domain.

The other aspect of demonstrating the TMI with HOM incorporated with SE is the transition from the spontaneous-scattering process to the stimulated-scattering process that

is occurring in the fiber amplifier. In Fig. 4.5-4, the Fourier-transform of the time-domain oscillation at 5 different locations of the fiber amplifier above TMI threshold is recorded. In the fiber segment from the seeding end (z = 0 m) to z = 0.55 m, the spectra of the HOM signal is evenly distributed. This indicates the spontaneous scattering of the HOM. At z = 0.66 m, the frequency components around the gain peak are selected and starts to be amplified, and from this point to the end of the fiber (z = 1 m), this amplification becomes more prominent, and eventually, the frequency components around the gain peak dominate. This is associated to the stimulated scattering. Consequently, the simulation results shown in Fig. 4.5-3 and Fig. 4.5-4 demonstrate that noisy modal content of the HOM can lead to thermal stimulated scattering, producing chaotic oscillations between the spatial modes.

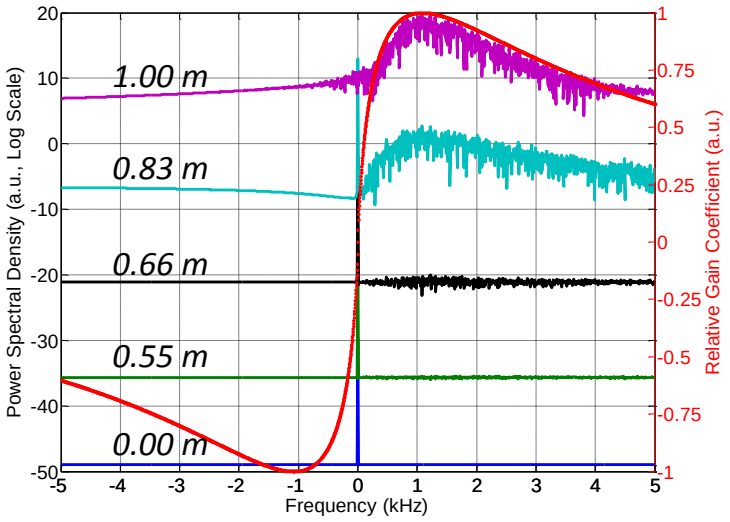

Fig. 4.5-4 Amplified frequency components at different location of the fiber. The location marked with 0.00 m is the seeding end, and it with 1.00 m is the pumping end. The red curve is the normalized thermal nonlinear coefficient which characterizes the gain or loss in frequency domain.

4.5.2 Role of the Numerical Noise on TMI Simulations

The reason to consider spontaneous emission as the noise source of TMI is explained. According to the last subsection, the spontaneous emission with a phase modulation of random-walk is incorporated into the HOM, and this phase-modulated HOM induces the stimulated TMI. However, as observed in the simulation, even if the phase modulation term is eliminated, a chaotic oscillation between the FM and the HOM would still occurs once the threshold is reached. Fig. 4.5-5 shows a similar result as the case in which the increment portion of the HOM is phase-modulated. A frequency shifted HOM is amplified when propagating through the fiber, and this shift indicates the gain provided by thermal nonlinearity. However, the main difference between these two cases is the threshold of the latter is much higher. Other than this point, the other features are all the same as the simulation result shown in Fig. 4.5-3. Now that the phase modulation term is eliminated, both FM and HOM possesses no required frequency to couple or to be coupled (χ equals zero). These clues indicate an important fact: a smaller noise source or modulating source still exists in the calculation.

This noise is eventually found from the round-off error or the truncation error which is due to the finite precision representation of real numbers in numerical calculation. For double precision with chopping, only 16 decimal digits is usable [79]. Thus, the round-off error is usually at the level of 10^{-16}.

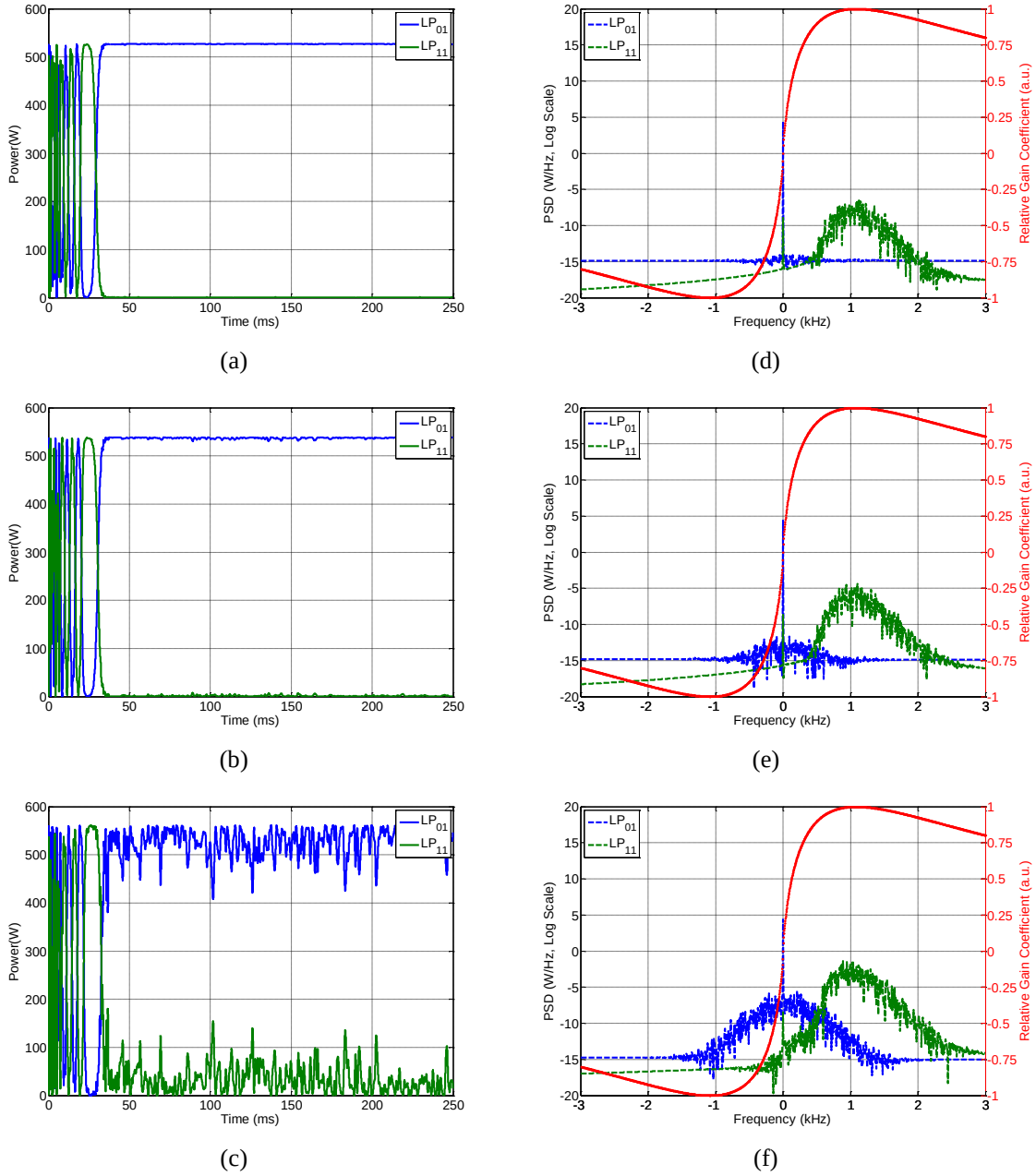

Fig. 4.5-5 (a), (b) and (c) are the output power progression of FM and HOM with the total output power at 520-W, 540-W, and 560-W; (d), (e), and (f) are the output power spectral density at the corresponding three pumping levels. The red curve is the normalized thermal nonlinear coefficient which characterizes the gain or loss in frequency domain.

The scenario of the numerical noise is mainly attributed to the calculation of the thermal equilibrium. In order to calculate the nonlinear refractive indices shown in Eq.

(4.2-21), the conversion from the integral equation to a differential equation (introduced in Sec. 4.4) is used. In principle, when thermal equilibrium is reached, Eq. (4.4-9) is equal to zero. However, due to the finite precision that can be reached, Eq. (4.4-9) can never be zero since the absolute values of the two terms at the right hand side are always slightly different. This error fluctuates and modulates the nonlinear refractive indices H_{ijkl}, and these nonlinear refractive indices further modulates the signal. As a result, the signal of FM or HOM gains additional frequencies thus enabling the coupling to happen.

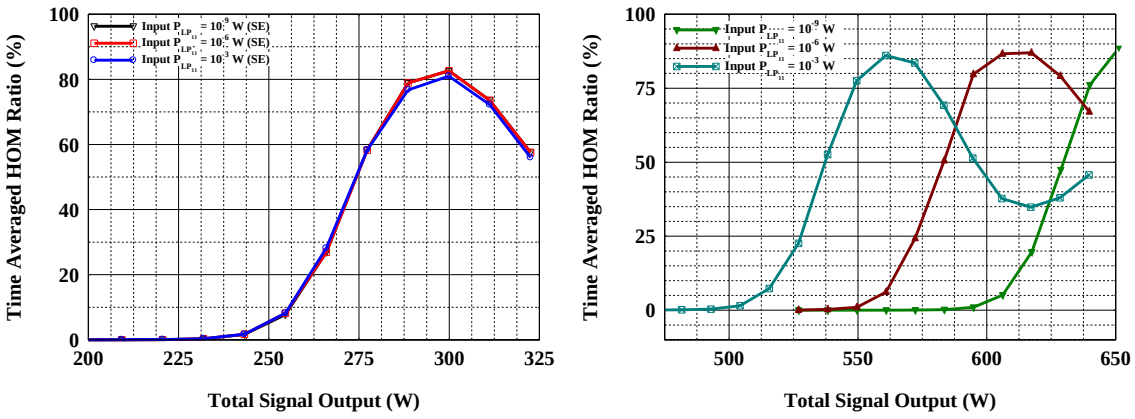

(a) (b)

Fig. 4.5-6 The time-averaged HOM ratio at different output power of signal. Three power levels of HOM excitation are considered. (a) The noise source is from spontaneous emission. (b) The noise source is from numerical round-off error.

One method to distinguish this non-physical noise induced TMI from the physical noise induced TMI is by setting different input excitation of the HOM which has the same frequency as the FM. In Fig. 4.5-6, the time-averaged HOM ratio at different output power of signal is recorded. Fig. 4.5-6 (a) is the case in which the spontaneous emission serves as the noise source. Even if the power level of HOM excitation varies, the threshold and the HOM amount is kept the same. This is mainly because the thermal nonlinearity can only

amplify frequency-shifted HOM that is originated from the spontaneous emission. However, Fig. 4.5-6 (b) shows that the time-averaged HOM and the threshold of TMI is dependent on the input power level of HOM excitation. This result indicates the instability is from a non-physical noise, because the level of this noise depends on the process of reaching thermal equilibrium, and the thermal equilibrium is associated to the depleted population by the input signal. Consequently, the role of numerical noise can be confirmed.

4.6 Discussion of the Origin of Modal Content Fluctuation in TMI

In the last section, two types of noise, one is physical and the other one is non-physical, are introduced. The physical one, spontaneous emission, serves as the most probable noise source which leads to the TMI in high power fiber amplifiers. However, a more fundamental mechanism, which is indeed the origin of TMI, can be explained with the dynamical model. In this mechanism, the role of noise is only for triggering a stimulated scattering process when the threshold is reached. As discussed previously, H_{1111} and H_{2222} are the nonlinear refractive indices for self-phase modulation, H_{1122} and H_{2211} are the nonlinear refractive indices for cross-phase modulation, and H_{1221} and H_{2112} are the nonlinear refractive indices for modal coupling. The terms of self-phase modulation and cross-phase modulation cannot lead to modal coupling but only increase the phase variation of both FM and HOM due to the local thermal loading attributed to the quantum defect. The coupling terms, H_{1221} and H_{2112}, can not only influence the coupling of the modes but the phase variation. The occurrence of the modal coupling is associated to the existence of the phase lag between radiation beating pattern and the temperature grating. Without this phase lag, the coupling terms are like the self-phase modulation and cross-phase modulation terms only causing phase variation. This fact is explained in the following content.

If the gain from fiber amplifiers is neglected, Eq. (4.4-5) that is representing the phase variation and coupling of HOM is changed to

$$\frac{\partial A_2}{\partial \xi} = jk_0\left(H_{1122}+H_{2222}\right)A_2 + jk_0\left(H_{2112}\right)A_1 \tag{4.6-1}$$

Eq. (4.6-1) can be further transformed to the differential intensity equation of HOM as shown below

$$\frac{dI_2}{d\xi} = A_2^* \frac{dA_2}{d\xi} + A_2 \frac{dA_2^*}{d\xi} = -2k_0 \,\mathrm{Im}[H_{2112} A_1 A_2^*]$$
$$\propto -\mathrm{Im}\left[A_1(\xi,T) A_2^*(\xi,T) \cdot \int_0^T A_2(\xi,t') A_1^*(\xi,t') e^{-\frac{(t'-T)}{\tau}} dt' \right] \qquad (4.6\text{-}2)$$

One aspect is that Eq. (4.6-2) again explains the modal coupling (the change of HOM intensity) is only associated to H_{1221} and H_{2112}. Moreover, it indicates that the modal coupling exists only if the phase lag between the temperature grating, which is proportional to $\int_0^T A_2(\xi,t') A_1^*(\xi,t') e^{-\frac{(t'-T)}{\tau}} dt'$, and the radiation beating of the two mode, which is proportional to $A_1(\xi,T) A_2^*(\xi,T)$, is not equal to zero or an integer number of 2π. Thus, the existence of this phase lag is only attributed to the time-dependent amplitudes. If this dependence is eliminated, the thermal equilibrium is eventually reached, and the coupling between the modes would be ceased. This fact further clarifies the role of the noise source, which is most probably from spontaneous emission. The noise source perturbs the amplitude of both modes. In time domain, it spatially shifts the radiation beating from temperature grating and thus inducing the thermal nonlinear gain to one mode and the loss to the other, while in frequency domain, it means the frequency components around the gain peak is distinguishably amplified by the large gain around the fiber end.

With understanding this insight of TMI's origin, a more detailed analysis of time-dependent TBC should be discussed. Fig. 4.6-1 shows the analysis of TMI above threshold (250 W total output signal) with the power progression of the FM and HOM in (a) and (b), the thermal nonlinear refractive index presented as gain and phase coefficient in (c) and (d), and the induced shift between thermal grating and radiation beating in (e) and (f) at two different time moment $t = t_1$ and $t = t_2$ (t_1, $t_2 > 100$ ms). Fig. 4.6-1 (a) and (b) show

modal power versus distance at the two moments. The stronger coupling from FM to HOM both onsets at 0.85 m, which locates the threshold of the thermally-induced TBC. However, in these two figures, one can still find the distribution of the modal power is different.

Fig. 4.6-1 (c) and (d) shows at the two moments the normalized magnitude of $-\mathrm{Im}[H_{2112}A_1A_2^*]$ and $\mathrm{Re}[H_{2112}A_1A_2^*]$, which indicates the intensity gain and the phase variation experienced by the HOM. The blue curves represented the nonlinear amplification of HOM, which can be presented as the spatial phase shift between the temperature grating and the radiation interference in Fig. 4.6-1 (e) and (f). In the segment between 0.8 m to 0.85 m, one can observe that $\mathrm{Re}[H_{2112}A_1A_2^*]$ is 1 while $-\mathrm{Im}[H_{2112}A_1A_2^*]$ is 0. This means when thermal equilibrium is reached, due to the lack of the spatial shift between the two gratings, the coupling is ceased, and the two coupling terms H_{1221} and H_{2112} can only provide phase variation to the modes.

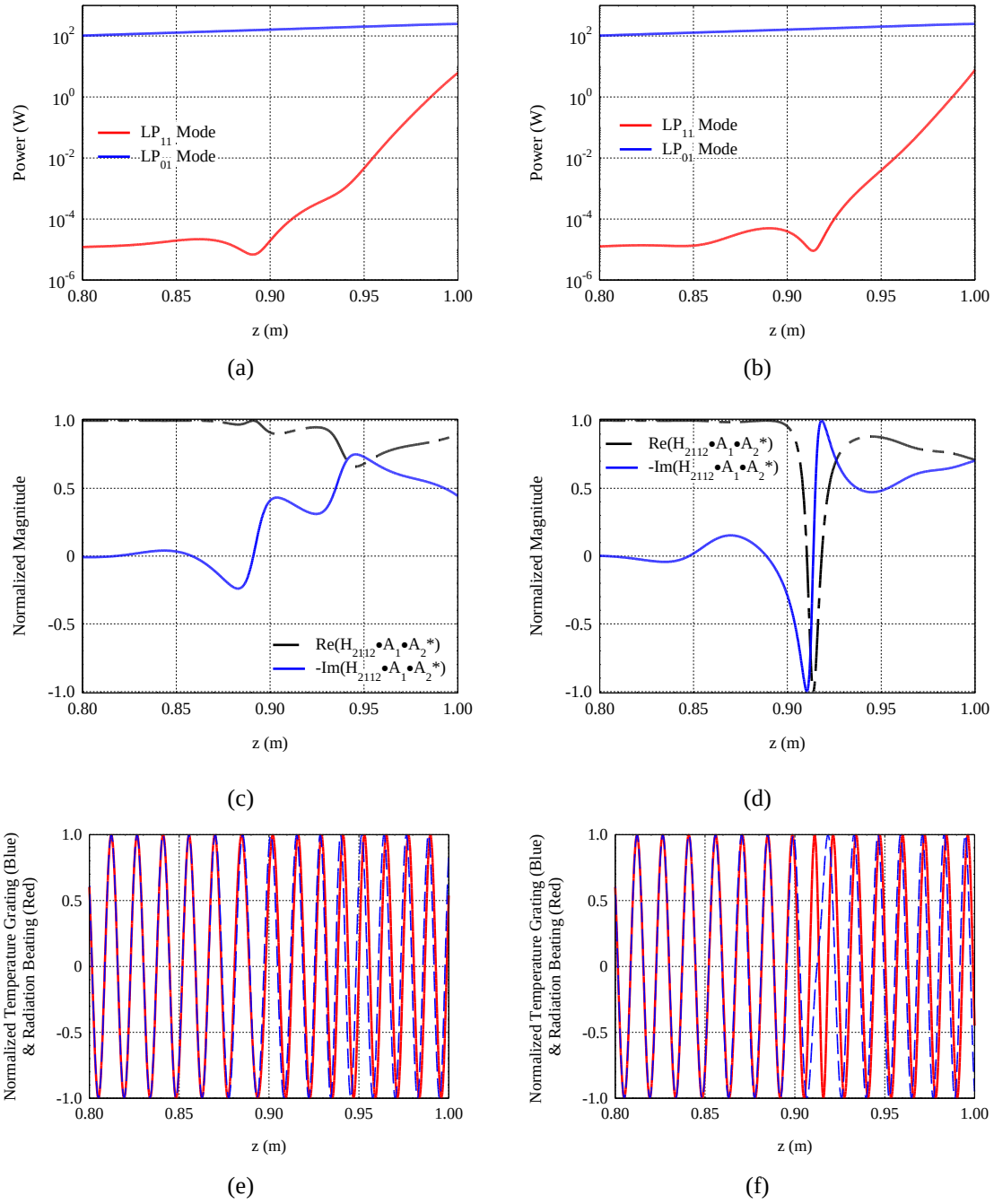

Fig. 4.6-1 (Top) The power progression of FM and HOM, (middle) normalized nonlinear refractive index presented as gain and phase coefficient, and (bottom) phase shift between thermal grating and radiation beating pattern of the fiber amplifier at 250-W output signal at two different time moment. (a)(c)(e) is captured at t_1, and (b)(d)(f) is captured at t_2.

The origin of TMI showing threshold-like chaotic oscillation between FM and HOM is explained. However, two other properties of TMI are still unexplainable in this field. The

first one is the harmonic oscillation between FM and HOM at the TMI threshold [25]. Even if this can be conceptually explained as an extrinsic modulation on the modes, the source of this modulation is still unknown. The second is about the built-up time of TMI when signal power is above threshold [26]. In the simulation with the dynamical model, the built-up of TMI is indeed observed. However, even if the output signal power is below threshold, the built-up of TMI with a chaotic process of reaching the thermal equilibrium still appears. Both cases indicates one or more factors which are not included in our scope. Definitely, these two specific phenomena in TMI are pending for us to explore in advance.

4.7 Conclusions

TMI is the newly found limitation on the power scalability of high power fiber lasers and amplifiers. When the threshold is reached, the output modal quality degrades and the oscillation between the FM and HOM appears. Based on the general TBC concept, an analytical theory was rigorously developed and shows that TMI is a particular case of it, and can be represented as a stimulated inter-modal scattering through thermally-induced nonlinear refractive index. Following the same steps as a general TBC theory presented in any standard textbook, a time dependent model of TMI is derived, and it can be further simplified to a static model. Advantage of the static model is that it allows calculating the TMI threshold, while the time-dependent model appears to reproduce key features of the TMI phenomenon that are observed experimentally.

Since TMI is originated from the fact that the fiber amplifier can support more than one transverse modes, the effective-single mode performance of CCC fibers can help mitigate its onset. The static model, in which the HOM attenuation is incorporated, is used to predict the required loss level of HOM for mitigating TMI. Overall, the total HOM attenuation is linearly proportional to the TMI threshold. For a 30μm-core step-index fiber amplifier with 0.07 NA, the TMI threshold increment versus total loss is 1.6W/dB. This indicates that in order to efficiently mitigate TMI in CCC fiber amplifiers, the scalability of HOM attenuation is the keynote.

Time-dependent TMI model qualitatively agrees with all key published experimental and numerical results. First, it predicts the threshold-like onset of propagation- and time-varying modal coupling with addition of spontaneous emission as the noise source. Second, kHz-frequency intermodal-coupling oscillations and the growing into broad-band chaos with increasing laser/amplifier power do occur. Third, the response time of the thermal

nonlinearity determines the kHz frequency offset between FM and HOM. Without considering this frequency offset, the unavoidable numerical noise is amplified in the high-gain TBC process presenting a mirage of TMI oscillation. This numerical noise is attributed to the round-off error in the calculation of thermal equilibrium.

The key feature of TBC energy couplings is due to the phase shift between the beating pattern of the modal intensity and the heat-load induced grating. This feature can be embodied by the onset of noise. Thus, the origin of TMI is inferred as the phase shift between the temperature grating and the radiation beating pattern triggered by the intrinsic noise, spontaneous emission, in high power fiber amplifiers.

Chapter V

Nonlinear Polarization Evolution in CCC Fiber Amplifiers

5.1 Introduction

5.1.1 Motivation

Polarization preservation at low peak power has been previously demonstrated in CCC fibers [80 , 81]. Recently, nonlinear polarization switching effects have been experimentally observed at high peak intensities in 35-µm core CCC fibers, which, depending on input polarization, can lead to either significant depolarization at the output or to a relatively well preserved linear output polarization with a fairly good polarization extinction ratio (PER) [82]. This prompted the need to explore, understand, and control this interesting phenomenon in all types of CCC fibers.

From both experimental observation and theoretical analysis of similar nonlinear polarization degradation and preservation effects in a 55µm polygonal-core CCC fiber amplifier, we recognized that the observed phenomena are associated with the nonlinear evolution of the polarization eigen-modes in a coiled CCC fiber amplifier. It occurs in a low-birefringence fiber, such as a CCC fiber, due to the presence of both linear (due to fiber coiling) and circular (due to fiber twisting) birefringence. Contribution of circular birefringence is critical in the sense that it makes normal mode intensity-dependent. This

dependency can be reduced by reducing the twisting induced circular birefringence: if the circular birefringence does not exist, the preservation of linear output polarization in a high peak power CCC fiber amplifier can always be achieved by seeding a linear polarization along slow axis. We also show that even with a small circular birefringence present one can find initial seeding conditions in the vicinity of the normal mode of propagation, which would preserve linear polarization to a high degree and under wide range of signal intensities. This finding indicates that CCC fibers can not only be applied to maintain polarization state in passive beam delivery with its low-birefringence property, but also to an intensity-independent preservation of linear output polarization in a high power amplifier through packaging the fibers without circular birefringence.

5.1.2 The Linear and Circular Birefringence in CCC-fiber Amplifiers

CCC fibers have been demonstrated and explained as polarization-preservation fibers [40]. This performance is attributed to several factors. On one hand, this property of CCC fibers is due to the spinning process of the fabrication, and this makes CCC fibers low-birefringent (Low-Bi) fibers. Such spun fibers help preserve the injected polarization status due to the randomly distributed intrinsic birefringence is averaged out along the fiber. On the other hand, the effective single-mode performance of CCC fibers help avoid the scattered higher-order modes which have different tracks of polarization evolution and different propagation velocity from the fundamental modes. However, the polarization-preservation property of CCC fibers is a prerequisite to the condition in which external perturbations are not exerted to them. In other words, any kind of external perturbation would directly induce a relevant birefringence in CCC fibers. When a CCC fiber is bent or

coiled, the induced linear birefringence $\Delta\beta$ with its fast axis parallel to the coiling plane can be quantified as [83]

$$\Delta\beta = 0.5 \cdot C_s \frac{r^2}{R^2} \tag{5.1-1}$$

where C_s is the strain-optic coefficient which is equal to 1.6×10^6 m^{-1} for fused silica medium operated at 1-μm wavelength. r is the fiber radius, and R is the coiling radius.

When a CCC fiber is twisted, the induced circular birefringence α is given by [84]

$$\alpha = hq \tag{5.1-2}$$

where q is the fiber twisted rate measured in radian per unit length, and h is about 0.159 for fused silica fiber operated at 1-μm wavelength.

Since CCC fiber is a Low-Bi fiber, when it is naturally packaged as a spool, externally induced linear birefringence due to bending can be comparable in magnitude to the circular birefringence due to twisting [40]. Therefore, an amplifier made with a packaged active CCC fiber can contain both linear and circular birefringence.

5.1.3 Linear Polarization Evolution and Eigen-polarizations

When an optical wave propagates through a medium, its polarization status can be changed due to the existence of birefringence. Birefringence means the two polarization modes which are consist of a polarization basis experience different refractive indices because the material response to the two modes is different. This kind of medium is defined as birefringent. A linear birefringent fiber indicates two linear polarization eigen-modes oscillating along the two fiber axes respectively; while for circular birefringent media, these two polarization eigen-modes are the two circular polarizations, right-handed circular polarization (RCP) and left-handed circular polarization (LCP). When an eigen-mode

optical waves propagates through a medium, its polarization status is maintained. When the launched polarization is not the eigen-mode, polarization evolution occurs.

An optical waves propagating in a birefringent fiber can be written by

$$\vec{E} = \frac{1}{2}\left(E_x \hat{x} + E_y \hat{y}\right) \cdot e^{-j\omega_0 t} + c.c. \tag{5.1-3}$$

where $E_i = A_i(z) \cdot \psi_i(r_\perp) \cdot e^{j\beta_i z}$. A_i is the slowly varying amplitude along longitudinal direction, ψ_i is the profile of the transverse mode supported by the fiber, β_i is the corresponding propagation constant ($i = x, y$). Here, $E_x \hat{x}$ and $E_y \hat{y}$ are the two eigen-modes of this birefringent optical fiber. The difference between β_x and β_y indicates the linear birefringence $\Delta\beta = \beta_x - \beta_y$. A similar concept of eigen-mode can also be applied to circular polarizations with circular birefringence.

In the following paragraphs, a theoretical review of the polarization evolution attributed to both linear and circular birefringence is introduced. The field components propagating in the fiber must satisfy Maxwell's wave equation,

$$\frac{d^2 \vec{E}}{dz^2} + \left(\frac{\omega}{c}\right)^2 \bar{\varepsilon} \vec{E} = 0 \tag{5.1-4}$$

$\bar{\varepsilon}$ is a dielectric tensor. Assuming both linear and circular birefringence are considered, $\bar{\varepsilon}$ can be shown as [85]

$$\varepsilon \equiv \begin{pmatrix} \varepsilon_{xx} & j\frac{\eta}{2} \\ -j\frac{\eta}{2} & \varepsilon_{yy} \end{pmatrix} \tag{5.1-5}$$

The diagonal terms accounts for the linear birefringence ($\varepsilon_{xx} \neq \varepsilon_{yy}$), while the imaginary

off-diagonal terms represents the twist-induced circular birefringence. η is defined by $\eta \equiv \frac{n\alpha}{k_0}$, where k_0 is the wave number in vacuum and α is circular birefringence.

If both types of birefringence exists ($\varepsilon_{xx} = \varepsilon_{yy} \neq 0, \eta \neq 0$), by substituting Eq. (5.1-3) and Eq. (5.1-5) into Eq. (5.1-4), considering slowly-varying approximation, and further defining $\frac{\varepsilon_{xx} + \varepsilon_{yy}}{2} = n^2$ and $\frac{\varepsilon_{xx} - \varepsilon_{yy}}{2} = n \cdot \Delta n$, a pair of coupled amplitude equations can be derived as

$$\frac{dA_{x,y}}{dz} = \mp \frac{\alpha}{2} A_{y,x} \tag{5.1-6}$$

Eq. (5.1-6) concludes that circular birefringence couples the two components of linear polarization since they are not the eigen-modes.

On the other hand, the field can also be resolved into complex circularly polarized components by explicitly writing the field amplitude and phase as

$$E_{\pm}(z)e^{ikz} = \frac{E_x(z) \mp jE_y(z)}{\sqrt{2}} \tag{5.1-7}$$

where *k* is the average of the propagation constants β_x and β_y. Eq. (5.1-4) can also be expanded using the circularly polarized basis fields shown in Eq. (5.1-7). With a few algebra, a pair of coupled field equations is obtained for the two circularly polarized modes $E_{\pm}$:

$$\frac{dE_{\pm}}{dz} = \mp \frac{\alpha}{2} E_{\pm} + i \frac{\Delta\beta}{2} E_{\mp} \tag{5.1-8}$$

Eq. (5.1-8) shows that linear birefringence couples circular polarization modes.

Even though either Eq. (5.1-6) accompanying with Eq. (5.1-3) and Eq. (5.1-8) can fully describe the polarization evolution in a birefringent medium, the polarization evolution is inconvenient to visualize using this description. While the use of Poincaré

Sphere can much ease this visualization.

5.1.4 Poincaré Sphere and Stokes Vactors

In order to visualize the polarization state of a light wave, a polarization ellipse is broadly used. As shown in Fig. 5.1-1 (a), the ellipse is the polarization state in the laboratory coordinates (*x* and *y*). The semi-major and semi-minor axes of this ellipse can also be used to define the other coordinate system (*x'* and *y'*). ψ is the angle of rotation about *z*-axis from the laboratory coordinate system to elliptical coordinate system, and it defines the azimuth angle of this polarization state. The ellipticity angle χ is defined by axial ratio of this ellipse. These two angles are known as Poincaré parameters, which can be directly applied to the Poincaré sphere.

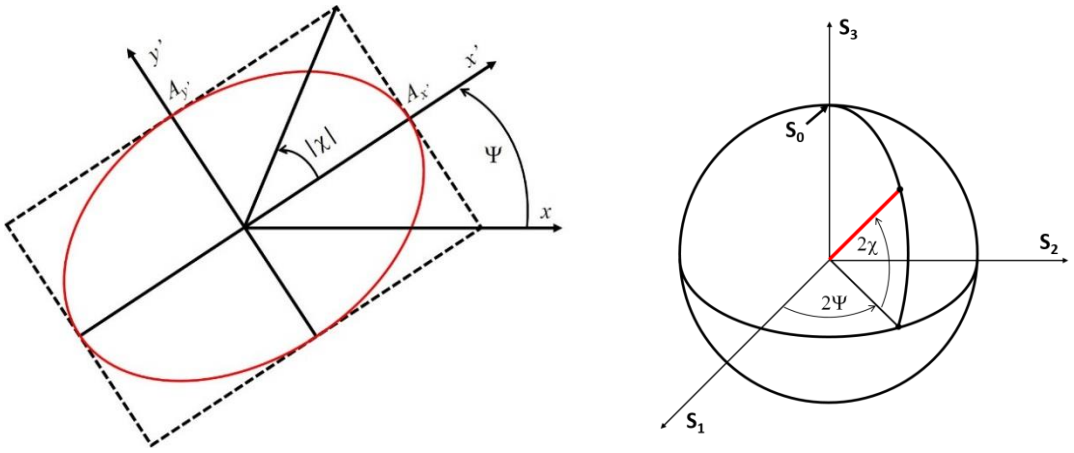

(a) (b)

Fig. 5.1-1 (a) Polarization ellipse (b) Poincaré Sphere

Fig. 5.1-1 (b) shows the Poincaré sphere. The Poincaré parameters defined in the polarization ellipse have a one-to-one mapping to the Poincaré sphere. The angle 2ψ and

2χ marks the longitude and latitude respectively. Thus, this configuration indicates the linear polarization states with different azimuth angle are around the equator, and the right-handed and left-handed circular polarization are at the north and south poles respectively. All the other elliptical polarization states are between the poles and the equator.

Since each point on the Poincaré sphere can be described by the Poincaré parameters ψ and χ thus defining a system of Cartesian vectors, which is known as Stokes vector or S-vector. A normal Stokes vector is constructed by the four components of Stokes parameters S_0, S_1, S_2, and S_3. If letting $S_0 = 1$, the Poincaré sphere is a unit sphere, and only S_1, S_2, and S_3 are needed to describe the polarization status of a light wave. The relationship between these parameters are listed as the following [86]:

$$S_0^2 = S_1^2 + S_2^2 + S_3^2 = P_0^2 \tag{5.1-9}$$

where

$$\begin{aligned} S_0 &= |A_x|^2 + |A_y|^2 \\ S_1 &= |A_x|^2 - |A_y|^2 \\ S_2 &= 2\,\mathrm{Re}\left[A_x^* A_y\right] \\ S_3 &= 2\,\mathrm{Im}\left[A_x^* A_y\right] \end{aligned} \tag{5.1-10}$$

and P_0 is the total power of the optical wave, which is the physical meaning of S_0. If the optical waves is described by the basis of circular polarizations. The relationship in Eq. (5.1-7) can be used to convert Eq. (5.1-10) to

$$\begin{aligned} S_0 &= |A_+|^2 + |A_-|^2 \\ S_1 &= 2\,\mathrm{Re}\left[A_-^* A_+\right] \end{aligned} \tag{5.1-11}$$

$$S_2 = 2\,\mathrm{Im}\left[A_-^* A_+\right]$$

$$S_3 = \left|A_-\right|^2 - \left|A_+\right|^2$$

Thus, from these expressions of the Stokes parameters, the physical meaning of them can be inferred. S_1 represents the power difference of *x*-polarized fraction from y-polarized fraction of the optical wave. Thus, if $S_1 = P_0$ means the optical wave is entirely polarized at *x*-direction, while $S_1 = -P_0$ means it is entirely polarized at *y*-direction. S_2 represents the power difference of +45°-polarized fraction from -45°-polarized fraction of the optical wave. S_3 represents the power difference of RC-polarized fraction from LC-polarized fraction of the optical wave. Since the Stokes parameters can be directly connected with the Poincaré sphere, Stokes vector $\vec{S} = \left[S_1 \quad S_2 \quad S_3\right]$, which is originated at the zero point in the Stokes coordinate, can be further defined on it to indicate a polarization state. The length of the Stokes vector is the total power. Thus, applying Eq. (5.1-11) to Eq. (5.1-8), we can use the displacement of a Stokes vector to describe a polarization evolution with the onset of birefringence on the Poincaré sphere. This step eases the visualization of nonlinear polarization evolution.

5.2 Nonlinear Polarization Evolution Description on the Poincaré Sphere

When an optical wave with strong enough intensity passes through an optical fiber, nonlinear Kerr effect will change the local refractive index as well as the birefringence. Under this condition, the Maxwell's equation is modified as [15]

$$\frac{d^2\vec{E}}{dz^2}+\left(\frac{\omega}{c}\right)^2\vec{\varepsilon}\vec{E}=-\mu_0\omega^2\overrightarrow{P^{NL}} \tag{5.2-1}$$

The $\overrightarrow{P^{NL}}$ is the nonlinearly-induced material polarization. For optical fibers made by fused silica, the third susceptibility in an isotropic medium is considered. The nonlinear polarization components thus can be presented as

$$\begin{aligned} P_x^{NL}&=\left(\frac{\chi\varepsilon_0}{2}\right)\left[\left(\left|E_x\right|^2+\left|E_y\right|^2\right)E_x+\frac{1}{2}\left(E_x^2+E_y^2\right)E_x^*\right]\\ P_y^{NL}&=\left(\frac{\chi\varepsilon_0}{2}\right)\left[\left(\left|E_x\right|^2+\left|E_y\right|^2\right)E_y+\frac{1}{2}\left(E_x^2+E_y^2\right)E_y^*\right] \end{aligned} \tag{5.2-2}$$

By substituting Eq. (5.2-2) into Eq. (5.2-1), considering slowly-varying approximation, and converting the linear-polarization basis into circular-polarization one with Eq. (5.1-7), the coupled amplitude equations with nonlinear birefringence included are given by

$$\frac{dE_\pm}{dz}=\mp i\frac{\alpha}{2}E_\pm+i\frac{\Delta\beta}{2}E_\mp+i\frac{2\gamma}{3}\left(\left|E_\pm\right|^2+2\left|E_\mp\right|^2\right)E_\pm \tag{5.2-3}$$

where γ is the nonlinear coefficient which is defined by $\gamma\equiv\frac{n_2\omega}{A_{eff}c}$. This coefficient quantifies the strength of nonlinearity with nonlinear refractive index coefficient n_2 and effective mode area A_{eff}. In order to more clearly visualize the nonlinear polarization evolution, Eq. (5.2-3) can be converted into a vectorial differential equation with a Stokes vector $\vec{S}=\begin{bmatrix}S_1 & S_2 & S_3\end{bmatrix}$ and a birefringence vector $\overrightarrow{W}$. This conversion results in a full description of the nonlinear polarization evolution which can be summarized as

$$\frac{d\vec{S}}{dz} = \overrightarrow{W} \times \vec{S}$$
$$\overrightarrow{W} = \overrightarrow{W_L} + \overrightarrow{W_{NL}} \qquad (5.2\text{-}4)$$

where $\overrightarrow{W_L} = \begin{bmatrix} -\Delta\beta & 0 & \alpha \end{bmatrix}$ and $\overrightarrow{W_{NL}} = \begin{bmatrix} 0 & 0 & \frac{2\gamma}{3} S_3 \end{bmatrix}$. The vectorial differential equation in Eq. (5.2-4) describes the route of polarization evolution on the Poincaré sphere. This route is determined by the cross product of the birefringence vector and the Stokes vector. The three components in the birefringence vector represent three different types of birefringence. The first one is the linear birefringence, the second is the linear birefringence with 45^o azimuth angle to the fiber axes, and the third one is the circular birefringence. One can see the complicated nonlinear refractive indices in Eq. (5.2-3) is replaced with a single term in $\overrightarrow{W_{NL}}$ and this term is proportional to S_3. This proportionality indicates nonlinear ellipse rotation [15]. As long as an optical wave is elliptically polarized ($S_3 \neq 0$), the polarization is influenced by the nonlinear birefringence.

In short, this model in "Stokes domain" largely simplifies the mathematical expression of nonlinear polarization coupling and can be easily applied on the Poincaré sphere for the purpose of visualization. Thus, the properties of nonlinear polarization evolution can be conveniently described. In the following subsections, the influence of linear birefringence and circular birefringence to nonlinear birefringence will be discussed.

5.2.1 NPE in an optical fiber with only linear birefringence

A birefringent fiber, such as a polarization-maintaining (PM) fiber or a bent CCC fiber without being twisted, is an optical fiber with linear birefringence. The linear polarization in this kind of fiber is preserved when the polarization azimuth angle is aligned with the

optic axis. When such a fiber is delivering an optical wave of high peak power, the birefringence vector that includes nonlinear birefringence in it is $\vec{W} = \left[-\Delta\beta \quad 0 \quad \frac{2\gamma}{3} S_3 \right]$. In order to find eigen-modes, i.e. fixed or stable points, on the Poincaré sphere, we need to solve $\frac{d\vec{S}}{dz} = 0$.

The cross product in Eq. (5.2-4) gives

$$\begin{cases} -\Delta\beta \cdot S_2 = 0 \\ \Delta\beta \cdot S_3 + 2\gamma/3 \cdot S_1 \cdot S_3 = 0 \\ -2\gamma/3 \cdot S_2 \cdot S_3 = 0 \end{cases} \tag{5.2-5}$$

The possible solutions of Eq. (5.2-5) are given by

$$\begin{cases} S_1 \neq 0, S_2 = 0, S_3 = 0 \quad \text{(Solutnio \#1)} \\ S_1 = -3\Delta\beta/2\gamma, S_2 = 0, S_3 \neq 0 \quad \text{(Solution \#2)} \end{cases} \tag{5.2-6}$$

Solution #1 corresponds to linear polarized eigen-modes, which are represented by $\vec{S} = \left[\pm P_0 \quad 0 \quad 0 \right]$ on the Poincaré sphere. These two modes are present at any powers. The other solution refers to two other eigen-modes appearing due to the onset of nonlinear birefringence. If we define $P_{cr}^{'} = -\frac{3\Delta\beta}{2\gamma}$ ($\Delta\beta < 0$ is always expected in coiled silica fibers.), by using Eq. (5.1-9), we can obtain the locations of these points on the Poincaré sphere. These two points given by $\vec{S} = \left[P_{cr}^{'} \quad 0 \quad \pm\sqrt{P_0^2 - P_{cr}^{'2}} \right]$ are symmetrically at the opposite sides about the fast axis. This result reveals that these two additional eigen-modes exist only if the total power P_0 exceeds $P_{cr}^{'}$. Moreover, it also indicates $\vec{S} = \left[+ P_0 \quad 0 \quad 0 \right]$ is an unstable point which splits into three points. This occurs as a result of the disappearance of the birefringence due to the nonlinearly increased refractive index at the fast axis. In order to visualize this phenomenon, the polarization evolution is depicted in

Fig. 5.2-1. In this figure, (a) and (b) respectively show the trajectories of Stokes-vector motion on the front side and back side of the Poincaré sphere when the power level is lower than P_{cr} , while (c) and (d) shows them when the power level is higher than P_{cr}. These two sets of Poincaré sphere reveals that the fast axis (x-axis) is the eigen-mode which splits into three, i.e. two additional stable eigen-modes split from the unstable point at the fast axis. If the input wave is polarized along this fast axis, small changes in the input polarization will result in large changes at the output polarization. This is so called polarization instability which specifically happens at the fast axis [15]. The two new eigen-modes, split from the unstable eigen-mode, indicates the associated elliptical eigen-polarizations at which the nonlinear ellipse rotation is exactly balanced with the linear birefringence.

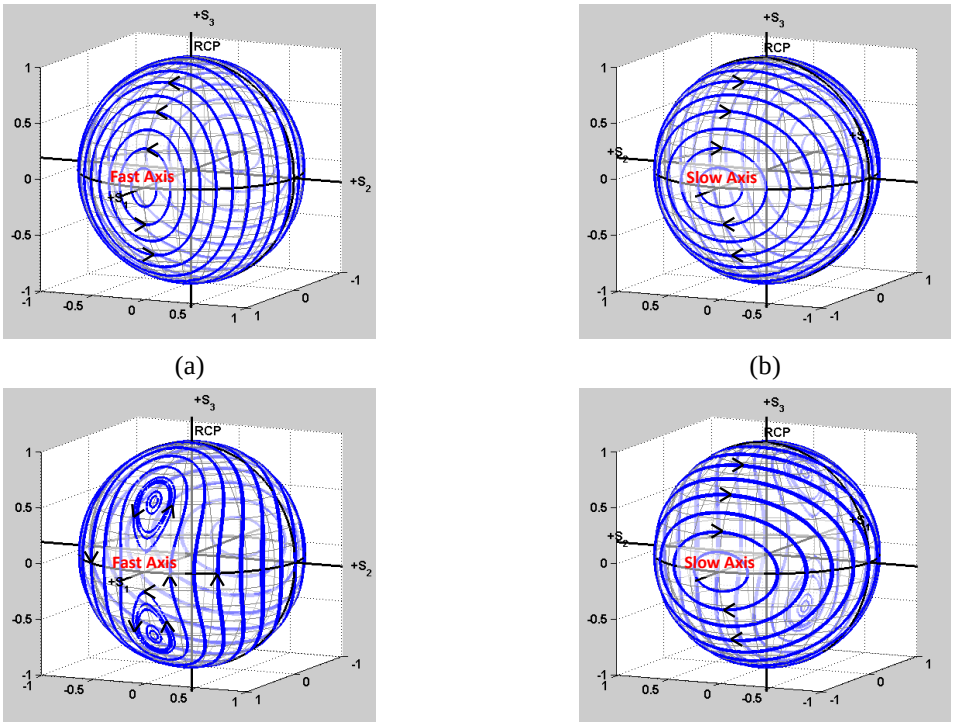

Fig. 5.2-1 Trajectories of Stokes-vector motion on the Poincaré sphere showing the splitting of the eigen-modes when the power level is larger than P_{cr}. (a) and (b) are the case with $\Delta\beta > 0$ and $P_0 = 0.5 \cdot P_{cr}$; (c) and (d) are the case with $\Delta\beta > 0$ and $P_0 = 1.5 \cdot P_{cr}$

5.2.2 NPE in a Coiled CCC Fiber

According to the explanation in Sec. 5.1.3, because CCC fibers are spun fibers, the external perturbation is directly reflected on the induced birefringence. When such fibers are coiled, a comparable linear birefringence and circular birefringence can be induced simultaneously. This configuration of the induced birefringence should be distinguished from the case of twisted polarization-maintaining (PM) fibers. In a twisted PM fiber, the optical axis is rotated with the twisting, while in a coiled CCC fiber, the optical axis is kept parallel to the coiling plane. Thus, the birefringence structure is entirely different. Since the case of twisted PM fiber is already analyzed [87], we will only focus on the birefringence of coiled CCC fibers that has not been considered yet.

The birefringence vector $\vec{W}$ in which linear birefringence, circular birefringence, and nonlinear birefringence are all included can be written as $\vec{W} = \left[-\Delta\beta \quad 0 \quad \alpha + \frac{2\gamma}{3} S_3 \right]$. By setting $\frac{d\vec{S}}{dz} = 0$, the eigen-modes on the Poincaré sphere can be solved. The derived equations are given by

$$\begin{cases} -\Delta\beta \cdot S_2 = 0 \\ \alpha \cdot S_1 + \Delta\beta \cdot S_3 + 2\gamma/3 \cdot S_1 \cdot S_3 = 0 \\ -\alpha \cdot S_2 - 2\gamma/3 \cdot S_2 \cdot S_3 = 0 \end{cases} \tag{5.2-7}$$

In Eq. (5.2-7), $S_2 = 0$ is easily observed. The other equation which need more algebra to solve is $\alpha S_1 + \Delta\beta S_3 + \frac{2\gamma}{3} S_1 S_3 = 0$, which can be organized as

$$S_1 = \frac{-\Delta\beta S_3}{\alpha + \frac{2\gamma}{3} S_3} \tag{5.2-8}$$

In addition, since $S_2 = 0$, the other implicit equation which indicates the energy conservation is

$$S_1^2 + S_3^2 = S_0^2 = P_0^2 \tag{5.2-9}$$

Therefore, we can combine these two equations, and obtain a quartic equation of S_3 as

$$\left(\frac{2\gamma}{3}\right)^2 S_3^4 + 2\left(\frac{2\gamma}{3}\right)\alpha S_3^3 + \left(\alpha^2 + \Delta\beta^2 - \left(\frac{2\gamma}{3}\right)^2 P_0^2\right) S_3^2 - 2\left(\frac{2\gamma}{3}\right)\alpha P_0^2 S_3 - P_0^2\alpha^2 = 0 \tag{5.2-10}$$

However, the solution of Eq. (5.2-10) can be implicitly reached by analyzing the transition of solution number with the method introduced later on. Our goal is to obtain the critical power at which one of the polarization eigen-mode becomes unstable and two more eigen-modes are split. In other words, the path of solving this quartic equation is to look for the conditions in which the solution number of S_3 becomes four from two.

Eq. (5.2-10) can be rewritten as $aS_3^4 + bS_3^3 + cS_3^2 + dS_3 + e = 0$, and the parameters are defined as $a \equiv \left(\frac{2\gamma}{3}\right)^2$, $b \equiv 2\left(\frac{2\gamma}{3}\right)\alpha$, $c \equiv \alpha^2 + \Delta\beta^2 - \left(\frac{2\gamma}{3}\right)^2 P_0^2$, $d \equiv -2\left(\frac{2\gamma}{3}\right)\alpha P_0^2$, and $e \equiv -P_0^2\alpha^2$. The solution number of S_3 in this equation can be judged from the discriminant of Δ [88]

$$\Delta_1^2 - 4\Delta_0^3 = -27\Delta \tag{5.2-11}$$

where Δ_0 and Δ_1 are defined by

$$\Delta_0 = c^2 - 3bd + 12ae \tag{5.2-12}$$

$$\Delta_1 = 2c^3 - 9bcd + 27b^2e + 27ad^2 - 72ace \tag{5.2-13}$$

$\Delta < 0$ indicates that Eq. (5.2-10) has 2 real roots, and $\Delta > 0$ indicates that Eq. (5.2-10) has four real roots. If we define $P_{cr}^{'} = -\frac{3\Delta\beta}{2\gamma}$ and the ratio of P_0 to $P_{cr}^{'}$ as η, Eq. (5.2-12) and (5.2-13) becomes

$$\Delta_0 = \left[\left(\eta^2 - 1\right)\cdot\Delta\beta^2 - \alpha^2\right]^2 \tag{5.2-14}$$

$$\Delta_1 = -2\left[\left(\eta^2 - 1\right)\cdot\Delta\beta^2 - \alpha^2\right]^3 + 108\cdot\eta^2\cdot\Delta\beta^2\cdot\alpha^2 \tag{5.2-15}$$

Then from Eq. (5.2-11), we can obtain

$$\frac{-27\Delta}{108\cdot\eta^2\cdot\Delta\beta^2\cdot\alpha^2} = 108\cdot\eta^2\cdot\Delta\beta^2\cdot\alpha^2 - 4\left[\left(\eta^2 - 1\right)\cdot\Delta\beta^2 - \alpha^2\right]^3 \tag{5.2-16}$$

Eq. (5.2-16) reveals that the solution of the critical power satisfies

$$108\cdot\eta_{cr}^2\cdot\Delta\beta^2\cdot\alpha^2 - 4\left[\left(\eta_{cr}^2 - 1\right)\cdot\Delta\beta^2 - \alpha^2\right]^3 = 0 \tag{5.2-17}$$

Eq. (5.2-17) can be solved as a cubic equation of η_{cr}. If we define $\delta = \frac{\alpha}{-\Delta\beta}$, the solution of Eq. (5.2-17) is

$$\eta_{cr} = \sqrt{\left[1+\sqrt[3]{\delta^2}\right]^3} \tag{5.2-18}$$

From (5.2-18), the critical power with considering both linear and circular birefringence thus can be given by

$$P_{cr} = P_{cr}^{'}\sqrt{\left[1+\sqrt[3]{\delta^2}\right]^3} \tag{5.2-19}$$

In Fig. 5.2-2, the trajectories of Stokes-vector motion on the Poincaré sphere with $\alpha = -\Delta\beta > 0$ are depicted. (a) and (b) are the case with the launched power lower than this updated critical power by the amount of $0.5P_{cr}$; (c) and (d) are the case with the launched power above the critical power by the amount of $0.5P_{cr}$. The evolution shown in these figures reveals the nonlinear polarization evolution in a coiled CCC fiber is no longer symmetrical concerning the interchange of RCP and LCP. This fact indicates that due to the existence of nonlinear birefringence, the entire circular birefringence in the upper hemisphere is enhanced while it at the lower hemisphere is suppressed. When the power level reaches P_{cr}, the splitting eigen-mode close to the fast axis is where both linear and circular birefringence are fully cancelled by nonlinear birefringence thus inducing an unstable eigen-mode, and is also where the polarization instability occurs. Any input polarization situated close to the unstable eigen-mode may evolve drastically when being slightly perturbed. When the power level is above P_{cr}, the eigen-mode split from the unstable point indicates where the circular birefringence is cancelled by nonlinear birefringence and linear birefringence is balanced. If the input power level is increased further, the entire polarization evolution would be close to the case without circular birefringence as discussed in Sec. 5.2.1. Two eigen-modes represent the elliptical eigen-polarization would go closer to the two poles, and both the unstable (close to fast axis) and the stable (close to slow axis) eigen-modes would go closer to the equator.

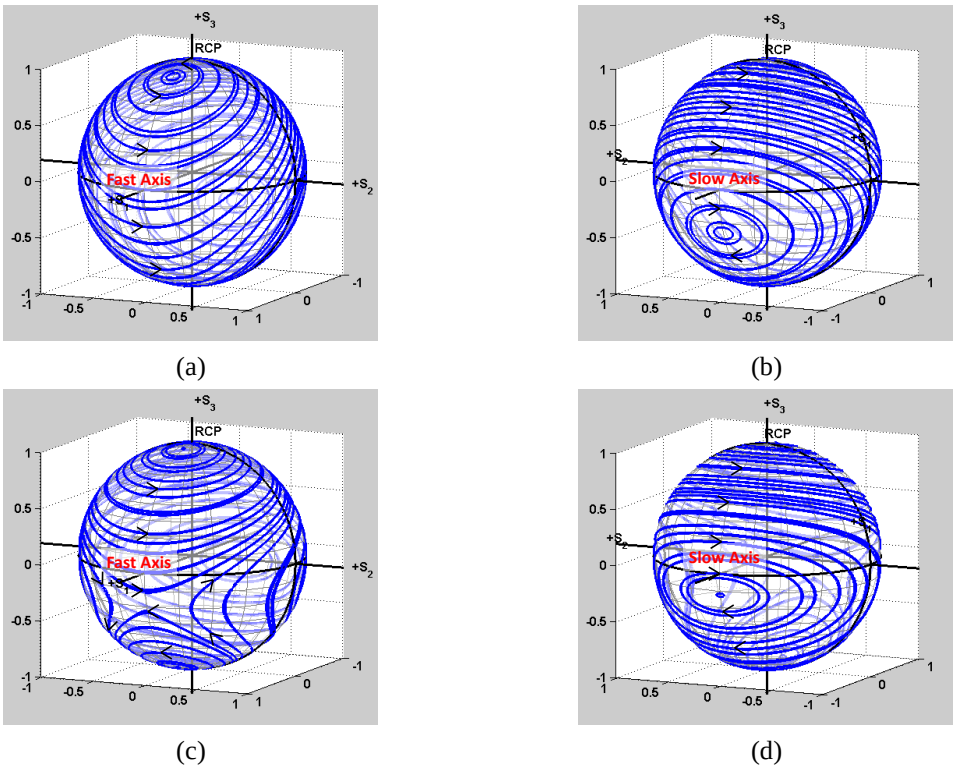

Fig. 5.2-2 Trajectories of Stokes-vector motion on the Poincaré sphere with $-\alpha = \Delta\beta < 0$. (a) and (b): $P_0 = 0.5P_{cr}$; (c) and (d): $P_0 = 1.5P_{cr}$

On the other hand, since the critical power is obtained, the splitting point around the fast axis can be derived. The combination of Eq. (5.2-8) and Eq. (5.2-9) gives the square of the normalized power level $\eta\,(=\frac{P_0}{P_{cr}^{'}})$ which can be expressed as

$$\eta^2 = \frac{\overline{s_3}^2}{\left[\overline{s_3} + \delta\right]^2} + \overline{s_3}^2 \equiv f\left(\overline{s_3}\right) \tag{5.2-20}$$

where $\overline{s_{3(1)}} \equiv \mathrm{S}_{3(1)} / P_{cr}^{'}$ representing the S_3 normalized by $P_{cr}^{'}$. This critical power $P_{cr}^{'}$ is the one without considering circular birefringence. Since we have known η_{cr} occurs at the local minimum of $f\left(\overline{s_3}\right)$, we can equate the derivative of $f\left(\overline{s_3}\right)$ to zero and solve it

for the root to obtain the value of $\overline{s_3}$ and the minimum of *f*. The solution is

$$\overline{s_3} = -\delta - \sqrt[3]{\delta} \tag{5.2-21}$$

Eq. (5.2-21) can be substituted into Eq. (5.2-20) to obtain η_{cr} as Eq. (5.2-19) shows. Using Eq. (5.2-9), the form of $\overline{s_1}$ can also be obtained

$$\overline{s_1} = 1 + \sqrt[3]{\delta^2} \tag{5.2-22}$$

Eq. (5.2-20) to Eq. (5.2-22) are applied to calculate the splitting eigen-mode on the Poincaré sphere.

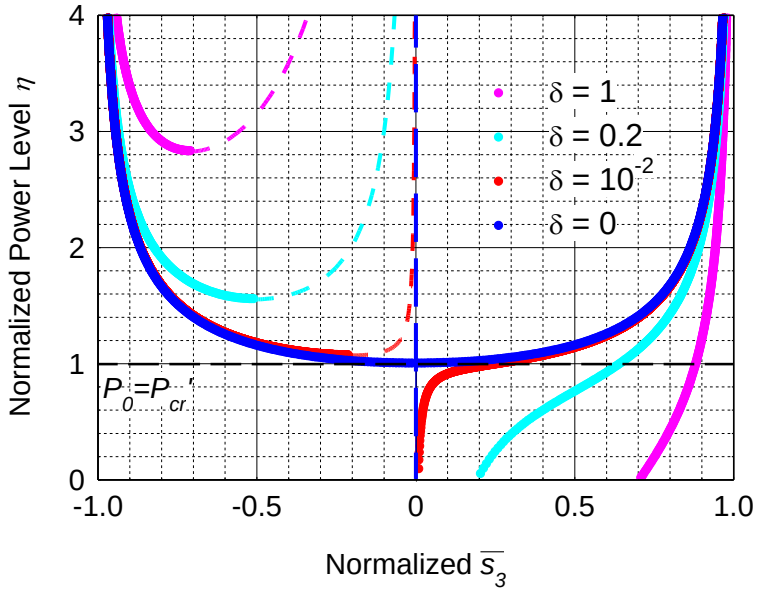

Fig. 5.2-3 Bifurcation diagram showing the normalized power level η versus the normalized S_3 coordinate of the critical points (with $S_2 = 0$, $S_1 > 0$) for four different birefringence ratio, $\delta = 0$, 10^{-2}, 0.2, and 1. (Solid line: stable eigen-mode; dashed line: unstable eigen-mode)

Calculated by Eq. (5.2-20), Fig. 5.2-3 quantifies the eigen-mode evolution that is discussed in this section by showing the relationship between η and the normalized Stokes

parameter $\overline{s_3}$ at four different δ values with only the part of $\overline{s_1} > 0$ being considered. The $\overline{s_3}$ value of the relevant eigen-modes can be determined by the intersection of these curves with a constant power level, i.e η is a constant. The reason to only involve η of $\overline{s_1} > 0$ is because of the $\overline{s_3}$ value and variation of the stable eigen-mode close to slow-axis ($\overline{s_1} < 0$), which is marked by slow mode, resembles them of the unstable eigen-mode close to fast-axis ($\overline{s_1} > 0$), which is marked by fast mode. In other words, the value and variation of the fast mode represents them of the slow mode.

Fig. 5.2-3 reveals an important fact: the intensity-independent eigen-modes only exists when circular birefringence is absent. When δ is zero, the fast mode becomes unstable with two new symmetrical stable eigen-modes split from it at the critical power $P_{cr}^{'}$. This case is explained in the last subsection. It means without circular birefringence, two of the eigen-modes, the stable slow mode and the unstable fast mode, stay as intensity-independent linear polarizations. For the case of δ=10^{-2}, a slight amount of circular birefringence leads to a dramatic change of the "on-axis" slow and fast modes as the normalized power level η is close to one. The overall variation of the eigen-mode with the power level is quite similar to the case of δ= 0. For the case of δ= 0.2 or 1, the eigen-mode configuration highly depends on the power level and the occurrence of the unstable fast mode and the two split stable eigen-modes requires higher power to achieve. If the power level is further increased, two stable eigen-modes can still move towards the pole ($\overline{s_3} = \pm 1$) of the Poincaré sphere, and the other two still move towards to the equator ($\overline{s_3} = 0$). The above analysis recapitulates the process of eigen-mode splitting with different

birefringence ratios.

5.3 The Preservation of Linear Polarization Output in CCC Fiber Amplifiers

According to the theory of the nonlinear polarization evolution introduced in Sec. 5.2, the polarization states of the fast and slow eigen-modes can be intensity-independent only if the circular polarization is zero. Thus robust, intensity-independent preservation of linear output polarization can be achieved in a CCC fiber amplifier only if its coiling-induced twisting is eliminated, and input light is launched into the slow eigen-mode (since fast eigen-mode is not stable). We did observe experimentally that preservation of linear output polarization can still be achieved within a wide range of output peak power when a specific seeding condition is satisfied, but since this is not associated with any eigen-mode, long-term stability of this state cannot be ensured. We used this observation to "calibrate" the agreement between our theoretical model and experimental results, verifying good correspondence between the two. In the following two subsections, this experimental and modeling work is discussed in detail.

5.3.1 Linear Polarization Preservation within a Wide Range of Output Peak Power

The preservation of linear output polarization is demonstrated in a 55-μm core CCC fiber amplifier shown that in a CCC fiber amplifier with a properly selected input polarization angle. The experimental setup is shown in Fig. 5.3-1. A 2.3m piece of 55μm-polygonal-core active CCC fiber coiled to 45cm diameter is used as the gain medium of a counter-pumped fiber amplifier. This fiber amplifier is seeded with a 12-ns pulse operated at 5 kHz repetition rate, and the pulse energy is 80 μJ (approximately 6.5 kW). The polarization controlling components, HWP 1, HWP 2, QWP, and PBS, are inserted at the seeding end, and the polarization measurement components, HWP 3 and PBS, are at the

pumping end. The beam blocker at the seeding end avoids the polarization controlling components from being heated by the pump through, and the beam blocker at the output end is to eliminate the cladding light which is close to unpolarized and can influence the signal polarization measurement. The output beam from the amplifier partially transmits through a wedge for power measurement and is partially coupled to a single mode fiber for pulse and spectra measurement.

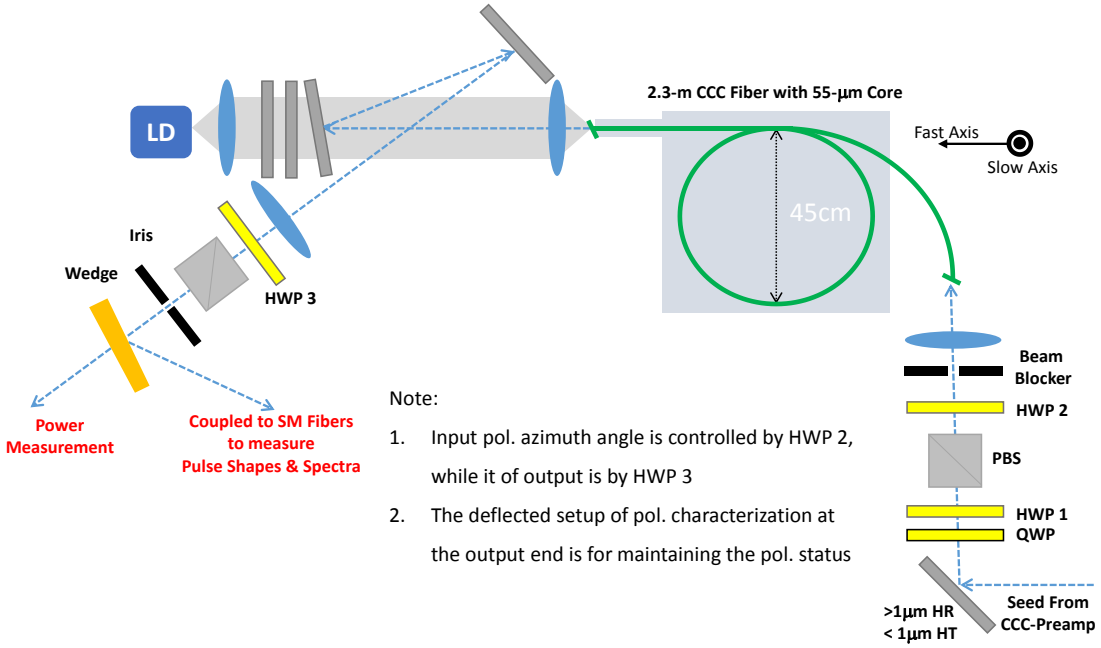

Fig. 5.3-1 Experimental layout for demonstrating the preservation of linear polarization output at high peak power in a 2.3-m 55-mm-core CCC fiber amplifier.

In this experiment, an input linear polarization at two different azimuth angles, one can achieve the preservation of linear output polarization and one cannot, is seeded the CCC fiber amplifier. The output polarization extinction ratio (PER) and the azimuth angle are characterized. The experiment result is shown in Fig. 5.3-2, in which the two curves respectively represent the output PER versus the output peak power at the two seeding

azimuth angles of linear polarization. An output azimuth angle is marked by each data point.

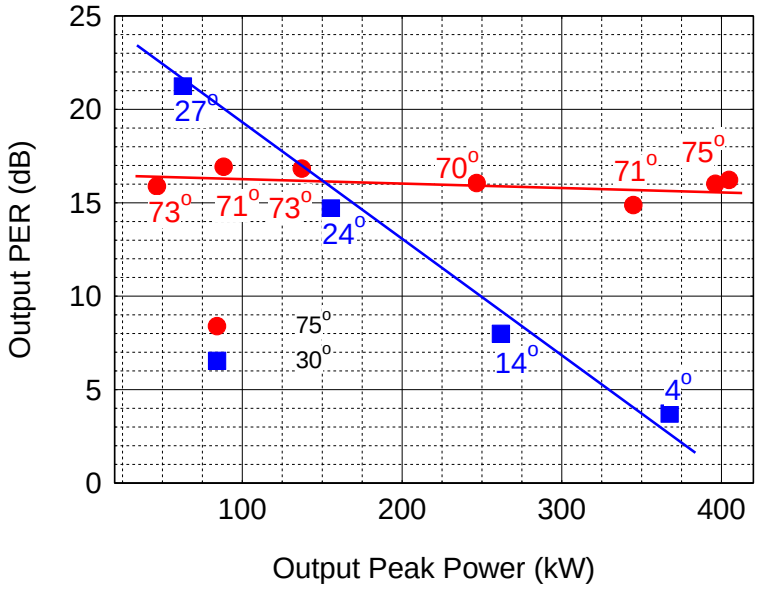

Fig. 5.3-2 The red markers show an intensity-independent output PER with negligible change of azimuth angle while the other curve shows a degraded PER with noticeable angle change when the peak power is getting higher. The output azimuth angle is marked by the data points.

One can observe that the curve of 75° input azimuth angle shows a 16dB output PER is independent of the output peak powers and the variation of the output azimuth angle is within 5°. This fact indicates the linear output polarization is preserved at up to 400-kW peak power. As for the other input polarization angle, depolarization occurs at high peak power and the output PER is being degraded from 23 dB to 3 dB, accompanying with a 23°-rotation of the output azimuth angle. This experimental result reveals that by selecting a proper input azimuth angle, like 75° in this case, the linear output polarization can be preserved.

5.3.2 Theoretical Modeling of Linear Polarization Preservation

Here we compare the obtained experimental results with our theoretical model to validate the agreement between the two. First of all, the differential equation of the Stokes vector should be replaced with

$$\frac{d\vec{S}}{dz} = \vec{W} \times \vec{S} + g\vec{S} \tag{5.3-1}$$

where g is the power gain coefficient from fiber amplifiers. If gain saturation is ignored, this gain coefficient indicates an exponential growth of the power in fiber amplifiers.

However, Eq. (5.3-1) reveals a trajectory on an expanding Poincaré sphere. In order to simplify it, we define $S_0(z) = S_0^{in} \cdot e^{gz}$, and thus we can further define $\tilde{s}_1(z) = S_1(z)/S_0(z)$, $\tilde{s}_2(z) = S_2(z)/S_0(z)$, and $\tilde{s}_3(z) = S_3(z)/S_0(z)$. Therefore, Eq. (5.3-1) can be rewritten as

$$\frac{d\tilde{\vec{s}}}{dz} = \vec{W} \times \tilde{\vec{s}} \tag{5.3-2}$$

where $\tilde{\vec{s}} = [\tilde{s}_1(z) \quad \tilde{s}_2(z) \quad \tilde{s}_3(z)]$ and $\vec{W} = [-\Delta\beta(z) \quad 0 \quad \alpha(z) - \eta(z)\cdot\tilde{s}_3(z)]$. Here, the parameters η defined in Sec. 5.2 is used, and the birefringence is assumed z-dependent. Using Eq. (5.3-2), the polarization evolution can be described on a unit Poincaré sphere.

In order to model a nonlinear polarization evolution in a CCC-fiber amplifier, the birefringence of CCC fibers should be characterized. The following is the recapitulation of the birefringence in CCC fibers. A CCC fiber is a spun fiber, which eliminates all internal random birefringence perturbations making it a Lo-Bi fiber. Since this is a flexible fiber that is usually coiled when packaged, accurate model for nonlinear polarization evolution should include external-perturbation effects such as linear birefringence induced by coil-bending, and circular birefringence induced by the twisting of the fiber. According to the

fiber coiling diameters shown in Fig. 5.3-1, the characterized linear and circular birefringence are both 0.45 m^{-1} respectively. In addition, since the MFD of this fiber is known as 42 μm^{-2}, using Eq. (5.2-19), the critical power can be calculated as 17.5 kW. It means the nonlinear eigen-mode splitting occurs at the very beginning end of the fiber.

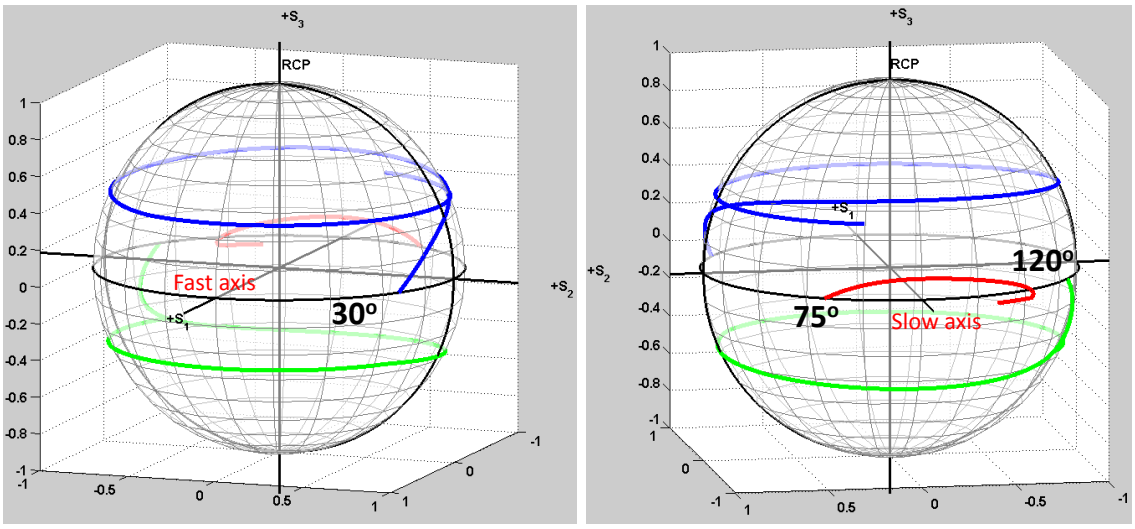

(a) (b)

Fig. 5.3-3 Trajectories of Stokes-vector motion of different input pol. angle to the 55-mm-core CCC fiber amplifiers with 400 kW peak power output. (a) is the front side and (b) is the back side.

Fig. 5.3-3 shows the numerical simulation result calculated by the modified model shown in Eq. (5.3-2) at 400 kW output peak power for three different input linear polarization angles. (a) shows the front side trajectories on the Poincaré sphere, while (b) shows the back side of the Poincaré sphere. This result again indicates when the launched azimuth angle is 75°, the trajectory of the polarization evolution goes around the slow-axis and preserved at the high-PER zone. While for the other input polarization angles, 30° or 120°, the polarization state can easily evolve to elliptical state at the low-PER zone and experience a dramatic nonlinear ellipse rotation there. Usually, the degradation of the

output PER is not because the polarization state evolves to a low-PER zone, but because the polarization state rotates dramatically thus leading to a depolarization within a high peak power pulse.

With this theoretical analysis, the existence of the input polarization state producing linearly-polarized and intensity-independent (within some peak-power range) output is confirmed, and in this specific case, this point has been verified close to the zone around 75^o azimuth angle. As long as the input polarization state is chosen around this point, within a range of output peak power, the output PER degradation and the azimuth angle rotation is negligible. The concept of such an input polarization state can be understood as the following property of nonlinear polarization evolution. The trajectory of the polarization evolution around the slow axis is relative stable. When the output power is larger than critical power ($P > P_{cr}$), trajectories starting from around the fast axis tend to proceed away from linear-polarization equator into the low-PER zone; while when starting from around the slow axis, the trajectories tend to remain close to linear polarization (i.e. high-PER).

However, the above concept only gives the sense of achieving linear output polarization preservation at high peak power output, and a more detailed analysis is definitely needed. As the trajectory of the red curves (with 75^o –input azimuth angle) in Fig. 5.3-3 (b) shows, the turning of this curve tells the rotation of the polarization is initiated, a further push of the output peak power will lead to a degradation of the output PER due to the nonlinear ellipse rotation on the lower hemisphere of the Poincaré sphere. The result of numerical optimization tells that the input polarization state which can lead to the preservation of linear output polarization at high peak power is actually elliptical polarization instead of linear polarization, as shown in Fig. 5.3-4. In this figure, the left elliptical polarization at 75^o azimuthal angle is found the optimized polarization state for

achieving the preservation of linear output polarization in a wide range of output peak power (3 to 500 kW). With 3 kW input peak power, the trajectories that indicates different output peak powers are overlapped and all end at the same point on the equator of the Poincaré sphere.

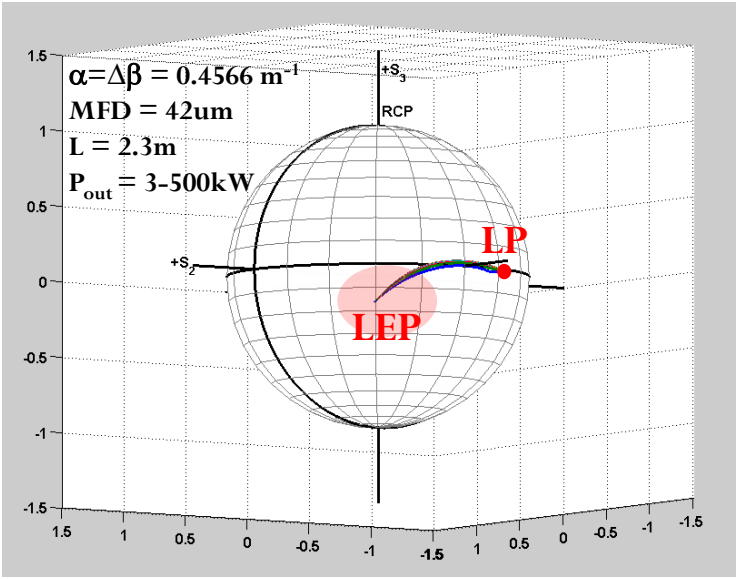

Fig. 5.3-4 The simulation of nonlinear polarization evolution in the CCC-fiber amplifier shown in Fig. 5.3-1 with optimized input polarization state (left elliptical polatization, LEP) for the preservation of linear output polarization (LP) at high peak powers

The reason that elliptical polarization with 75^{o} azimiuth angle leads to the preservation of linear polarization output is due to the existence of circular birefringence. Recalling the nonlinear polarization evolution discussed in Subsec. 5.2.1, the absence of circular birefringence makes the polarization state along the slow axis as an intensity-independent linear polarized slow mode. The 75^{o} linear polarization is only applicable, within a limited power range, to a specific fiber amplifiers packaged with a comparable linear birefringence and circular birefringence. Assume that the circular birefringence is being reduced, this stabilizing point can be predicted moving toward 90^{o} which is linear polarized slow mode,

as shown in Fig. 5.3-5. Therefore, the final comment is that in order to achieve the preservation of linear polarization output, the focus should alternatively be on the elimination of circular birefringence. According to the Low-Bi property of CCC fibers, an intuitive method of realizing zero circular birefringence is untwisting the CCC fiber amplifier by the amount that is concurrently induced by fiber coiling. However, the feasibility of this work is still unknown, and a further demonstration is in progress.

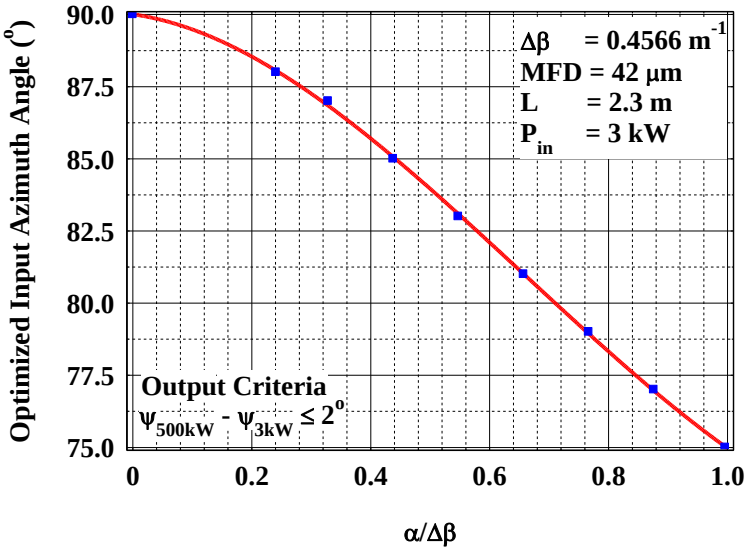

Fig. 5.3-5 The relationship between the optimized input azimuth angle and the amount of circular birefringence in the coiled CCC-fiber amplifier shown in Fig. 5.3-1. The criteria of the optimized input azimuth angle is determined by <2° output azimuthal angle difference of 500kW-output case from 3kW-output case.

5.4 Conclusion

In a CCC fiber, since fiber is spun during fabrication, all internal birefringence contributions are effectively “erased”, and the fiber is inherently a low birefringent fiber. Since a flexible fiber is usually coiled when packaged, moderate amounts of “external” linear birefringence due to coil-bending, and circular birefringence due to the concurrent twisting of the fiber are thus induced in CCC fibers. This affects signal polarization at high peak powers due to the occurring nonlinear polarization evolution. Below the critical power, two eigen-modes (stable points), one is right-elliptical polarization and the other is left-elliptical polarization, exist in the polarization evolution. Above the critical power, two additional eigen-modes, one is close to the fast axis (unstable) and the other one (stable) is close to the pole, appear in the polarization evolution and increasing the power moves two of the stable points towards each poles and one closer to the equator. Thus, the transition from 2 eigen-modes to 4 eigen-modes occurs when a polarized signal propagates along a high peak power CCC fiber amplifier. When a linearly polarized signal at a specific azimuthal angle is seeded, the preservation of the linear output polarization can be achieved while at other angles, the degradation of the linear output polarization occurs.

We experimentally demonstrate the preservation of linear polarization output at a particular input azimuth angle 75^{o}, which appears to be an effective stabilizing input polarization angle. Experiment agrees well with numerical simulations using nonlinear polarization evolution model. In general, this finding determines a correct input condition based on the ratio of linear and circular birefringence for achieving the preservation of linear output polarization from a coiled and concurrently twisted large-core effectively-single-mode fibers with very low intrinsic birefringence. However, this approach can only be applicable within a limited output power range.

Strictly speaking, this operation condition is not associated with any polarization eigen-mode, and therefore cannot guarantee long-term stability. More robust solution for achieving robust linearly polarized output at any output peak power should be sought by launching input signal into a slow eigen-mode of a CCC fiber, which is packaged without any twist. However, experimental verification of this is in progress but has not been achieved yet.

Chapter VI

Design Principe of Polygonal-core CCC Fibers

6.1 Introduction

In Chapter III, two types of chirally coupled core (CCC) fibers, one is with single-side core and the other is with 8-side cores, are used to demonstrate the suppression of stimulated Raman scattering (SRS) through their tailored transmission spectra that are one important features of CCC fibers. An effective CCC fiber for SRS suppression requires at least 30 dB/m loss at the Stokes wave and <1 dB/m loss at the signal wave. In Chapter IV, CCC fibers are again proposed a solution to mitigate transverse mode instabilities (TMI) with the other important feature of CCC fibers, the effective single-mode (E-SM) operation. These two cases directly indicate that in order to control nonlinearities in passive large-mode-area (LMA) fibers or in high power fiber amplifiers, the design work of CCC fibers plays a critical role.

In CCC fibers, the HOMs are selectively leaked from the central core to the cladding, while the fundamental mode (FM) is kept in the central core with a negligibly small loss so that the E-SM performance can be achieved. E-SM operation is achieved only if the HOM loss is larger than 10's of dB/m and the FM loss is smaller than 1 dB/m. This E-SM operation is achieved by the previously reported CCC fibers with a single side core through a quasi-phase-matched (QPM) coupling of HOM from the central core into the side core. The coupled light in the side core is attenuated due to the curvature of the side core, which

leads to the frustration of total internal reflection. For this type of CCC fibers, the core size can only be scaled up to 40μm diameter with E-SM performance being maintained [38]. The main reason of this limitation is due to the decrease of the modal overlap between central core and side core. The increased size of the central core leads to weaker HOM coupling into the side core. According to the calculation result in ref [89], the optimized suppression of LP_{11} mode in a CCC fiber degrades from >400 dB/m to <50 dB/m when the core size changes from 30μm to 100μm.

In order to resolve the issue of weaker modal overlap with the increasing of the central core size, the 8-side and octagon-shaped central core CCC fibers are developed and are further demonstrated the capability of being operated as effectively single-mode with core sizes larger than 50μm diameter [39]. Being different from the old-type CCC fibers with a single side core, it couples central-core HOM into central-core leaky modes which are radiating directly into the cladding. Compared to the modal overlap between central-core mode and side-core mode, the modal overlap between central-core guided and leaky modes is much less dependent on the central-core size, so the core-size scaling of E-SM CCC fibers is available. This new type of CCC structure is shown in Fig. 6.1-1. The two major features which distinguish this structure from the old-type CCC geometry are: 1) the central core is polygonal (octagonal in particular); 2) the off-axis side cores are positioned around each vertex of the central core. Adding the 7 more side cores is to increase the perturbation to the central core thus enhancing the suppression of the HOM. Due to the spinning in the fabrication process of this type of CCC fibers, the central core acquires a twisted polygon shape, with a twisting period Λ, while the off-axis side cores become helically winding around the central core with the same period. Therefore, this new structure is labeled as "Polygonal-CCC" (P-CCC) fiber to distinguish it from the old-typed CCC fibers as

"Single-side CCC" (S-CCC) fibers.

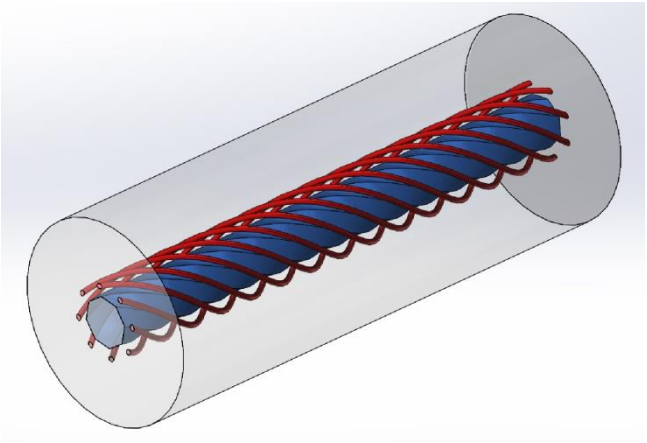

Fig. 6.1-1 The structure of polygonal-CCC fiber : the on-axis central core has a polygonal shape (octagon in this example), and each the side core (8 side cores in this case) is positioned at the vertices of this polygon.

Since both S-CCC structure and P-CCC structure are helically symmetric, the invariance property of such structure indicates the modal interactions can only occur between the supported helically-symmetric modes which possess orbital angular momentum coming from modal field-distribution rotation and spin angular momentum coming from vectorial rotation of modal field. As previously reported, the QPM conditions for S-CCC is [38]

$$\Delta\beta = \beta_{l_1 m_1} - \beta_{l_2 m_2}\sqrt{1+K^2R^2} - \Delta m \cdot K = 0 \tag{6.1-1}$$

where $\beta_{l_1 m_1}$ is the propagation constants of fiber modal group $LP_{l_1 m_1}$ in straight central core with modal number l_1 and m_1, $\beta_{l_2 m_2}$ is the propagation constants of fiber modal group $LP_{l_2 m_2}$ in straight side core with modal number l_2, and m_2, the factor $\sqrt{1+K^2R^2}$ is for a helical correction for the helically wound side core, $\Delta m = \Delta l + \Delta s$ in which

$\Delta l = \pm l_1 \pm l_2$ is associated to the orbital angular momentum degeneracy and geometrical perturbation, and Δs = -2, −1, 0, + 1, and + 2 (only 5 possible values) is associated to spin angular momentum degeneracy and anisotropic perturbation (i.e. localized linear and circular birefringence) between the central core and the single side core.

The QPM intra-core modal coupling in P-CCC fibers only needs orbital angular momenta to achieve phase matching. Due to large separation distances between central core and side cores, anisotropic birefringence perturbation between them is too small to be exploited in P-CCC structure. The reduced overlap among the enlarged central-core mode, the side core mode, and the perturbation presented as an anisotropic birefringence cannot support an efficient QPM modal coupling in this new type of CCC structure. Consequently, singly accounting for orbital angular momentum and geometrical perturbations in the QPM conditions of P-CCC fibers is sufficient

$$\Delta\beta = \beta_{l_1 m_1} - \beta_{l_2 m_2} - \Delta l \cdot K = 0 \tag{6.1-2}$$

where $\beta_{l_1 m_1}$ and $\beta_{l_2 m_2}$ are both from central core, and $\Delta l = \pm l_1 \pm l_2$ due to orbital angular momentum degeneracy and geometrical perturbation.

However, even if the QPM condition of the in-core modal coupling in P-CCC fiber is predicted, the detailed principle of modal coupling and the relevant constraint needs more investigation. Basically, the known part is that P-CCC fibers produces HOM suppression through the following processes: the central core guided modes can be coupled into leaky modes through the helically symmetric core structure, which acts as a helical perturbation for the interacting modes. Because of this symmetry, this perturbation only lead to modal couplings between helical symmetric modes. Consequently, QPM description of CCC interactions still applies, i.e. phase-matching between the modes involves both modal

propagation constants and their angular momenta. However, if there is no need to consider both linear and circular birefringence, then only orbital angular momenta are involved, and circular polarization (i.e. spin-orbital angular momentum) is not relevant. Thus, the non-zero overlap integral between the guided and the leaky modes over this perturbation determines the onset of modal coupling in P-CCC fibers.

Based on the above fact, the principle of the modal coupling due to the polygonal symmetry are mathematically proved. In addition, because of the need to fully suppress HOMs, the bending-induced mixture of HOM helical modes are further analyzed. These works are highly associated to the suppression of nonlinearities such as SRS and TMI in P-CCC fibers.

6.2 Coupled mode theory in P-CCC fibers

6.2.1 The Polygonal Perturbation

In P-CCC fibers, guided core modes can couple into leaky modes. This coupling occurs via the perturbation from the helically-symmetric polygonal core structure. As shown in Fig. 6.2-1, the modal interactions occur in the octagonal core can be thought as among the modes supported by the inscribed round core (green) surrounded by the cladding (grey) that are perturbed by the octagonal structure (red), including the octagonal ring of the core and the existence of the 8 side cores. This perturbation can only lead to the modal coupling between helically symmetric modes since interacting modes must be invariant with helical translation. In the following content, this point is proved with the coupled mode theory.

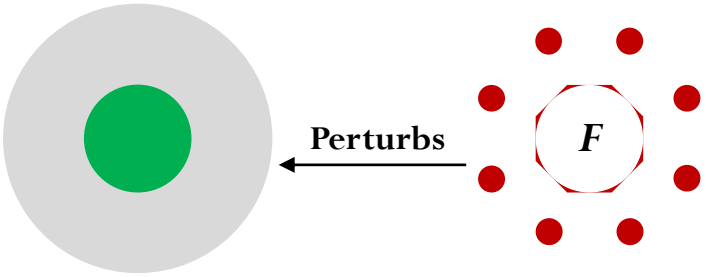

Fig. 6.2-1 The transverse profile of an octogonal-core CCC fiber is decomposed into two part. The polygonal ring and the 8 side cores (red) serve as the perturbation to the mode supported by the round core (green) surrounded by the clading (grey).

The helical structure and the limited influence of local birefringence constraints the eigen-mode as linearly-polarized helical mode $LP_{lm}^{\pm}$, where ± means the two different rotation direction of modal wave front, and *l*, *m* are respectively the azimuthal and radial modal numbers. The optical waves of helical modes in fibers that are described in a helical

frame can be written as

$$E_{lm} = A_{lm}(z)\cdot\Gamma_{lm}(r)\cdot e^{jl\theta}\cdot e^{j\left[\left(\beta_{lm}+l\frac{2\pi}{\Lambda}\right)z-\omega t\right]} \tag{6.2-1}$$

, where A_{lm} is the amplitude, Γ_{lm} is the radial modal profile, β_{lm} is the modal propagation constant, Λ is the pitch of the rotating period, *l* and *m* are both the modal index of the modes. In the helical frame, a perturbation of polygonal symmetry resembled the shown in Fig. 6.2-1 on the transverse plane which rotates and varies along the longitudinal direction can be mathematically described as

$$\Delta n = F\left[\theta - \frac{2\pi}{N}\ floor\left(\frac{N\theta+\pi}{2\pi}\right)\right] \tag{6.2-2}$$

This perturbation is presented as an "arbitrary" function *F* which has N-fold rotational symmetry. This polygonal symmetry with N sides are described by the floor function which makes *F* a local function in the range of $-\frac{\pi}{N} \le \theta \le \frac{\pi}{N}$. For calculating the modal overlap with polygon-shaped perturbation, the radial dependence of the supported modes can be ignored ($A_{lm} \to A_l$ and $\beta_{lm} \to \beta_l$), since the variation of such perturbation, as shown in Eq. (6.2-2), is only dependent on azimuthal angles.

The coupled equations, incorporated with Eq. (6.2-1) and Eq. (6.2-2), can be written as [90]

$$\frac{dA_l}{dz} = i\kappa_{ll'}A_{l'}e^{j\left(\beta_l-\beta_{l'}+(l-l')\frac{2\pi}{\Lambda}\right)z} \tag{6.2-3}$$

where $\kappa_{ll'}$ is the coupling coefficient, and it is defined as

$$\begin{aligned}\kappa_{ll'} &\equiv k_0\int\Gamma_l(r)e^{jl\theta}\cdot\Delta n\cdot\Gamma_{l'}(r)e^{jl'\theta}\cdot dr_\perp \\ &= k_0\int_0^\infty\Gamma_l(r)\Gamma_{l'}(r)rdr\int_0^{2\pi}Fe^{j(l-l')\theta}d\theta\end{aligned} \tag{6.2-4}$$

where $l \neq l'$ is presumed. This indicates the modal coupling between LP_{0x} and LP_{0y} ($x \neq y$) is excluded, since they are orthogonal in their radial dependence. With this presumption, the radial integral of the beating pattern between the two modes in Eq. (6.2-4) would not vanish but only determines the magnitude of the coupling coefficient, thus we only need to analyze the integral along the azimuth angle for proving the existence of the modal coupling.

Eq. (6.2-3) indicates two required factors which determines the occurrence of the modal coupling through the polygonal symmetric perturbation. One is that the modal coupling coefficient $\kappa_{ll'}$ should be nonzero, and the other one is the phase-matching of the modal coupling should be achieved ($\Delta k = 0$).

6.2.2 Modal Interactions in P-CCC Fibers

In following derivation, $\kappa_{ll'}$ is proved to be nonzero only if the value of $l - l'$ equals an integer number of N, which is the side number of the polygon-shaped core. Here, the difference of the modal number between any two modes are defined by $\Delta l \equiv l - l'$, so the coupling coefficient can be written as

$$\begin{aligned}
\kappa_{ll'} &\propto \int_0^{2\pi} F e^{j\cdot\Delta l\cdot\theta} d\theta \\
&= \int_{-\frac{\pi}{N}}^{\frac{\pi}{N}} F\left(\theta - \frac{2\pi}{N}\cdot 0\right)\cdot e^{i\cdot\Delta l\cdot\theta} d\theta + \int_{\frac{\pi}{N}}^{3\frac{\pi}{N}} F\left(\theta - \frac{2\pi}{N}\cdot 1\right)\cdot e^{i\cdot\Delta l\cdot\theta} d\theta \\
&+ \ldots + \int_{(2N-5)\frac{\pi}{N}}^{(2N-3)\frac{\pi}{N}} F\left(\theta - \frac{2\pi}{N}(N-2)\right)\cdot e^{i\cdot\Delta l\cdot\theta} d\theta + \int_{(2N-3)\frac{\pi}{N}}^{(2N-1)\frac{\pi}{N}} F\left(\theta - \frac{2\pi}{N}(N-1)\right)\cdot e^{i\cdot\Delta l\cdot\theta} d\theta
\end{aligned} \tag{6.2-5}$$

By defining $\theta_n \equiv \theta - n \cdot \frac{2\pi}{N}$, where $n = 0, 1, 2, 3...N-1$, Eq. (6.2-5) can be rewritten as

$$\begin{aligned}
\kappa_{ll'} &\propto \int_0^{2\pi} F \cdot e^{j\cdot\Delta l\cdot\theta} d\theta \\
&= \int_{-\frac{\pi}{N}}^{\frac{\pi}{N}} F(\theta_0)\cdot e^{j\cdot\Delta l\cdot\theta_0} d\theta_0 + \int_{-\frac{\pi}{N}}^{\frac{\pi}{N}} F(\theta_1)\cdot e^{j\left(\Delta l\cdot\theta_1 + \frac{\Delta l}{N}\cdot 2\pi\right)} d\theta_1 + ... \\
&+ \int_{-\frac{\pi}{N}}^{\frac{\pi}{N}} F(\theta_{N-2})\cdot e^{j\left(\Delta l\cdot\theta_{N-2} + \frac{\Delta l}{N}\cdot(N-2)\cdot 2\pi\right)} d\theta_{N-2} + \int_{-\frac{\pi}{N}}^{\frac{\pi}{N}} F(\theta_{N-1})\cdot e^{j\left(\Delta l\cdot\theta_{N-1} + \frac{\Delta l}{N}\cdot(N-1)\cdot 2\pi\right)} d\theta_{N-1} \\
&= \int_{-\frac{\pi}{N}}^{\frac{\pi}{N}} F(\theta')\cdot e^{j\cdot\Delta l\cdot\theta'} \left[1 + e^{j\cdot 1\cdot\frac{\Delta l}{N}\cdot 2\pi} + ... + e^{j\cdot(N-2)\cdot\frac{\Delta l}{N}\cdot 2\pi} + e^{j\cdot(N-1)\cdot\frac{\Delta l}{N}\cdot 2\pi}\right] d\theta'
\end{aligned} \tag{6.2-6}$$

The summation of the N phasor terms in the above square parenthesis is given by

$$1 + e^{j\cdot 1\cdot\frac{\Delta l}{N}\cdot 2\pi} + ... + e^{j\cdot(N-2)\cdot\frac{\Delta l}{N}\cdot 2\pi} + e^{j\cdot(N-1)\cdot\frac{\Delta l}{N}\cdot 2\pi} = \begin{cases} 0, \Delta l \neq \pm N, \pm 2N, \pm 3N, ... \\ N, \Delta l = \pm N, \pm 2N, \pm 3N, ... \end{cases} \tag{6.2-7}$$

Thus, the $\kappa_{ll'}$ can be determined as

$$\kappa_{ll'} \propto \int_0^{2\pi} F \cdot e^{j\cdot\Delta l\cdot\theta} d\theta = \begin{cases} 0 & , \Delta l \neq \pm N, \pm 2N, \pm 3N, .. \\ N\int_{-\frac{\pi}{N}}^{\frac{\pi}{N}} F(\theta)\cdot e^{j\cdot\Delta l\cdot\theta} d\theta & , \Delta l = \pm N, \pm 2N, \pm 3N, .. \end{cases} \tag{6.2-8}$$

Eq. (6.2-8) indicates the relationship between the geometry of the perturbation and the existence of modal coupling between two modes with modal number *l* and *l'* respectively. For example, an octagonal core P-CCC fiber can couple the guided HOM to leaky modes with the modal number difference between them equaling to the multiples of 8, since the selection rule determined by the geometry of the octagon-shaped perturbation indicates an "octave" apart modal coupling. Table 6.2-1 shows the potential modal coupling from the first three orders of fiber modes to leaky modes via the octagon-shaped perturbation. Through the octagonal perturbation, LP_{11} mode can be coupled to LP_{9x} mode or LP_{7x} mode,

and LP_{21} mode can be coupled to LP_{10x} mode or LP_{6x} mode. In this scheme, HOMs such as LP_{11} mode or LP_{21} mode in the central core thus can be attenuated by directly radiating into the cladding. In principle, this intra-core coupling in P-CCC fibers is much stronger than the inter-core coupling in S-CCC fiber when the central core size is getting larger.

Table 6.2-1 The first three orders of LP helical modes that are capable of being coupled to the leaky modes via the perturbation provided by an octogon-shapded core

<table>
<tr><th>$|l|$</th><th colspan="2">Guided Modes</th><th>Leaky Modes</th></tr>
<tr><td>0</td><td colspan="2">LP_{01}</td><td>LP_{8x}</td></tr>
<tr><td rowspan="4">1</td><td rowspan="4">LP_{11}</td><td rowspan="2">LP_{11}^{+}</td><td>LP_{9x}^{+}</td></tr>
<tr><td>LP_{7x}^{-}</td></tr>
<tr><td rowspan="2">LP_{11}^{-}</td><td>LP_{7x}^{+}</td></tr>
<tr><td>LP_{9x}^{-}</td></tr>
<tr><td rowspan="4">2</td><td rowspan="4">LP_{21}</td><td rowspan="2">LP_{21}^{+}</td><td>LP_{10x}^{+}</td></tr>
<tr><td>LP_{6x}^{-}</td></tr>
<tr><td rowspan="2">LP_{21}^{-}</td><td>LP_{6x}^{+}</td></tr>
<tr><td>LP_{10x}^{-}</td></tr>
</table>

This theory is interpreted as the selection rule of the coupling modes. This selection rule determines the achievable coupling between two modes, one is guided mode and the other can be leaky mode. When the modal number difference of two modes matches the perturbation symmetry, the coupling between them occurs. Thus, this selection rule reveals that when the modal coupling occurs, the beating pattern of these two modes must possess the same symmetry as the perturbation. This point of view can also be applied to the achieving of phase-matching condition. The phase matching condition of a modal coupling process is achieved when the beating of the coupled modes matches the rotation rate and direction of the helical structure. However, due to the constraint from the fiber structure of

single chirality, only one of the degenerate modes can be coupled to a higher-order mode, leaky mode in particular, fiber bending must be included in the design consideration for HOM suppression.

6.3 The Mixture of Helical Modes by Bending Fibers

In the last section, the mechanism of modal coupling due to the onset perturbation of polygonal symmetry is modeled. According to the selection rule shown in Eq. (6.2-8), an octagonal perturbation can induce the modal coupling from LP_{11}^{+} mode to LP_{91}^{+} mode or LP_{71}^{-} mode, or from LP_{11}^{-} mode to LP_{91}^{-} mode or LP_{71}^{+} mode and so on. With this modal coupling mechanism, the main goal is to achieve effective single-mode (E-SM) operation by phase-matching HOMs to leaky modes in P-CCC fibers. However, due to the modal dispersion and single helicity of the structure, the modal coupling of both degenerate helical modes cannot happen at the same wavelength. For instance, as shown in Fig. 6.3-1, the modal coupling from LP_{11}^{+} mode to LP_{91}^{+} mode and to LP_{92}^{+} mode are respectively phase matched at 1.23μm and 0.64μm, while the modal coupling from LP_{11}^{-} to LP_{71}^{+} mode is phase matched at 0.94μm and to LP_{72}^{+} is phase matched at the wavelength longer than 1.75μm. However, in order to achieve effective single-mode performance, the most significant requirement is that the 1st-order HOMs, including both LP_{11}^{+} and LP_{11}^{-} modes, are supposed to be fully suppressed by coupling to relevant leaky modes at the same wavelength. In the following content, the mechanism of bending fiber induced mixture of the helical HOMs is introduced and naturally conquer the above mentioned issue.

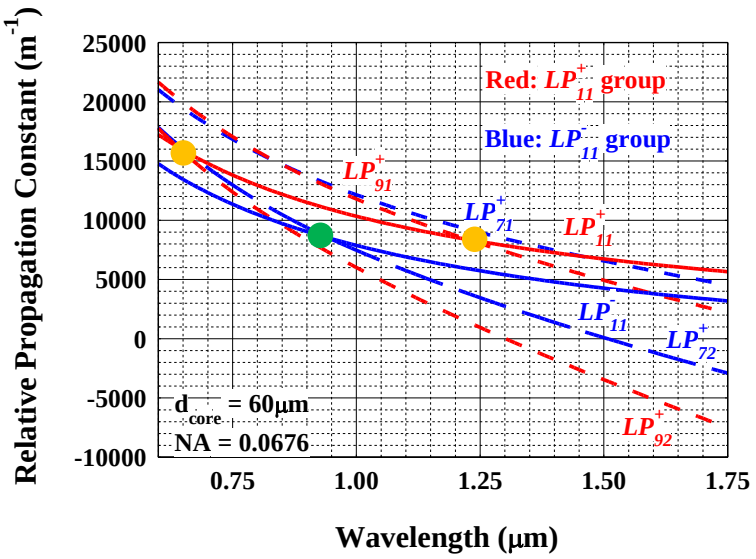

Fig. 6.3-1 The dispersion curves of $LP_{11}^{\pm}$, LP_{91}^{+}, LP_{92}^{+}, LP_{71}^{+}, and LP_{72}^{+} in a 60-μm core P-CCC fiber. These curves are seperated into two groups, LP_{11}^{+} and LP_{11}^{-}, based on the availability of phase-matching condition. The intersection of the solid curve with the dashed one in the same group, marked by orange dot for LP_{11}^{+} group and green dot for LP_{11}^{-} group, indicates the phase-matching condition is achieved.

Accompanying the modal coupling induced by polygonal symmetry, bending optical fibers, which naturally occurs when packaging, can lead to an effective attenuation on the degenerate helical mode which is not coupled to leaky modes from the loss of the other one which is coupled to, and this effective attenuation is determined by the coupling strength between these two degenerate helical modes. The critical point of this scheme is removing the degeneracy between even- and odd- linear HOMs in a bent fiber. The lifted degeneracy of linear HOMs induces the coupling between two degenerate helical modes. In the following paragraphs, this bending induced effect on linear LP_{11} mode and the inter-coupling onset between helical LP_{11} modes will be mathematically demonstrated. Even if this is only a specific case, this demonstration fully covers the principle which can also be applied to the other orders of HOMs.

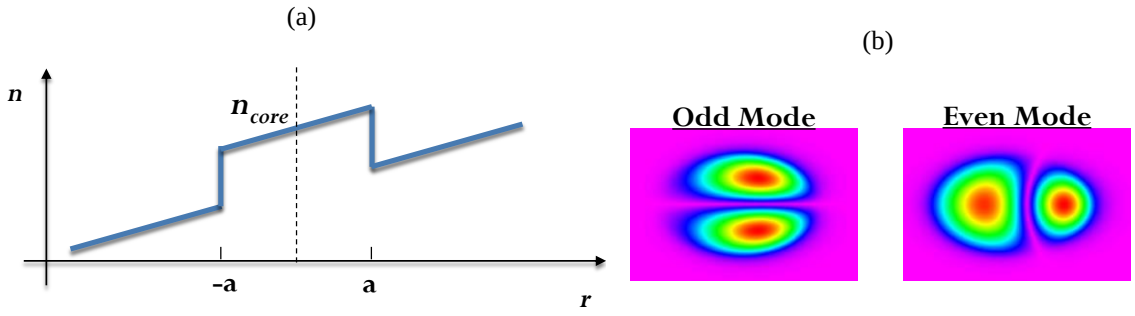

Fig. 6.3-2 (a) The transverse profile refractive of a bent step-index fiber with 2a core size (b) The distorted modal profile of odd and even LP_{11} mode due to fiber bending

When a step-index fiber is bent, the asymmetry of the refractive index profile is induced, as shown in Fig. 6.3-2 (a), and this asymmetric refractive profile leads to the distortion of the mode. For example, Fig. 6.3-2 (b) shows the modal distortion of the odd and even LP_{11} mode. Even though this bent fiber still supports even and odd LP_{11} modes, due to the asymmetric refractive index profile and distorted modal field distribution, they possess different propagation constants. As a result, the degeneracy of linear LP_{11} modes disappear. In a bent fiber, the electrical fields of these two modes can be shown as

$$\begin{aligned} E_o &\equiv a_o(z)\cdot\Gamma_o(r)\cdot\cos(\theta)\cdot e^{j\beta_o z} \equiv A_o(z)\cdot\Gamma_o(r)\cdot\cos(\theta) \\ E_e &\equiv a_e(z)\cdot\Gamma_e(r)\cdot\sin(\theta)\cdot e^{j\beta_e z} \equiv A_e(z)\cdot\Gamma_e(r)\cdot\sin(\theta) \end{aligned} \tag{6.3-1}$$

where subscripts *o* and *e* denote even and odd modes and $\beta_o \neq \beta_e$. Both these two modes are still eigen-modes in this bent fiber. In other words, if these modes are lossless, they simply have phase variation when propagating along this fiber. Thus, we can express the generalized amplitudes $A_o(z)$ and $A_e(z)$ with the matrixed form of the relevant two differential equations as

$$\frac{d}{dz}\begin{pmatrix} A_o \\ A_e \end{pmatrix} = -j\begin{pmatrix} \beta_o & 0 \\ 0 & \beta_e \end{pmatrix}\cdot\begin{pmatrix} A_o \\ A_e \end{pmatrix} \tag{6.3-2}$$

In Eq. (6.3-2), these two linear modes form a basis of the 1st-order transverse modes in this

bent fiber. The degenerate helical modes can thus be converted with these two formulas that are given by

$$\begin{aligned} A^{+} &\equiv \frac{A_o + iA_e}{\sqrt{2}} \\ A^{+} &\equiv \frac{A_o - iA_e}{\sqrt{2}} \end{aligned} \tag{6.3-3}$$

Applying Eq. (6.3-3) to Eq. (6.3-2) gives

$$\frac{d}{dz}\begin{pmatrix} A^{+} \\ A^{-} \end{pmatrix} = j\begin{pmatrix} \frac{\beta_o + \beta_e}{2} & \frac{\beta_o - \beta_e}{2} \\ \frac{\beta_o - \beta_e}{2} & \frac{\beta_o + \beta_e}{2} \end{pmatrix} \cdot \begin{pmatrix} A^{+} \\ A^{-} \end{pmatrix} \equiv j\begin{pmatrix} \overline{\beta}_c & \frac{\Delta\beta_l}{2} \\ \frac{\Delta\beta_l}{2} & \overline{\beta}_c \end{pmatrix} \cdot \begin{pmatrix} A^{+} \\ A^{-} \end{pmatrix} \tag{6.3-4}$$

where $\overline{\beta}_c$ and $\Delta\beta_l$ indicates the mean and difference of the propagation constants of the non-degenerate linear modes. Here we find $\frac{\Delta\beta_l}{2}$ serves as the coupling coefficient of these two helical modes, so we can define

$$\kappa \equiv \frac{\Delta\beta_l}{2} \tag{6.3-5}$$

Then, Eq. (6.3-4) can be further simplified by defining $A^{\pm} \equiv a^{\pm} \cdot e^{j\overline{\beta}_c z}$

$$\frac{da^{\pm}}{dz} = j\kappa \cdot a^{\mp} \cdot e^{\mp j2\Delta\beta z} \tag{6.3-6}$$

where $\Delta\beta = \frac{\overline{\beta}_c - \overline{\beta}_c}{2}$. The reason to keep $\Delta\beta$ in Eq. (6.3-6) is for applying a mathematical trick later. One thing to note is that the former $\overline{\beta}_c$ is the propagation constant of A^{+}, while the latter one is it from A^{-}.

If the power loss of A^{-} wave is considered, Eq. (6.3-6) can be modified as

$$\begin{aligned} \frac{da^{+}}{dz} &= j\kappa a^{-} e^{-j2\Delta\beta z} \\ \frac{da^{-}}{dz} &= j\kappa a^{+} e^{j2\Delta\beta z} - \frac{\alpha_{-}}{2} a^{-} \end{aligned} \tag{6.3-7}$$

In Eq. (6.3-7), one can notice the symmetry of the coupled mode equation is broken, and

this is associated to the solution of Eq. (6.3-7). Assuming the initial condition is $A^{+}(0)=A_0^{+}$ and $A^{-}(0)=0$, the solution of Eq. (6.3-6) is given by [89]

$$\begin{aligned} A^{+}(z) &= A_0^{+} e^{j\overline{\beta}z}\left[\cos\left(\sqrt{\Delta\beta^2+\kappa^2}\,z\right)+ j\frac{\Delta\beta}{\sqrt{\Delta\beta^2+\kappa^2}}\sin\left(\sqrt{\Delta\beta^2+\kappa^2}\,z\right)\right] \\ A^{-}(z) &= A_0^{+} e^{j\overline{\beta}z}\frac{j\kappa}{\sqrt{\Delta\beta^2+\kappa^2}}\cdot\sin\left(\sqrt{\Delta\beta^2+\kappa^2}\,z\right) \end{aligned} \tag{6.3-8}$$

where $\overline{\beta}=\dfrac{\overline{\beta_c}+\overline{\beta_c}}{2}$, and the former $\overline{\beta_c}$ is the propagation constant of A^{+}, while the latter one is it from A^{-}. This arrangement of parameters in Eq. (6.3-8) can help solve Eq. (6.3-7). Due to the modal loss considered for A^{-} wave, the propagation constant of A^{-} wave is modified as $\overline{\beta_c}\rightarrow\overline{\beta}_c+j\dfrac{\alpha_{-}}{2}$. Therefore, the propagation constant difference and the averaged propagation constant thus become $\Delta\beta=-j\dfrac{\alpha_{-}}{4}$ and $\overline{\beta}\rightarrow\overline{\beta}_c+j\dfrac{\alpha_{-}}{4}$ respectively. As a result, the redundancy of keeping $\Delta\beta$ in Eq. (6.3-6) and Eq. (6.3-7) is explained. Thus, the form of A^{+} can be written as

$$\begin{aligned} &A^{+}(z)= \\ &A_0^{+}e^{-j\overline{\beta}_c z}e^{-\frac{\alpha_{-}}{4}z}\left[\cos\left(\sqrt{-\frac{\alpha_{-}^2}{16}+\kappa^2}\,z\right)-j\frac{j\frac{\alpha_{-}}{4}}{\sqrt{-\frac{\alpha_{-}^2}{16}+\kappa^2}}\sin\left(\sqrt{-\frac{\alpha_{-}^2}{16}+\kappa^2}\,z\right)\right] \end{aligned} \tag{6.3-9}$$

As shown in Eq. (6.3-9), the loss of A^{-} wave is associated to it of A^{+} wave, and this is associated to the effective loss α_{+} which can be alternatively described as $\left|A^{+}(z)\right|=\left|A_0^{+}\right|\cdot e^{-\frac{\alpha_{+}}{2}z}$. Thus, taking an absolute value of Eq. (6.3-9), α_{+} can be expressed as

$$\alpha_{+}=\frac{\alpha_{-}}{2}-\mathrm{Im}\left[2\sqrt{-\frac{\alpha_{-}^2}{16}+\kappa^2}\right] \tag{6.3-10}$$

Eq. (6.3-10) can also be written as

$$\alpha_+ = \begin{cases} \dfrac{\alpha_-}{2}, \alpha_- < 4\kappa \\ 2\kappa, \alpha_- = 4\kappa \\ \dfrac{\alpha_-}{2} - 2\sqrt{\dfrac{\alpha_-^2}{16} - \kappa^2}, \alpha_- > 4\kappa \end{cases} \tag{6.3-11}$$

Eq. (6.3-11) is plotted and shown in Fig. 6.3-3.

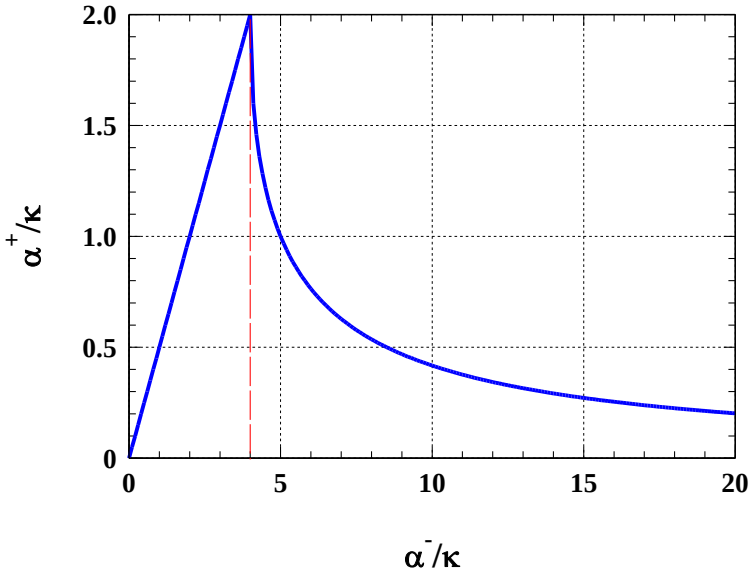

Fig. 6.3-3 Effective loss α^+ of the helical mode A^+ that is not coupled to leaky modes. This effective loss is from the loss α of the degenerate helical mode A^- that is coupled to leaky modes. The strength of α^+ is determined by the coupling strength κ between these two helical modes.

In Fig. 6.3-3, the loss of both helical modes is characterized by κ to show their dependence to the coupling strength. Since bending fibers eliminates the degeneracy of the even and odd linear LP_{11} modes, the coupling between the helical LP_{11} modes thus occurs. (This concept is analogical to the polarization coupling discussed in Subsec. 5.1.3) If one of these two helical modes is lossy (like coupling to the leaky modes or cladding modes), as shown in the above figure, the other mode is simultaneously suppressed. The

degree of this suppression is proportional to the coupling strength of these two helical modes. Therefore, we can conclude that the effective loss α^+ is determined by coupling strength κ, as shown in Eq. (6.3-11), the coupling strength κ is determined by the propagation constant difference, as shown in Eq. (6.3-5), and the propagation constant difference is determined by coiling condition. In the following paragraphs, this chain rule is applied to LP_{11} mode and numerically shown.

In order to predict the magnitude of this suppression, the lifted degeneracy of the linear LP_{11} modes for step-index fibers can be analytically calculated by the following formulas from Garth [91]

$$\delta\beta = \beta_e - \beta_o = \frac{1}{4\rho}\left(\frac{V^2}{2\Delta}\right)^{3/2} B(V)\left(\frac{\rho}{a}\right)^2$$
$$B(V) = \frac{1}{U^2}\left[\frac{1}{W^2}\frac{J_2(U)}{J_0(U)}\left(W^2 - U^2\right) - \frac{J_1^2(U)}{J_0^2(U)}\right] \tag{6.3-12}$$

with coiling diameters which are corrected by the bending induced stress [92].

$$a = \frac{a_g}{0.8} \tag{6.3-13}$$

where ρ is the effective radius of the fiber core; a is the effective radius of the coiling and it is corrected from the physical radius of coiling a_g; V is the normalized frequency of the fiber; U and W are the normalized fiber parameters which satisfy $U^2 + W^2 = V^2$. In Fig. 6.3-4, for a step-index fiber with different core sizes, Eq. (6.3-12) and Eq. (6.3-13) is applied to plot the propagation constants difference of the two nondegenerate linear LP_{11} modes versus coiling diameter.

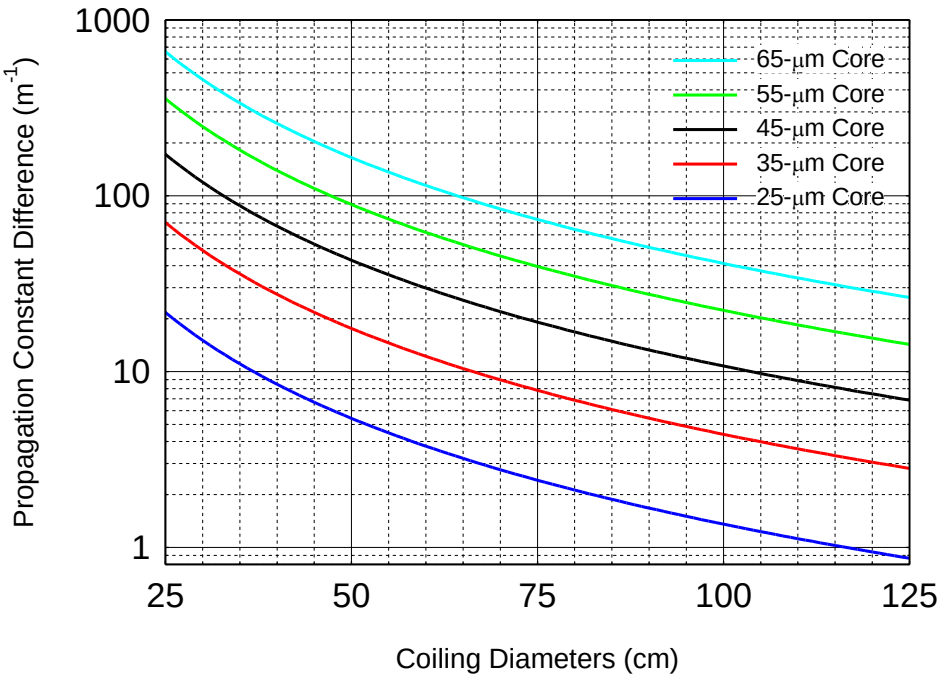

Fig. 6.3-4 The relationship between propagation constant difference between even and odd LP_{11} mode and the fiber coiling diameter at different core size (NA = 0.07).

The understanding of Eq. (6.3-5) and Eq. (6.3-11) indicates the maximum effective loss is equal to this propagation constant difference, i.e. $\alpha_+^{\max} = 2\kappa = \Delta\beta$. Thus, the maximum effective loss has the same relationship with the propagation constant difference, as shown in Fig. 6.3-5. In this figure, the core size of the fiber varies from 25 to 65-μm and the effective loss is plotted in dB scale.

Fig. 6.3-5 shows that 100-dB/m HOM suppression can be achieved when the coiling diameter of a 35-μm-core fiber is smaller than 45 cm, the coiling diameter of a 45-μm-core fiber is smaller than 70 cm, the coiling diameter of a 55-μm-core fiber is smaller than 100 cm, and the coiling diameter of a 65-μm-core fiber is smaller than 125 cm. These estimations provide a fundamental basis to further design P-CCC fibers for the purpose of mitigating TMI or SRS.

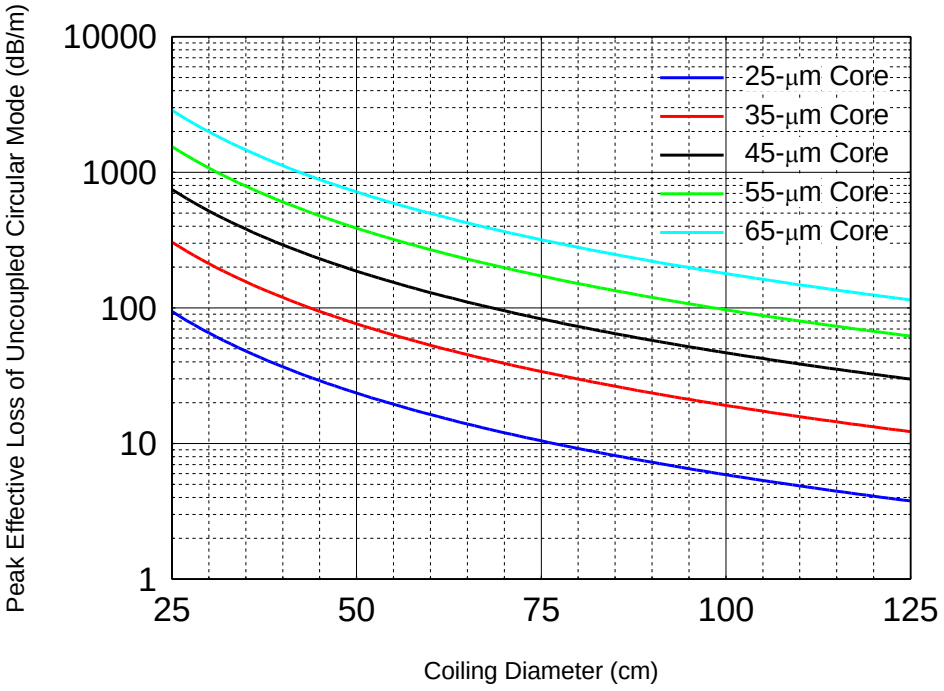

Fig. 6.3-5 The relationship between the peak effective loss of uncoupled circular mode and the fiber coiling diameter at different core sizes (NA = 0.07).

6.4 Conclusion

Compared to S-CCC fibers, an additional design flexibility exists in P-CCC fibers. This design flexibility imposed by the symmetry of the modal perturbation. When the modal number difference of two helical modes matches the perturbation symmetry, the coupling between them occurs. This indicates that the occurrence of the modal coupling in a P-CCC fiber is attributed to the non-zero overlap integral between the two helical modes over this perturbation and the achieved phase matching of these two modes along the longitudinally-twisted fiber structure.

This modal coupling through the perturbation caused by the rotational and polygonal fiber structure is mathematically proved, and the developed selection rule can be applied to the design work of E-SM CCC fibers with phase matching the coupling of the first several order HOMs to leaky modes. However, since the phase matching condition can only be satisfied with one of the two degenerate helical modes coupling to leaky modes. Therefore, bending fiber induced mixture of helical HOMs is proposed. When a fiber is bent, the degeneracy of the two linear modes at the same order vanishes, and the coupling between two helical modes at this order is thus induced because they are not eigen-mode anymore. This coupling transfers the loss from the mode which coupled to a leaky mode to the uncoupled mode thus achieving the entire suppression of the mode at the same order. The analysis shows that a bent P-CCC fiber can potentially achieve an effective loss of >100 dB/m for LP_{11} mode with the fiber being packaged with a proper coiling diameter. This level of attenuation is fairly enough to suppress transverse mode instability in high power fiber amplifiers.

Chapter VII

Summary and Future Work

7.1 Summary

In the dissertation, a knowledge base of nonlinear optical effects in large-mode area (LMA) fibers and high pulse energy fiber amplifiers is built up. The included nonlinear effects are four-wave-mixing, stimulated Raman scattering, transverse mode instability, and nonlinear polarization evolution. In order to control these effects, a novel specialty optical fiber, chirally-coupled-core (CCC) fiber, is used as the medium of carrying optical waves.

In Chapter II, a systematic process to study the use of DFWM for wavelength conversion in CCC fibers is built. The wavelength conversion via DFWM nonlinear effect in LMA fibers is analyzed with 5 aspects: 1) phase-matching condition, 2) the domination of fundamental-mode signal, 3) an efficient wavelength conversion at peak powers well below the threshold for other competing nonlinearities (stimulated Raman scattering in particular), 4) the detrimental effects associated with high loss of idler wave in fused silica at the wavelengths above ~2μm, and 5) the requirement of a high-peak-power, hundreds of picosecond pulse with pico-meter level bandwidth. Our initial exploration addressed all five issues and determined the condition under which the use of LMA CCC fibers can achieve an efficient and power scalable wavelength conversion from ~1μm (Yb-fiber operation range) down to the visible light. However, these 5 aspects are not independent,

especially in LMA CCC fibers. The phase matching condition determines the available pump, signal, and idler wavelength. The pump wavelength is associated to the acceptable pump bandwidth that is dependent on the dispersion at this wavelength. Moreover, the pump wavelength determines the Stokes wavelength which in transmission spectra of CCC fibers should be at a dip with >30 dB/m attenuation and <50 nm slope as discussed in Chapter III. At the signal wavelength, the fundamental mode attenuation is supposed to be <1dB/m in CCC fibers. The idler wavelength is directly associated to the IR molecular absorption which can dramatically vary in a small wavelength range. Thus, according to the above comments, the most critical factor of achieving an efficient wavelength conversion in CCC fibers is dispersion, which determines the phase-matched pump, signal, and idler wavelength. These three wavelengths should be able to match the design of CCC fibers.

Chapter III is an extension of Chapter II, even if the scope of it is beyond that. In this chapter, the spectral filtering properties of CCC fibers is exploited to suppress SRS. This capability of CCC fibers is demonstrated in two types of CCC fibers, one is 30-μm core and the other is 60-μm core. This also demonstrated an additional degree of design freedom, combining core-size scalability with the Stokes-wave-loss SRS suppression for high power operation.

In Chapter IV, based on the presumption that TMI is a stimulated scattering process, we rigorously model it with a fundamental theory of two-beam coupling, in which a FM and HOM couples through a thermally-induced grating imprinted by the beating between these modes. We show that previously postulated movement of this grating to phase-match the coupling between the modes naturally occurs due to a finite thermal-response time of a fiber. With considering HOM incorporated with spontaneous emission, the temporal

dynamics of TMI can be simulated and explained. From the simulation result, the noise is proved to be the triggering source of TMI, and the origin of TMI is proved the noise-induced phase lag between the radiation beating pattern of the involved modes and temperature grating. Overall, this theory is consistent with experimental observations in that it accurately predicts the onset-like threshold and temporal instabilities in the kilohertz-frequency range. Moreover, this general model can be simplified to a static model which eases the calculation of the TMI threshold. The static model is used to show that increasing higher-order mode suppression in CCC fibers increases TMI threshold power.

In Chapter V, the theory and experiment of nonlinear polarization evolution (NPE) in a 55μm core polygonal-core CCC fiber amplifier reveals that both nonlinear polarization switching and linear polarization maintaining can be achieved depending on the input signal polarization. With proper signal excitation and fiber packaging conditions linear output polarization can be maintained under a wide range of output peak powers. Moreover, in a Low-Bi CCC fiber, the presence of the circular birefringence is confirmed to complicate NPE at high peak powers, which can degrade polarization preservation at the amplifier or laser output. A more robust preservation of linear polarization output is attributed to eliminate the twisted induced circular birefringence which shifts the stabilizing eigen-mode from the linear polarization along slow axis to an elliptical polarization with smaller polarized angle.

In Chapter VI, the design principle of P-CCC fibers is mathematically investigated for an additional design flexibility and enhancing the control of nonlinearities in high power fiber amplifiers. The polygonal core can help couple the first several orders of helical HOMs to leaky modes via the rotationally symmetric perturbation. Due to the limitation on modal dispersion, only one of the two degenerate helical modes can be

coupled to leaky modes under phase-matching condition. Therefore, the unavoidable bending induced mixture of helical HOMs is exploited. A bent P-CCC fiber results in the energy interchange between the two helical modes thus introducing an effective attenuation to the degenerate helical mode which is not coupled to leaky modes. This scheme can potentially be applied to TMI or SRS suppression with providing an HOM attenuation up to the order of 100 dB/m. Overall, in this chapter, an additional design flexibility of CCC fibers in developed.

7.2 Future Work

The topic of nonlinear optical effects in high power or high energy fiber amplifiers is a tremendous field. In this dissertation, we only selected a few currently critical topics to investigate. Thus, the entire research works in this dissertation are only small part of this field, even if we have tried to cover as much as we can. For each topic in this dissertation, an extension as future works is suggested.

The wavelength conversion achieved by four wave mixing in large-core area fibers is demonstrated when pump, signal, and idler are at the same polarization and transverse modes, i.e. all three waves are LP_{01} mode and linearly polarized at a specific azimuth angle [41, 42]. This approach provides a simplest and straightforward path to efficiently generate red light. However, the achievable wavelength of the signal wave is only limited at 650μm if the pumping wavelength is in the operateable range of an ytterbium-doped fiber lasers. This constraints the applicability of visible high power fiber lasers. In order to extend the wavelength range, two advanced phase-matching method can be investigated. Firstly, a fiber with built-in birefringence provides an additional option to achieve phase–matching between different wavelengths and the two polarization modes. If birefringence is further adjustable, the achievable wavelength range can be largely extended. This scheme is based on the engineering of waveguide dispersion. Secondly, HOMs can also be exploited to achieve phase-matching and efficient wavelength conversion. Since the modal loss can be controlled by the resonance of specialty fibers, for example CCC fibers, HOMs can also be involved in a four-wave-mixing process to extend the phase-matchable wavelengths.

On the other hand, the other critical research work in this dissertation is the understanding of transverse mode instability in high power fiber amplifiers. In the last few years, even though so many researchers have contributed to understand the whole picture

of this newly found limitation on the power scalability of fiber lasers, a full explanation is still unavailable. The missed two pieces are the theoretical modeling of the build-up of TMI, and a theoretical explanation of the harmonics at TMI threshold. Even though the latter one is used to be explained as the modulation of pump or signal wave, the origin of this modulation still cannot be explained [93]. In addition, the other noise source, spontaneous thermal Rayleigh scattering, proposed by Smith [94] can be further investigated. The physics of this linearly scattering process, which is explained as the other triggering source of a TMI process, might be a key to understand the missed two pieces of TMI in high power fiber amplifiers. Other than these two parts associated to the understanding of TMI, a recently reported mitigation scheme based on the shift of the pump wavelength from 976 nm to the other wavelengths raises one more puzzling point [95]. The experimental results shows the pump wavelength is not only associated to the quantum defect but the dependency to the threshold of TMI as well as the modal oscillation frequency above threshold. These findings prove our understanding of TMI is very limited, and a further investigation is needed. Nonetheless, the focus of TMI research should be on the mitigation strategy for improving the power scalability of high average power fiber amplifiers. According to the calculation result introduced in Sec. 4.3 and 6.3, a bent P-CCC fiber is supposed a promising candidate to suppress TMI. Moreover, P-CCC fibers can also be applied to the suppression of SRS and the enhancement of DFWM. Thus, a well-designed P-CCC fiber for the purpose of controlling different types of nonlinear interactions is desired.

The third extendable topic is the nonlinear polarization evolution in high energy fiber amplifiers. The polarization evolution in a coiled high energy fiber amplifiers is not only dependent on the intensity distribution along the fiber and the coiled induced linear as well

as circular birefringence, but also on the thermal induced stress which is associated to the different thermal expansion coefficients of the doped core and un-doped cladding. Furthermore, the reason that the induced linear and circular birefringence in active CCC fiber is smaller than passive CCC fiber is still not clear. Overall, an in-depth knowledge on the mechanics of fused-silica fibers should be acquired.

This section summarizes the direction to extend the research work in this dissertation.

Bibliography

1. Wei Shi, Qiang Fang, Xiushan Zhu, R. A. Norwood, and N. Peyghambarian, “Fiber lasers and their applications”, Applied Optics Vol. 53, pp. 6554-6568 (2014)
2. Cesar Jauregui,Jens Limpert and Andreas Tünnermann, "High power fiber lasers," Nature Photonics 7, 861–867 (2013)
3. http://optics.org/news/3/10/44
4. H. M. Pask, R. J. Carman, D. C. Hanna, A. C. Tropper, C. J. Mackechnie, P. R. Barber, and J. M. Dawes. Ytterbium-doped silica fiber lasers: versatile sources for the 1-1.2 µm region. IEEE J. Sel. Top. Quantum Electron, 1(1):2–13, 1995.
5. Minelly, J. D., Taylor, E. R., Jedrzejewski, K. P., Wang, J. & Payne, D. N. Laser-diode-pumped Nd-doped fibre laser with output power>lW. Paper 246 in Proc. CLEO (1992).
6. Dominic, V. et al. 110 W fibre laser. Electron. Lett. 35, 1158–1160 (1999).
7. Jeong, Y., Sahu, J. K., Payne, D. N. & Nilsson, J. Ytterbium-doped large-core fibre laser with 1 kW of continuous-wave output power. Electron. Lett. 40, 470–472 (2004).
8. Gapontsev, V., Fomin, F. A. & Abramov, M. Diffraction limited ultra-high-power fibre lasers. Paper AWA1 in Proc. Adv. Solid-State Photon. Topical Meeting (OSA, 2010).
9. E. Snitzer, “Proposed Fiber Cavities for Optical Masers” ,J. App. Phys. Vol. 32, pp. 36-39 (1961)
10. E. Snitzer, Po, H., Hakimi, F., Tumminelli, R. & McCollum, B. C. Double clad, offset core Nd fibre laser. Paper PD5 in Proc. Opt. Fib. Sensors 2 (OSA, 1988)
11. Pierre Laperle, Claude Paré, Huimin Zheng, André Croteau, "Yb-doped LMA triple-clad fiber for power amplifiers", Proc. SPIE 6453, Fiber Lasers IV: Technology, Systems, and Applications, 645308 (2007)
12. M. H. Muendel, “Optimal inner cladding shapes for double-clad fiber lasers”, Conference of Lasers and Electro-Optics, OSA Tech. Dig. Series Vol. 9 pp. 209 (1996)
13. D. J. Digiovanni and A. J. Stentz, “Tapered fiber bundles for coupling light into and out of cladding-pumped fiber devices”, U.S. Patent 5, 864, 644 (1999)

14. Robert W. Boyd, Nonlinear Optics, Academic Press (2008)

15. Govind P. Agrawal, *Nonlinear Fiber Optics 4th ed.*, Academic Press (2007)

16. John A. Buck, *Fundamentals of Optical Fibers*, Wiley-Interscience (2004)

17. Angel Flores, Craig Robin, Ann Lanari, and Iyad Dajani, "Pseudo-random binary sequence phase modulation for narrow linewidth, kilowatt, monolithic fiber amplifiers", Optics Express Vol. 22, Issue 15, pp. 17735-17744 (2014)

18. Y. Imai and N. Shimada, "Dependence of stimulated Brillouin scattering on temperature distribution in polarization-maintaining fibers", IEEE Photon. Technol. Lett. 5, 1335 (1993)

19. Hansryd et al., "Increase of the SBS threshold in a short highly nonlinear fiber by applying a temperature distribution", J. Lightwave Technol. 19, 1691 (2001)

20. Marc D. Mermelstein, "SBS threshold measurements and acoustic beam propagation modeling in guiding and anti-guiding single mode optical fibers", Optics Express Vol. 17, pp. 16225-16237 (2009)

21. Vadim V. Lozovoy, Igor Pastirk, and Marcos Dantus, "Multiphoton intrapulse interference. IV. Ultrashort laser pulse spectral phase characterization and compensation", Optics Letters Vol. 29, pp. 775-777 (2004)

22. Schimpf, D. N. et al., "Circular versus linear polarization in laser-amplifiers with Kerr-nonlinearity", Opt. Express 17, 18774–18781 (2009).

23. Fibich, G. & Gaeta, A. L., "Critical power for self-focusing in bulk media and in hollow waveguides", Opt. Lett. Vol. 25, pp. 335–337 (2000).

24. Eidam, T., Wirth, C., Jauregui, C., Stutzki, F., Jansen, F., Otto, H.-J., Schmidt, O., Schreiber, T., Limpert, J., and Tünnermann, A., "Experimental observations of the threshold-like onset of mode instabilities in high power fiber amplifiers," Opt. Express 19(14), 13218 (2011)

25. Otto, H.-J., Stutzki, F., Jansen, F., Eidam, T., Jauregui, C., Limpert, J., and Tünnermann, A., "Temporal dynamics of mode instabilities in high-power fiber lasers and amplifiers," Opt. Express 20, 15710–15722 (2012)

26. Nicoletta Haarlammert, Oliver de Vries, Andreas Liem, Andrea Kliner, Thomas Peschel, Thomas Schreiber, Ramona Eberhardt, and Andreas Tünnermann, "Build up and decay of mode instability in a high power fiber amplifier", Opt. Express Vol. 20, pp. 13274-13283 (2012)

27. Cesar Jauregui, Tino Eidam, Hans-Jürgen Otto, Fabian Stutzki, Florian Jansen, Jens Limpert, and Andreas Tünnermann, "Physical origin of mode instabilities in high-power fiber laser systems", Opt. Express, Vol. 20, pp.12912-12925 (2012)

28. Shadi Naderi, Iyad Dajani, Timothy Madden, and Craig Robin "Investigations of modal

instabilities in fiber amplifiers through detailed numerical simulations“, Opt. Express, 21, 16111-1612

29. Ward, B., Robin, C., and Dajani, I., “Origin of thermal modal instabilities in large mode area fiber amplifiers,” Opt. Express 20(10), 11407–11422 (2012)

30. Hans-Jürgen Otto, Cesar Jauregui, Fabian Stutzki, Florian Jansen, Jens Limpert, and Andreas Tünnermann, "Controlling mode instabilities by dynamic mode excitation with an acousto-optic deflector", Opt. Express Vol. 21, pp.17285-17298 (2013)

31. Laurila, M. et al. “Distributed mode filtering rod fibre amplifier delivering 292W with improved mode stability”, Opt. Express, Vol. 20, pp. 5742–5753 (2012).

32. Craig Robin, Iyad Dajani, and Benjamin Pulford, "Modal instability-suppressing, single-frequency photonic crystal fiber amplifier with 811 W output power", Opt. Letters Vol. 39, pp.666-669 (2014)

33. M. E. Fermann, “Single-mode excitation of multimode fibers with ultrashort pulses,” Opt. Lett. 23(1), 52–54 (1998).

34. J. P. Koplow, D. A. V. Kliner, and L. Goldberg, “Single-mode operation of a coiled multimode fiber amplifier,” Opt. Lett. 25(7), 442–444 (2000).

35. T. A. Birks, J. C. Knight, and P. St.J. Russell, "Endlessly single-mode photonic crystal fiber", Optics Letters Vol. 22, pp. 961-963 (1997)

36. F. Stutzki, F. Jansen, T. Eidam, A. Steinmetz, C. Jauregui, J. Limpert, and A. Tünnermann, “High average power large-pitch fiber amplifier with robust single-mode operation,” Opt. Lett. 36(5), 689–691 (2011).

37. Eidam, T. et al. Fibre chirped-pulse amplification system emitting 3.8 GW peak power. Opt. Express 19, 255–260 (2011)

38. X. Ma, C.-H. Liu, G. Chang, and A. Galvanauskas, “Angular-momentum coupled optical waves in chirally-coupled-core fibers,” Opt. Express 19(27), 26515–26528 (2011).

39. Xiuquan Ma, Cheng Zhu, I-Ning Hu, Alex Kaplan, and Almantas Galvanauskas, "Single-mode chirally-coupled-core fibers with larger than 50μm diameter cores", Opt. Express 22, 9206-9219 (2014).

40. Cheng Zhu, "High Power Chirally-Couple-Core (CCC) Fiber Lasers for Coherent Combining Systems", Doctoral Thesis at the University of Michigan, 2014.

41. D. Nodop,* C. Jauregui, D. Schimpf, J. Limpert, and A. Tünnermann, “Efficient high-power generation of visible and mid-infrared light by degenerate four-wave-mixing in a large-mode-area photonic-crystal fiber”, Opt. Lett. 34, 3499 (2009).

42. Cesar Jauregui, Alexander Steinmetz, Jens Limpert, and Andreas Tünnermann, "High-power efficient generation of visible and mid-infrared radiation exploiting four-wave-mixing in optical fibers", Opt. Express 20, 24957 (2012).

43. Yijiang Chen, "Combined processes of stimulated Raman scattering and four-wave mixing in optical fibers", J. Opt. Soc. Am. B, Vol. 7, pp. 43-52 (1990)

44 A. De Rossi, V. Berger, M. Calligaro, G. Leo, V. Ortiz, and X. Marcadet, "Parametric fluorescence in oxidized aluminum gallium arsenide waveguides", Applied Physics Letters, Vol 79, pp. 3758-3760 (2001).

45 R. G. Smith, "Optical power handling capacity of low loss optical fibers as determined by stimulated Raman and brillouin scattering," Appl. Opt. 11(11), 2489–2494 (1972).

46. Rei Kitamura, Laurent Pilon, and Miroslaw Jonasz, "Optical constants of silica glass from extreme ultraviolet to far infrared at near room temperature", Applied Optics, Vol . 46, pp. 8118-8133 (2007)

47. Dennis D. Lowenthal, "CW Periodically Poled $LiNbO_3$ Optical Parametric Oscillator Model with Strong Idler Absorption", IEEE Jourrnal oF Quantum Electronics, Vol. 34, pp. 1356-1366

48. Andrew Weine, Ultrafast Optics, John Wiley & Sons (2011)

49. E. M. Dianov, A. V. Shubin, M. A. Melkumov, O. I. Medvedkov, and I. A. Bufetov, "High-power cw bismuth-fiber lasers", J. Opt. Soc. Am. B 24, 1749-1755 (2007).

50. Jens Limpert, Fabian Stutzki, Florian Jansen, Hans-Jürgen Otto, Tino Eidam, Cesar Jauregui and Andreas Tünnermann, "Yb-doped large-pitch fibres: effective single-mode operation based on higher-order mode delocalization", Light: Science & Applications (2012) **1**, e8

51. Moritz M. Vogel, Marwan Abdou-Ahmed, Andreas Voss, and Thomas Graf, "Very-

large-mode-area, single-mode multicore fiber", Optics Letters, Vol. 34, Issue 18, pp. 2876-2878 (2009)

52. T. A. Birks, J. C. Knight, and P. St. J. Russell, "Endlessly single-mode photonic crystal fiber", Optics Letters, Vol. 22, Issue 13, pp. 961-963 (1997)

53. E.A. Kuzin, G. Beltran-Perez, M.A. Basurto-Pensado, R. Rojas-Laguna, J.A. Andrade-Lucio, M. Torres-Cisneros, E. Alvarado-Mendez, "Stimulated Raman scattering in a fiber with bending loss", Optics Communications, Vol. 169, pp. 87–91 (1999)

54. L. A. Zenteno, J. Wang , D. T. Walton , B. A. Ruffin, M.J. Li, S. Gray, A. Crowley and X. Chen, "Suppression of Raman gain in single-transverse-mode dual-hole-assisted fiber", Opt. Express 13, 8921-8926 (2005).

55. J. Kim, P. Dupriez, C. Codemard, J. Nilsson, and J. K. Sahu, "Suppression of stimulated Raman scattering in a high power Yb-doped fiber amplifier using a W-type core with fundamental mode cut-off", Opt. Express 14, 5103-5113 (2006).

56. J. M. Fini, R. T. Bise, M. Yan, A. D. Yablon, and P. Wisk, "Distributed fiber filter based

on index-matched coupling between core and cladding", Opt. Express 13, 10022-10033 (2005).

57. J. M. Fini, M. D. Mermelstein, M. F. Yan, R. T. Bise, A. D. Yablon, P. W. Wisk, and M. J. Andrejco, "Distributed suppression of stimulated Raman scattering in an Yb-doped filter-fiber amplifier", Opt. Lett. 31, 2550-2552 (2006).

58. F. Benabid, G. Bouwmans, J. C. Knight, and P. St. J. Russell, "Ultrahigh Efficiency Laser Wavelength Conversion in a Gas-Filled Hollow Core Photonic Crystal Fiber by Pure Stimulated Rotational Raman Scattering in Molecular Hydrogen", Phys. Rev. Lett. 93, 123903 (2004).

59. T. Taru, J. Hou, and J. C. Knight, "Raman gain suppression in all-solid photonic bandgap fiber", in European Conference and Exhibition on Optical Communication 2007, Berlin (Sep. 2007), paper 7.1.1.

60. S. Blin, L. Provino, N. Traynor, A. Mugnier, D. Pureur, and T. Chartier, "Design of all-solid photonic-bandgap fibers for Raman-free propagation", in CLEO/Europe and EQEC 2009 Conference Digest, (Optical Society of America, 2009), paper CJ1_5.

61. Akira Shirakawa, Yuta Suzuki, Suguru Arisa, Mingchen Chen, C. B. Olausson, Jens K. Lyngsø, and Jes Broeng, " High-peak Power Pulse Amplification by SRS-suppressed Photonic Bandgap Fiber", in Lasers and Electro-Optics Pacific Rim (CLEO-PR) 2013 Conference, Kyoto (Jun.-Jul 2013), paper TuA2-1.

62. Xiuquan Ma, I-Ning Hu, and Almantas Galvanauskas, "Propagation-length independent SRS threshold in chirally-coupled-core fibers",Opt. Express 19, 22575-22581 (2011).

63. Chisato Fukai, Kazuhide Nakajima, Jian Zhou, Katsusuke Tajima, Kenji Kurokawa, and Izumi Sankawa, "Effective Raman gain characteristics in germanium- and fluorine-doped optical fibers", Opt. Lett. 29, 545-547 (2004).

64 . Ferdinand A. Oguama, Hernando Garcia, Anthony M. Johnson, "Simultaneous measurement of the Raman gain coefficient and the nonlinear refractive index of optical fibers: theory and experiment", J. Opt. Soc. Am. B 22, 426-436 (2005).

65. Stutzki, F., Otto, H.-J., Jansen, F., Gaida, C., Jauregui, C., Limpert, J., and Tünnermann, A., "High-speed modal decomposition of mode instabilities in high-power fiber lasers," Opt. Lett. 36(23), 4572-4574 (2011)

66. Smith, A. and Smith, J., "Mode instability in high power fiber amplifiers," Opt. Express 19, 10180–10192 (2011)

67. I-Ning Hu, Cheng Zhu, Chao Zhang, Alexander Thomas, and Almantas Galvanauskas, " Analytical Time-Dependent Theory of Thermally-Induced Modal Instabilities in High

Power Fiber Amplifiers," in Proc. SPIE, 2013, vol. 8605, Fiber Lasers X: Technology, Systems, and Applications, pp.860109-1–860109-9.

68. Hansen, K.-R., Alkeskjold, T.-T., Broeng, J., and Lægsgaard, J., “Thermally induced mode coupling in rare-earth doped fiber amplifiers,” Opt. Letters 37, 2382–2384 (2012).

69. Liang Dong, “Stimulated thermal Rayleigh scattering in optical fibers”, Opt. Express 21, 2642-2656 (2013).

70. Cesar Jauregui, Tino Eidam, Jens Limpert, and Andreas Tünnermann, "Impact of modal interference on the beam quality of high-power fiber amplifiers", Opt. Express, Vol. 19, pp.3258-3271 (2011)

71. Boyd, W.-R., [Nonlinear Optics, 3rd Edition], Academic Press, Burlington, 369-374 (2008).

72. Kristian Rymann Hansen, Thomas Tanggaard Alkeskjold, Jes Broeng, and Jesper Lægsgaard, "Theoretical analysis of mode instability in high-power fiber amplifiers", Opt. Express, Vol. 21, pp. 1944-1971 (2013)

73. Cesar Jauregui, Hans-Jürgen Otto, Fabian Stutzki, Florian Jansen, Jens Limpert,and Andreas Tünnermann,"Passive mitigation strategies for mode instabilities in high-power fiber laser systems", Opt. Express Vol. 21, pp.19375-19386 (2013)

74. Hans-Jürgen Otto, Arno Klenke, Cesar Jauregui, Fabian Stutzki, Jens Limpert, and Andreas Tünnermann, "Scaling the mode instability threshold with multicore fibers", Opt. Letters Vol. 39, pp.2680-2683 (2014)

75. Xue Liu, Joseph W. Haus, S.M. Shahriar, "Modulation instability for a relaxational Kerr medium", Opt. Communications, Vol. 281, pp.2907-2912 (2008)

76. Y. Silberberg and I. Bar Joseph, "Instabilities, Self-Oscillation, and Chaos in a Simple Nonlinear Optical Interaction", Physical Review Letters, Vol. 48, pp. 1541-1543 (1982).

77. Yaron Silberberg and Israel Bar-Joseph, "Optical instabilities in a nonlinear Kerr medium", J. Opt. Soc. Am. B, Vol. 1, pp. 662-670 (1984).

78. Amos A. Hardy, "Amplified Spontaneous Emission and Rayleigh Backscattering in Strongly Pumped Fiber Amplifiers", J. Lightwave Technology, Vol. 16, pp. 1865-1873 (1998)

79. Uri M. Ascher, Chen Greif, *A First Course on Numerical Methods*, SIAM, 2011

80. Michelle L. Stock, Chi-Hung Liu, Andrey Kuznetsov, Gaston Tudury, Almantas Galvanauskas and Tom Sosnowski, "Polarized, 100 kW peak power, high brightness nanosecond lasers based on 3C optical fiber," in Proc. SPIE, 2011, vol. 8605, Fiber Lasers X: Technology, Systems, and Applications, pp. 79140U-1–79140U-9.

81. Kazuyoku Tei, Tsutomu Sakurai, Jun Enokidani, and Shin Sumida, "Monolithic Polarization-maintaining Amplifier Based on Chirally Coupled Core Fibers", Advanced Solid State Lasers, Shanghai China, November 16-21, 2014

82. Timothy S. McComb, Geoff Fanning, David Logan, Roger Farrow, Tyson L. Lowder, Joona J. Koponen, "Nonlinear Effects in High Peak Power 3C Fiber Amplifiers", Specialty Optical Fibers, Barcelona Spain, July 27-31, 2014.

83. R. Ulrich, S. C. Rashleigh and W. Eickhoff , "Bending-induced birefringence in single mode fiber", Opt. Lett., Vol. 5, pp.273-275 (1980)

84. R. Ulrich and A. Simon, "Polarization optics of twisted single mode fibers", Appl. Opt., Vol. 18, pp.2241-2251 (1979)

85. Sandra F. Feldman, Doreen A. Weinberger, and Herbert G. Winful, "Polarization instability in a twisted birefringent optical fiber", J. OSA B, Vol. 10, pp. 1191-1201 (1993)

86. Edward Collett, *Field Guide to Polarization* (SPIE Press, 2005)

87. F. Matera and S. Wabnitz, "Nonlinear polarization evolution and instability in a twisted birefringent fiber", Optics Letters, Vol. 11, pp.467-469 (1986)

88. http://en.wikipedia.org/wiki/Quartic_function, Quartic Function, Wikipedia

89. Xiuquan Ma, "Understanding and controlling angular momentum coupled optical waves in chirally-coupled-core (CCC) fibers," Doctoral Dissertation, University of Michigan at Ann Arbor.

90. A.W. Snyder, J. Love, *Optical Waveguide Theory*, Springer Science & Business Media (1983)

91. S. J. Garth, "Modes on a bent optical waveguide", IEEE Proceedings, Vol. 134, Pt. J, No. 4 (1987)

92. Kazuo Nagano, Shojiro Kawakami, and Shigeo Nishida, "Change of the refractive index in an optical fiber due to external forces", Applied Optics, Vol. 17, No.13 (1978)

93. Arlee V. Smith and Jesse J. Smith," Modeled fiber amplifier performance near the mode instability threshold", arXiv:1301.4278v1 [physics.optics] (2013)

94. Arlee V. Smith and Jesse J. Smith, "Spontaneous Rayleigh Seed for Stimulated Rayleigh Scattering in High Power Fiber Amplifiers", IEEE Photonics Journal, Vol. 5, pp. 7100807 (2013)

95 Rumao Tao, Pengfei Ma, Xiaolin Wang, Pu Zhou and Zejin Liu, "Mitigating of modal instabilities in linearly-polarized fiber amplifiers by shifting pump wavelength", Journal of Optics, Vol. 17, pp. 045504 (2015)